Forming Wide-Orbit Planets via Pebble Accretion

Nerea Gurrutxaga

Division of Astrophysics
Department of Physics
Lund University

2023-EXA212

Degree project of 60 higher education credits (for a degree of Master)

Supervisor: Anders Johansen &
Michiel Lambrechts

Division of Astrophysics
Department of Physics
Box 43
SE-221 00 Lund
Sweden

Popular Summary

Planets form alongside stars within protoplanetary disks composed of gas and solids. This material rotates around the central star and can convert into planets. The tiniest solid particles, called dust, can grow up to form rocky/icy planets or the core of giant planets. In the latter case, once the core forms, it attracts gas and becomes a gas giant.

The initial dust grows into pebbles, which are mm-cm size solid particles. The gas rotates slower than solids, but dust easily couples to the slower rotation. However, when dust grows up to the size of pebbles, the friction exerted by the gas decelerates them. Consequently, pebbles might fall towards the star. In this project, we studied how a Moon-size body, called the embryo, can attract these drifting pebbles. When the embryo effectively attracts pebbles, it can grow to over ten times the size of Earth, which is similar to the typical size of the core of gas giants like Jupiter and Saturn. We refer to this process as pebble accretion.

While the embryo grows via pebble accretion, it also gets closer to the star because of its gravitational interaction with the gas. Therefore, it is challenging to keep planets in the outer regions. Our understanding of the mechanism responsible for the observed wide-orbit exoplanets remains elusive. In addition, from observations of protoplanetary disks, we know that some disks have substructures, such as gaps in the outer regions, which might be formed by massive and distant planets. Moreover, some of these planets would have to form very quickly since the gaps are also observed within young disks. Our main goal has been to figure out if it is possible to form planets with these characteristics via pebble accretion.

The key finding of our work is that pebble accretion could explain the fast formation of cores in the outer regions under certain conditions. We need the embryos to form early in the outermost regions and the gas to decelerate pebbles efficiently. When the pebble mass reservoir is large, the distance away from the star at which cores can form increases. We also found that if the turbulent motions of the gas are weak, it is easier to form cores in the outer regions. The core can form far away from the star at the early stages, and therefore, it can still attract gas and become a gas giant. However, as there might be still plenty of gas remaining, the large amount of gas decelerates the core, and thus, it migrates inwards for a long distance. Drawing an analogy with the Solar System, the cores could form beyond Neptune's orbit but eventually evolve into gas giants orbiting between Jupiter and Saturn.

Abstract

The possibility that detected substructures in protoplanetary disks, such as gaps, rings and cavities, are created by distant protoplanets has prompted an inquiry into the mechanism responsible for their formation. These wide-orbit young bodies are likely to form relatively rapidly in the outer regions of circumstellar disks. Pebble accretion is considered a promising candidate to explain their formation, as distant reservoirs of pebbles (mm-cm sized particles) have been confirmed, and the mechanism can enhance the growth rate of forming planets. However, the inwards migration of planets and the slower growth in the outer regions still challenge wide-orbit planet formation via pebble accretion. Therefore, the disk must harbour the appropriate characteristics for the fast growth of the body.

With the aim of constraining such features, we utilised existing models, which describe the growth and migration of distant protoplanets until the dispersal of the disk. We also presented a novel analytical model to explain the depletion of pebbles over the evolving disk. This model facilitates the simulation of more realistic formation scenarios when pebbles drift fast across the disk generating a strong but short-lasting pebble flux.

We found that a Moon-sized protoplanetary embryo formed at very early stages and located beyond 50 AU can grow up to become the core of a gas giant (and therefore open a gap) at $20 - 50$ AU within less than 1 Myr. The outermost cores form when there is a strong but short-lasting pebble flux with a Stokes number of $\mathrm{St} \gtrsim 0.03$. A metallicity of $Z_0 \sim 0.01 - 0.02$ and low turbulence of $\alpha_\mathrm{t} \lesssim 10^{-4}$ also enhances the formation of distant cores. As these cores form very early, they undergo a fast inwards migration while they accrete gas, and by the end of the disk lifetime (~ 3 Myr), they become giant planets orbiting at < 10 AU. In view of these results, we proposed a new mechanism for forming wide-orbit gas giants, and we showed that it might be possible to form gas giants at $10 - 50$ AU at the end of the disk lifetime. According to our model, these planets are rare, in agreement with the low occurrence of gas giants in the outer regions from direct imaging surveys.

Overall, protoplanets migrate several AU before they become gas giants. That suggests that giant planets in our Solar System, such as Jupiter, might have started forming from protoplanetary embryos at distant locations. If the giant planets accrete most of their solid material in the outermost regions, this can have a significant impact on their ultimate composition.

Acknowledgements

I would like to express my sincere gratitude to my advisors, Anders and Michiel, for their support and guidance throughout my thesis. I am especially grateful to Anders for his constructive feedback and engaging discussions, which have contributed significantly to my academic growth.

I also want to extend my appreciation to all the researchers I had the pleasure of working with during my master's program. Collaborating with other master's and PhD students has made my experience at Lund University all the more fulfilling. I am deeply thankful to Florent, Alvaro, and Bibi for their dedication to maximising our collective academic experience, and to my examiners, Jens and Alex, for their constructive feedback.

Furthermore, I am grateful to my parents and grandmother for their invaluable support throughout my studies. I would also like to thank my friend Alessandro who consistently offered a helping hand whenever I needed it. Lastly, I wish to express my gratitude to Pablo for encouraging and inspiring me every day during this thesis.

Contents

Chapter 1

Introduction

The formation of wide-orbit planets has become of special interest with recent detections from Atacama Large Millimeter/submillimeter Array (ALMA). ALMA has detected plenty of protoplanetary disks that show substructures such as gaps, rings, spirals and cavities (see review by Bae et al., 2022). Although the origin of all the substructures is still unknown, it is possible that protoplanets[1] could have created them. These proposed protoplanets need to be massive bodies ($\gtrsim 10\,M_\oplus$) so that they can perturb the gas within the disk and orbit at large distances ($> 10\,AU$) to match with the location of observed substructures (see fig. 1.1). Furthermore, observations reveal that some disks younger than 1 Myr contain gaps (e.g. Sheehan & Eisner, 2018). If these gaps were formed by protoplanets, the protoplanets must have formed at early stages.

There is already evidence supporting the idea that substructures might form due to the presence of a protoplanet. The first observations are related to a cavity created by PDS 70b and c, which are bodies orbiting at $\sim 22\,AU$ and $\sim 35\,AU$, respectively, within a disk with an age of approximately 5 Myr (Keppler et al., 2018; Haffert et al., 2019). Another more recent evidence is the spirals excited by the planet AB Aur b at $\sim 90\,AU$ (Currie et al., 2022). The detection of these protoplanets does not imply that all detected substructures must form due to the presence of a planet. However, it is necessary to study how common this mechanism is and whether it can explain the origin of the substructures for which no direct evidence of protoplanets has been found. To date, the formation mechanism of early-formed, distant and massive planets is still an open question.

To study the formation of planets massive enough create substructures, we will focus on the formation of giant planets. Given that these planets contain a large percentage of gas, their formation must occur before the gas within the circumstellar disk dissipates, typically within a few million years (Hartmann et al., 1998; Soderblom et al., 2014). Two distinct mechanisms have prevailed to explain their formation; the core accretion scenario (Safronov, 1972; Pollack et al., 1996) and the Gravitational Instability (GI) mechanism (Boss, 1997). The core accretion model proposes that a massive core forms first, followed by the accretion of a gaseous envelope. A crucial aspect of this model is that the core must reach sufficient mass to accrete gas before the disk dispersal. The GI scenario can occur when the disk is

[1] Protoplanets are planets still in the ongoing formation process.

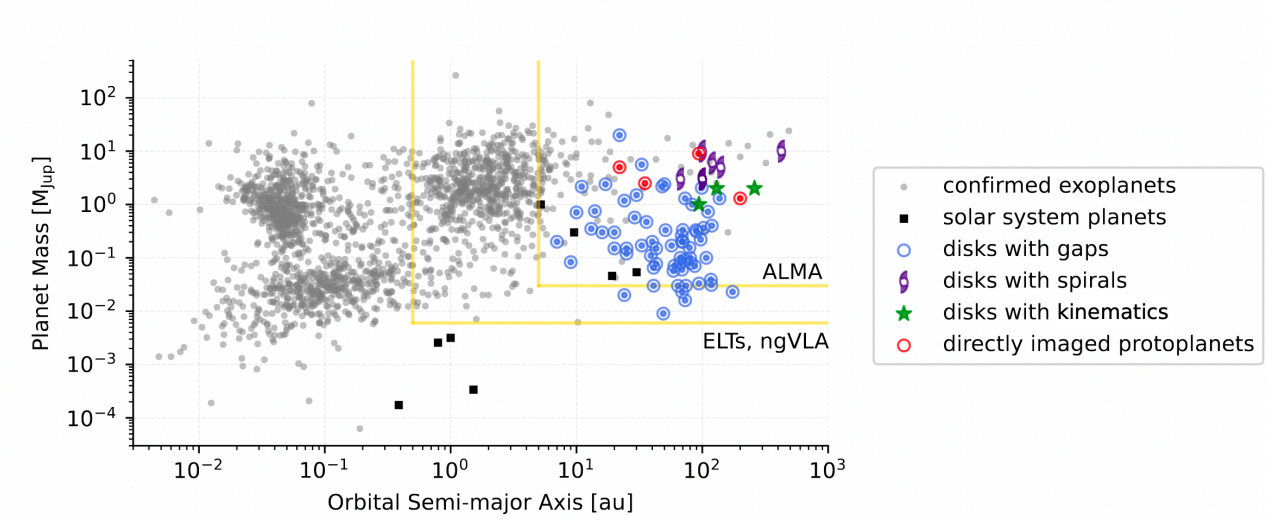

Figure 1.1: Distribution of confirmed exoplanets (grey dots), planets within the Solar System (black squares), proposed protoplanets to reproduce the observed disk substructures (blue ⊙ for gaps, purple spiral symbols for spirals, and green stars for kinematic planetary signatures) and directly imaged protoplanets (PDS 70b and c, AB Aur b and AS 209b) with red ⊙ symbols. The figure does not include the uncertainties in the estimated mass of the protoplanet, which can typically range from a factor of a few to ten. These uncertainties are mainly due to poorly constrained properties of the disk, such as its viscosity. The yellow lines indicate areas where current and future observing facilities such as ALMA, the next generation Very Large Array (ngVLA) and the Extremely Large Telescope (ELT) are predicted to discover protoplanets directly or through the disk substructures that they generate. Figure from Bae et al. (2022).

sufficiently massive so that the disk's self-gravity can trigger a collapse and result in the formation of a planet. In this work, we will focus on the possibility of planet formation based on the core accretion model.

According to classical theory, the core of the protoplanet grows by accreting planetesimals from its vicinity (Wetherill & Stewart, 1989). Nevertheless, the formation of gas giants in the outer regions via planetesimal-driven scenarios is hindered by long core formation times (e.g. Ida & Lin, 2004; Bitsch et al., 2015b; Johansen & Bitsch, 2019). By the time the core has formed, the gas has already dispersed, preventing the core from becoming a gas giant. Given the limitations of planetesimal accretion, a new paradigm called pebble accretion was prompted in the last decade (see review by Johansen & Lambrechts, 2017). The mechanism was first discovered by Ormel & Klahr (2010) and later studied more in detail by Lambrechts & Johansen (2012). The authors found that if there are enough pebbles (∼mm/cm size particles) in the disk, pebble accretion is more efficient than planetesimal accretion. That occurs because a flux of pebbles flows from the outside towards the centre of the disk, and the drag force exerted by the gas slows down pebbles passing the protoplanet but not the planetesimals themselves. Therefore, pebble accretion increases the growth rates of forming planets.

Although pebble accretion is a prospective mechanism for rapid core formation, the formation of wide-orbit planets still faces some challenges. One of the main issues is that the protoplanet interacts gravitationally with the gas disk, causing an inwards migration towards the central star (Tanaka et al., 2002). That migration can be rapid enough to prevent the formation and survival of gas giants (Coleman & Nelson, 2014). Moreover, the outcome of planet formation strongly depends on the turbulence of the disk and on the mass of the pebble reservoir (Ormel, 2017). It is, therefore, necessary to identify the characteristics that can lead to the formation of distant planets.

Recent studies of wide-orbit planet formation embraced the idea of pressure bumps or rings that prevent the planet from migrating too fast inwards and to have enough solid build-up for growth (e.g. Morbidelli, 2020; Chambers, 2021; Jiang & Ormel, 2023). However, as discussed above, the substructures within the disk might be caused by other planets. We will therefore focus on the formation of the earliest planets and consider disks with monotonic pressure profiles, i.e. without pressure bumps and substructures. We will analyse the evolution of individual [2] embryos initially located in the outer regions with initial masses close to $M_0 \sim 0.01\,\mathrm{M}_\oplus$. We will see later that the core of a gas giant is already massive enough to open a gap within the disk. Therefore, we will not concentrate only on the final location of the giant planets but also on where their cores form. Since gaps are the most common substructures (Bae et al., 2022), we will focus on their link with planet formation.

This work is structured as follows. In section 2, we explain the physical concepts underlying the work. In section 3, we explain the existing models we employed for describing growth and migration of distant protoplanets. We also present a novel analytical model to explain the depletion of pebbles. In section 4, we present and discuss the results of our work, and in section 5, we explain the main limitations and future prospects.

[2] We assume that a protoplanet does not interact with any other protoplanet within the disk.

Chapter 2

Background

In this chapter we introduce the main physical aspects of the planet-forming process. It is known that the birthplace of planets, the disk, evolves (Hartmann et al., 1998), and that the structure of the disk plays a fundamental role in planet formation (Bitsch et al., 2015a; Ida et al., 2016). Hence, we begin by explaining the most important aspects of the disk structure and evolution. Next, we focus on the dynamics and growth of the solid particles, which establish the basics of pebble accretion. To finish, we explain the growth and migration mechanisms of planets.

2.1 Gas disk structure and evolution

Protoplanetary disks surround the nascent stars. Approximately 99% of the matter in a disk is gas (mainly H and He), and the rest is solid, initially μm-sized dust (Armitage, 2010). The dynamics of the gas and solids are different, and therefore, the distribution of the gas and that of the solid differ during evolution. We will focus on the gas disk for now.

Figure 2.1a illustrates a disk spanning over 100 AU, although some disks can be more compact with sizes as small as 30 AU (Drążkowska et al., 2022). Furthermore, a gas disk tends to increase in size as it evolves. Apart from the radial extension, it has a vertical structure that is assumed to be in isothermal hydrostatic equilibrium and geometrically thin (Armitage, 2010). If the self-gravity of the disk can be neglected, the disk is nearly Keplerian i.e. its orbital velocity is approximately

$$v_{\mathrm{K}} = r\,\Omega_{\mathrm{K}} = \sqrt{\frac{GM_*}{r}}, \tag{2.1}$$

where r is the radial distance from the parent star, Ω_{K} the keplerian frequency and M_* the mass of the central star. The disk structure varies with the radial distance from the central star and age of the disk, and it is commonly described by the gas surface density Σ_{g}, the temperature T or the related magnitude the gas sound speed $T \propto c_{\mathrm{s}}^2$, and the scale height

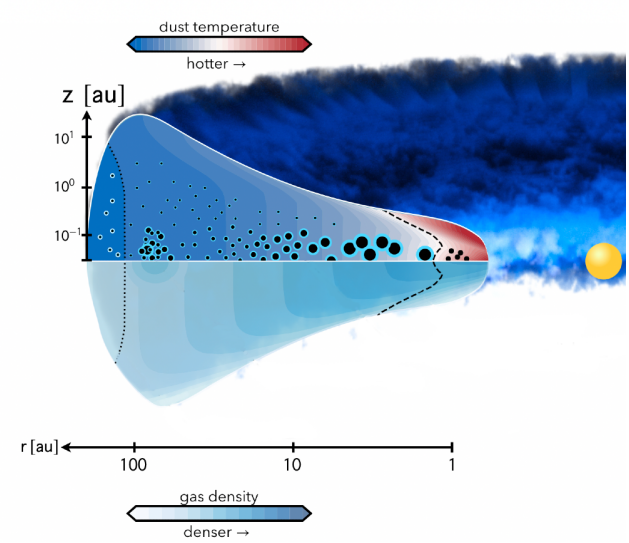

(a) Structure of the gas disk. The temperature and density decrease with increasing distance from the star. Black dots correspond to solid particles with different sizes. Figure adapted from Miotello et al. (2022).

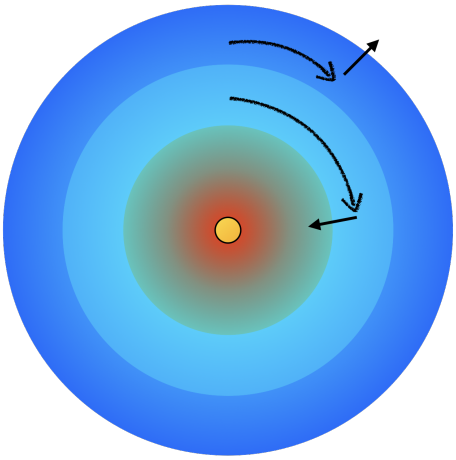

(b) At Keplerian velocities, the orbital velocity of the inner regions of a disk is greater than that of the outer regions. The viscosity between adjacent layers makes the inner regions move inward while the outer regions move outward.

Figure 2.1: Schematic view of the disk structure and evolution.

H. The scale height is defined as[1],

$$H(r) = \frac{c_\mathrm{s}(r)}{\Omega(r)}. \tag{2.2}$$

The density and temperature of the disk decrease with radial distance (see fig. 2.1a). Consequently, the pressure also decreases with distance. The pressure gradient exerts an outwards force on the gas, and therefore, the gas rotates at sub-Keplerian speed ($v_\theta \approx 0.995 v_\mathrm{K}$, Armitage, 2010). This pressure gradient force does not affect solids, which is why the dynamics of the gas and solids differ significantly.

The disk evolves with a typical disk lifetime of $t_\mathrm{f} \sim 3\,\mathrm{Myr}$ (Haisch et al., 2001; Williams & Cieza, 2011). To explain why the disk evolves, the radial dependence of the orbital velocity of the gas can be approximated as the Keplerian one, i.e. $v_\phi \sim v_\mathrm{K} \propto r^{-1/2}$ (see eq. 2.1). From that relation, we can deduce that the inner regions orbit faster than the outer ones. The viscosity between adjacent layers rotating at different velocities makes the inner regions move inward while the outer regions move outward (see fig. 2.1b). Observations of the rate at which gas accretes onto the star[2] (e.g. Manara et al., 2012) suggest that the gas is transported at a faster rate than what would be anticipated by molecular viscosity alone. The origin of the anomalously high viscosity is not well understood yet (Hartmann

[1] As the gas is assumed to be vertically isothermal and in hydrostatic equilibrium, the volume density $\rho(z) = \rho_0 e^{-z^2/2/(c_\mathrm{s}/\Omega)^2} = \rho_0 e^{-z^2/(2H^2)}$. See Armitage (2010) for the whole derivation.

[2] Also referred to as the gas flux $\dot{\mathcal{M}}_\mathrm{g}$.

et al., 2016). However, given that disks are most likely turbulent (Youdin & Lithwick, 2007), turbulence may drive the radial gas transport. Different mechanisms could create turbulence, but regardless of the source, viscosity can be linearly scaled by a dimensionless parameter α between 0 and 1 (see α-disk model in section 3.1).

A further consideration is that describing the turbulence strength with a single α may not be appropriate in particular for different vertical layers of the disk (Drążkowska et al., 2022). It is expected that the midplane of the disk has lower turbulence than the upper layers because of the shielding from ionizing radiation. Typically, different parameters are used to differ the global α that describes the radial transport of the gas and the midplane turbulence $\alpha_{\rm t}$.

2.2 From dust to pebbles

The solid particles grow and are transported within the gas (Testi et al., 2014). Since solids are initially orbiting at Keplerian speed and the gas at sub-Keplerian one, the gas exerts a drag force on the solids. Depending on the size and position of the solids, they re-couple to the gas or drift inwards rapidly compared to the disk lifetime (Weidenschilling, 1977).

An important parameter to describe the dynamics of solids is the Stokes number St. It is a dimensionless parameter that quantifies the coupling time of a particle $t_{\rm stop}$ (i.e. the time that needs a particle to couple with the gas) in terms of the local orbital timescale,

$$\mathrm{St} = \mathrm{t_{stop}}\Omega_{\rm K}, \tag{2.3}$$

where $\Omega_{\rm K}$ is the Keplerian frequency (see eq. 2.1). In the outer part of the disk, the relation between the particle size $a_{\rm s}$ and its St can be written as (Lambrechts & Johansen, 2012)

$$\mathrm{St} = \frac{\pi}{2}\frac{\mathrm{a_s}\rho_{\rm s}}{\Sigma_{\rm g}}, \tag{2.4}$$

where $\rho_{\rm s}$ is its internal density, and $\Sigma_{\rm g}$ the gas surface density, which decreases with the radial distance. Therefore, the size of particles exhibiting the same aerodynamic behaviour (i.e. same St) reduces further away from the star.

Small particles ($\mathrm{St} \ll 1$) are well-coupled to the gas, orbiting at sub-Keplerian velocities and radially moving due to turbulence. For larger particles ($\mathrm{St} \lesssim 1$) or pebbles, it is harder to couple to the motion of the gas. Due to the drag force exerted by the gas, pebbles undergo radial drift. In addition, there is also a vertical transport of solids. Particles are not affected by the vertical force acting due to the vertical pressure gradient of the gas. However, particles do not fall to the midplane; they form a vertical structure that depends on the settling due to gravity and mixing effects due to the midplane turbulence (see fig. 2.2) (Testi et al., 2014). Dubrulle et al. (1995) calculated that vertical structure $H_{\rm p}$ for an equilibrium between settling and turbulence mixing effects,

$$H_{\rm p} = H\sqrt{\frac{\alpha_{\rm t}}{\alpha_{\rm t} + \mathrm{St}}}, \tag{2.5}$$

where H is the scale height of the gas (see eq. 2.2) and α_t is the midplane turbulence. This equation provides insight into the settling behaviour of pebbles, with larger pebbles showing greater decoupling from the vertical gas structure and settling more readily into the midplane. Conversely, the turbulence in the midplane has an inhibiting effect on settling. Regarding the growth of solids, the μm-sized primordial dust particles (or monomers) can stick together to form larger aggregates (Testi et al., 2014). The timescale for doubling the size is estimated to be $\tau \sim (Z_0 \Omega_K)^{-1}$(Brauer et al., 2008), where Z_0 is the initial dust-to-gas ratio, and Ω_K the Keplerian frequency. Hence, the timescale required to grow up from 1 μm to size a_s,

$$\tau_g \sim \frac{1}{Z_0 \Omega_K} \cdot \log_2 \left(\frac{a_s}{\mu m} \right). \tag{2.6}$$

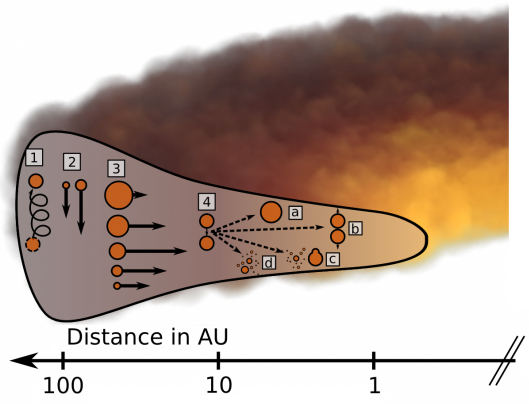

Figure 2.2: Transport of solids within the disk; 1) Radial or vertical mixing, 2) Vertical settling, 3) Radial Drift. 4) Growth and barriers; a) Sticking, b) Bouncing, c) Fragmentation with mass transfer, d) Fragmentation. Figure adapted from Testi et al. (2014).

The velocity at which particles collide is one of the factors that determines the growth, as when particles are driven by turbulence, their relative velocity increases with size or St ($\Delta v_{turb} \propto \sqrt{\alpha_t St} \cdot c_s$, Ormel & Cuzzi, 2007), and the pairwise collisions can result in fragmentation (Blum & Wurm, 2008). In models, this effect is described by the fragmentation velocity v_f, which is the maximum relative velocity between colliding pairs until they start to fragment. By equating the relative velocity with the fragmentation limit,

$$St_{frag} \approx \frac{1}{3\alpha_t} \left(\frac{v_f}{c_s} \right)^2, \tag{2.7}$$

establishes the maximum size at which a particle can grow (Birnstiel et al., 2009). This does not imply that particles always grow up to the fragmentation limit, as radial drift might hamper growth. The Stokes number of particles dominated by the radial drift is (Ida et al., 2016)

$$St_{drift} \approx \frac{\sqrt{3\pi}}{80} \frac{v_K}{\Delta v} Z_0, \tag{2.8}$$

where v_K is the Keplerian velocity, Δv the sub-Keplerian velocity and Z_0 is the initial dust-to-gas ratio. The maximum pebble-size at a certain location is the minimum between the fragmentation barrier and drift barrier, i.e. $St = \min(St_{frag}, St_{drift})$. The inner regions are mostly dominated by the fragmentation barrier, and the outer ones by the drift barrier.

Turbulence plays a key role in the growth of particles, as higher turbulence increases the relative velocity between particles, in addition to hindering the settling of particles into the

midplane (see eq. 2.5). This causes the particles to spread within a larger region, resulting in less frequent encounters, and therefore, reducing their growth rate (Misener et al., 2019). Therefore, particles within high turbulence regions grow more slowly and stop growing at smaller sizes.

Since particles grow to pebble sizes and then radially drift, a pebble flux $\dot{\mathcal{M}}_{\rm p}$ is defined to describe the carried mass by pebbles from the outer to the inner regions of the disk (Lambrechts & Johansen, 2014). In the pebble accretion scenario, the protoplanet grows by consuming pebbles from this flux. The flux is characterised by the aerodynamic properties of the pebbles (St) and the pebble-to-gas ratio (Z). The impact of varying these parameters has already been explored. For example, Drążkowska et al. (2021) showed that an inwards flux of small pebbles (or small St) lasts longer. Another example is that Lambrechts et al. (2019) showed that a high pebble flux favours the formation of giant planets, while a low flux leads to the formation of super-Earths. Arguably, the pebble flux characteristics shape the fate of planets, and therefore, its characterisation is highly relevant. We will address this again when we derive the model in section 3.2.

2.3 Protoplanetary growth

This section will focus on protoplanetary growth through the accumulation of solids and gas. The initial embryo most likely forms by a mechanism called the Streaming Instability (SI), which is based on the collapse of self-gravitating pebble clumps (Johansen et al., 2014). Planetesimals with different sizes can form in those collapses (e.g. Schäfer et al., 2017), and the embryo is the largest planetesimal of a population. In a standard model, the embryo starts growing by accreting planetesimals until it is massive enough to accrete pebbles more efficiently. Nevertheless, Lorek & Johansen (2022) analysed the growth of embryos via planetesimal accretion in the outer regions and found that planetesimals cannot maintain an efficient accretion rate beyond $5 - 10\,\mathrm{AU}$. In addition, Lyra et al. (2023) found that growth via pebble accretion is possible directly after the embryo formation by SI. Thus, we do not include planetesimal accretion in our model. We begin by examining the evolution of a typical initial embryo mass of $0.001 - 0.1\,\mathrm{M}_{\oplus}$ that could form directly by SI at large distances (e.g. Liu et al., 2020). The embryo is located in the midplane and undergoes pebble accretion (as shown in fig. 2.3). Once the core forms, we proceed to gas accretion.

2.3.1 Pebble accretion

In the pebble accretion scenario, a protoplanet grows by accreting pebbles drifting from outer regions. The efficiency of pebble accretion depends mostly on two factors: the protoplanet's mass and the pebble's Stokes number (see fig. 2.4). On the one hand, the protoplanet needs to be massive enough to settle particles down its gravitational well (see the difference between fig. 2.4 (a), (b), (c) and (d)). On the other hand, if $\mathrm{St} \ll 1$ particles are well-coupled to the gas (see fig. 2.4 (f)), and if $\mathrm{St} > 1$, the gas cannot effectively decelerate such large object (see fig. 2.4 (e)). Hence, a protoplanet accretes pebbles more efficiently when $\mathrm{St} \sim 0.001 - 0.1$ (Ormel, 2017; Drążkowska et al., 2022).

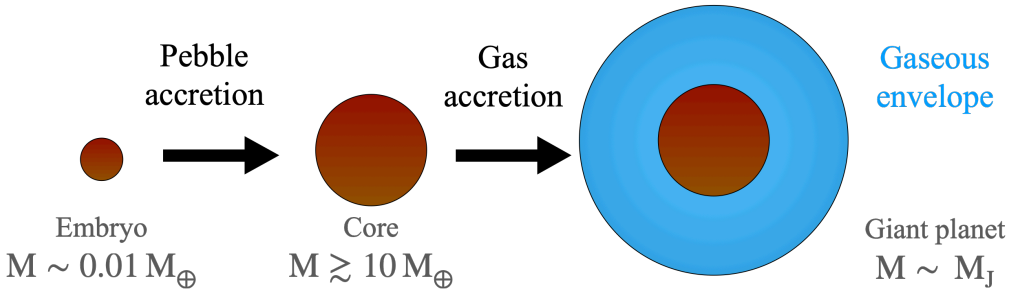

Figure 2.3: The core accretion scenario. The embryo starts growing via pebble accretion, and once the core forms, it will accrete gas to form the envelope until the gas disk dissipates.

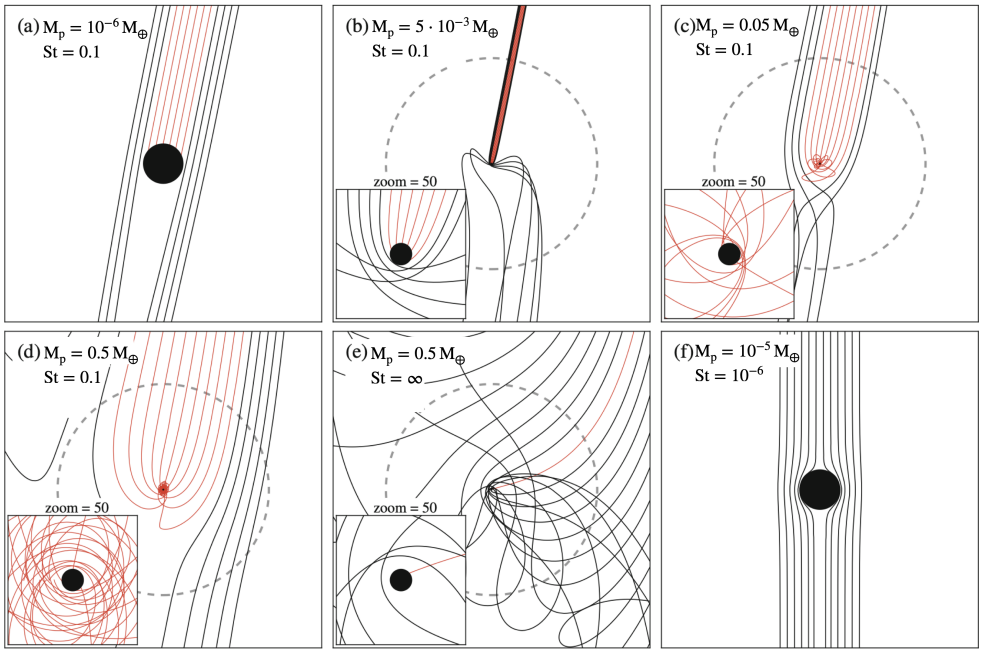

Figure 2.4: Different scenarios of protoplanet-pebble interaction, adapted from Ormel (2017). The red lines indicate the path of accreted pebbles. Only (c) and (d) are the ones qualified as pebble accretion scenarios, whose accretion radius extends close to the Hill radius (dashed circle). In (a) and (b), the protoplanet is not massive enough to attract pebbles efficiently. In (e), the gas drag does not decelerate the particles due to the large Stokes number. In (f), the particles are so small that they do not detach from the gas.

Some characteristics of the disk can also enhance or hinder pebble accretion. A high gas density enhances accretion, as it will decelerate pebbles more effectively (Ormel, 2017). We know that the gas density decreases with distance, so this does not benefit the growth of wide-orbit planets. A higher dust-to-gas ratio also enhances accretion, as it causes a stronger pebble flux. Turbulence is another factor to consider because, as we mentioned in the previous section, high turbulence hinders the settling of particles, and consequently, particles do not accumulate near the midplane. That can pose a challenge for low mass protoplanets to accrete them. In that regard, accretion is classified as either 2D or 3D, and

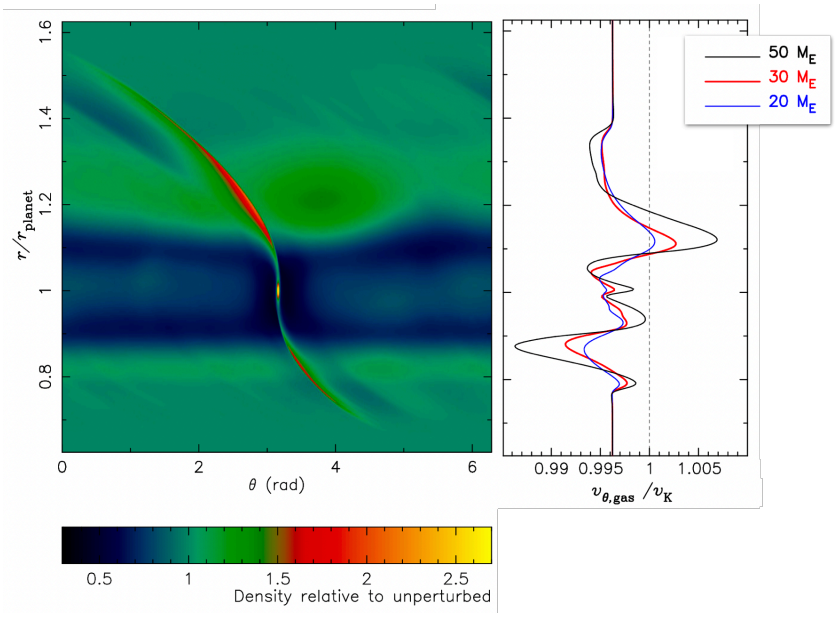

Figure 2.5: 3D simulation of the gravitational perturbation that an embedded protoplanet causes on the midplane gas (Lambrechts et al., 2014). On the left panel, they show the change in the gas surface density due to the presence of a protoplanet. They plot the full annulus ($\theta = 2\pi$) of a protoplanetary disk around the planet, located at a normalised distance of $r = 1$. On the right panel, they show how the orbital velocity of the gas with respect to the Keplerian one changes in the presence of protoplanets with different masses. In the outer edge of the gap, the gas rotates at super-Keplerian velocity, which halts pebbles coming from the outer regions.

we will delve into the specifics of this in section 3.3.1 when we discuss the model.

The body stops growing when the pebble flux is depleted (e.g. because all the pebbles have fallen to the centre or the gas dissipates) or when the core reaches its maximum mass and cannot accrete more pebbles. Lambrechts et al. (2014) showed via 3D numerical simulations that a massive protoplanet perturbs the disk, opening a gap that changes the radial pressure gradient in its vicinity (see fig. 2.5). Due to those perturbations, the gas in the outer regions of the protoplanet's orbit rotates at super-Keplerian velocities. Hence, pebbles are pushed outwards in that region and eventually accumulate on the outer edge. The threshold mass of a protoplanet, beyond which the pebble accretion process ceases, is referred to as the pebble isolation mass $M_{\rm iso}$.

2.3.2 Gas Accretion

During pebble accretion, the impacts of pebbles heat the atmosphere, preventing contraction and efficient gas accretion (Lambrechts et al., 2014). However, if the protoplanet reaches $M_{\rm iso}$ before the disk dispersal, the envelope starts to cool down by emitting radiation or luminosity. In response to the energy loss, it contracts via Kelvin-Helmholtz contraction, and new gas flows from the disk to refill the empty space.

In the first stage, the envelope has a relatively low mass, and therefore, the cooling and contraction process is slow and limits the gas accretion rate. Although the pebble flux is halted, dust particles well-coupled to the gas can still enter the envelope. The dust contributes to the opacity of the envelope κ and marginally hampers gas accretion (Ikoma et al., 2000).

When the mass of the envelope is similar to that of the core, the gas accretion starts to be very rapid. This mechanism is referred to as runaway gas accretion. As the protoplanetary envelope increases, the cooling and contraction rate becomes so rapid that the accretion rate starts to be limited by the extent of the disk where the protoplanet dominates, i.e. its Hill radius $R_{\rm H}$. Whilst accretion continues, the Hill sphere can become sufficiently large that the accretion rate is limited by the amount of gas that can enter the region from the disk (Ida et al., 2018). The runaway process stops when the gas disk depletes after the disk lifetime $t_{\rm f}$. By the time the gas disk dissipates, the protoplanet has already formed a gaseous envelope or primary atmosphere (Pollack et al., 1996).

2.4 Protoplanetary migration

When the protoplanet attains a mass of approximately $0.1\,{\rm M}_\oplus$, the gravitational interaction with the surrounding gas disk becomes significant, leading to notable effects on the dynamical evolution of the system (Kley & Nelson, 2012). The protoplanet generates two density waves; an inner leading and an outer trailing spiral arm. As a reaction, the protoplanet feels an exerted torque by each excited wave (see fig. 2.6). The internal torque exerted by the inner arm accelerates the protoplanet, while the external torque exerted by the outer one decelerates it. The external torque dominates over the inner one, and consequently, the protoplanet migrates inwards (Goldreich & Tremaine, 1978; Tanaka et al., 2002).

Initially, the migration speed scales linearly with the protoplanet's mass and with the unperturbed gas surface density[3] within the so-called type I migration regime (Tanaka et al., 2002). As already mentioned in section 2.3.1, a massive protoplanet opens a density gap along its orbit. If the gas does not flow across the gap, the gas will not exert any torque on the planet and the protoplanet will migrate at the speed of the gas viscous accretion (Lin & Papaloizou, 1986). This type of migration is referred to as the type II migration regime. Hydrodynamical simulations (e.g. Dürmann & Kley, 2015) showed, however, that gas can easily cross the gap. In Kanagawa et al. (2018), they described a new physical model where the torque exerted by the gas that crosses the gap depends on the surface density at the bottom of the gap instead of the unperturbed one of the type I regime. The surface density at the bottom of the gap decreases with increasing the protoplanet's mass, and therefore, considering the gap-opening slows down the protoplanet's migration.

[3]The *unperturbed* gas surface density is the aforementioned $\Sigma_{\rm g}$ in section 2.1, because the protoplanet is still not massive enough to perturb significantly its vicinity.

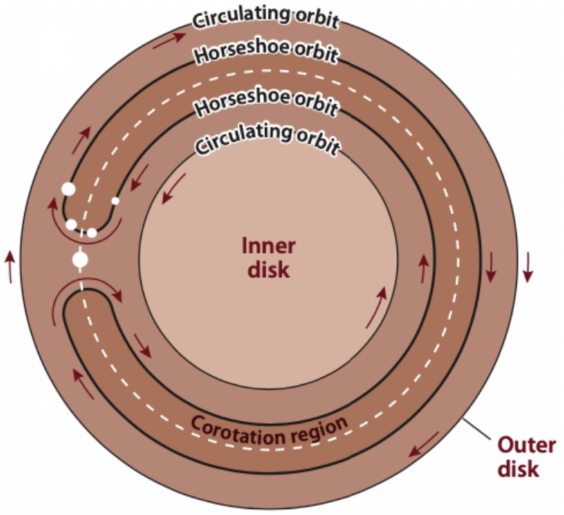

(a) The co-rotating frame of reference of the protoplanet. The gas rotates counterclockwise in the inner regions, and clockwise the outer ones.

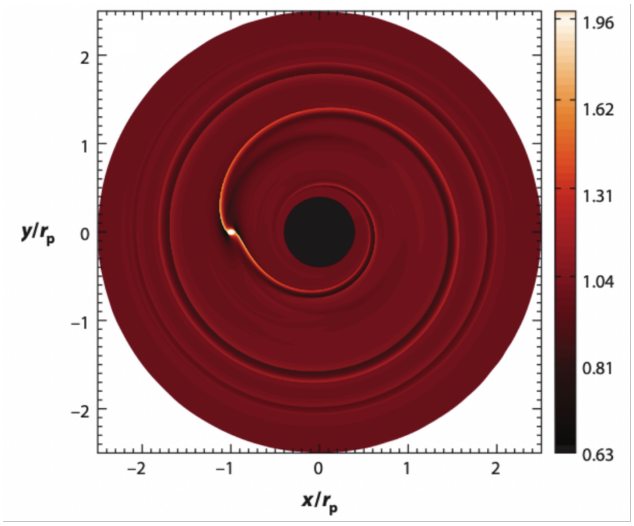

(b) The inner leading and the outer trailing spiral arms induced by the protoplanet. The colour map indicates the gas surface density.

Figure 2.6: Inwards migration due to planet-disk gravitational interaction (Kley & Nelson, 2012).

Although migration reduces when the planet reaches a large mass and opens a gap, rapid growth of the planet is necessary to create such a gap quickly. Migration is one of the major problems in retaining planets in outer regions and its impact will be considered in our model.

Chapter 3

Method

In this chapter, we explain the specific method that we adopt to describe the outer regions. First, we describe the model for the structure and evolution of the disk. Next, we introduce the analytical model of the pebble flux, including its derivation and numerical proof. Subsequently, we show the initial conditions for the simulations, followed by the model and method for calculating the growth and migration of the protoplanet.

3.1 Gas surface density and gas flux

The evolution of the gas surface density Σ_g of a geometrically thin Keplerian disk under the action of internal angular momentum transport is given by (Pringle, 1981)

$$\frac{\partial \Sigma_g}{\partial t} = \frac{3}{r}\frac{\partial}{\partial r}\left[r^{1/2}\frac{\partial}{\partial r}(\nu \Sigma_g r^{1/2})\right], \tag{3.1}$$

where ν is the turbulent viscosity. To derive $\Sigma_g(r,t)$, we begin by analysing the steady-state solution of eq. 3.1 ($\frac{\partial \Sigma_g}{\partial t} = 0$). We assume that the viscosity and disk temperature of the disk can be approximated with power-law functions of the radial distance r (Ida et al., 2016)

$$\nu \propto r^{\gamma}, \tag{3.2}$$

$$T_d \propto r^{-\zeta}, \tag{3.3}$$

and consequently, the sound speed and the scale height (see eq. 2.1 and 2.2) can be written as

$$c_s(r) = c_{s,1}\left(\frac{r}{\mathrm{AU}}\right)^{-\frac{\zeta}{2}}, \tag{3.4}$$

$$H(r) = \frac{c_{s,1}}{\Omega_{1\,\mathrm{AU}}}\left(\frac{r}{\mathrm{AU}}\right)^{-\frac{\zeta}{2}+\frac{3}{2}}, \tag{3.5}$$

where $c_{s,1}$ is the sound speed at 1 AU, and $\Omega_{1\,\mathrm{AU}}$ is the Keplerian frequency at 1 AU (see eq. 2.1). Following the α-disk model (Shakura & Sunyaev, 1973), we can relate the viscosity to the sound speed and the scale height. The turbulence cannot create structures larger than the smallest scale in the disk, which is generally the disk scale height. Similarly, the velocity

of the turbulent motion is limited to be no larger than the sound speed since supersonic motions result in shocks and rapid dissipation. Therefore, we write the turbulent viscosity as

$$\nu(r) = \alpha \cdot c_{\rm s}(r) H(r), \tag{3.6}$$

where α, or the global disk accretion coefficient, quantifies the efficiency of angular momentum transport due to turbulence (mentioned in section 2.1) and is expected to be less than 1. From eq. 3.2, 3.4, 3.5 and 3.6, we can relate the two power-law indexes $\gamma = \frac{3}{2} - \zeta$.

From the conservation of angular momentum of a narrow ring of material, the steady-state solution of eq. 3.1 can be written as a function of constant gas flux $\dot{\mathcal{M}}_{\rm g,0}$ across the disk and over time, also known as the gas accretion rate onto the star,

$$\Sigma_{\rm g}(r) = \frac{\dot{\mathcal{M}}_{\rm g,0}}{3\,\pi\,\nu(r)}. \tag{3.7}$$

We assume that at $t = t_0$ the surface density takes the form of the steady solution out to the characteristic initial disk size R_1, with an exponential cut-off at larger distances,

$$\Sigma_{\rm g}(r, t = t_0) = \frac{\dot{\mathcal{M}}_{\rm g,0}}{3\,\pi\,\nu_1\,\tilde{r}^{\gamma}} \exp\left(-\tilde{r}^{(2-\gamma)}\right), \tag{3.8}$$

where $\dot{\mathcal{M}}_{\rm g,0}$ in the non-steady solution is the initial gas accretion rate onto the star in the inner regions, $\nu_1 = \nu(R_1)$, $\tilde{r} = r/R_1$, and γ is the viscous power-index. Then, we use the self-similar solution (Lynden-Bell & Pringle, 1974)

$$\Sigma_{\rm g}(r, t) = \frac{\dot{\mathcal{M}}_{\rm g,0}}{3\,\pi\,\nu_1\,\tilde{r}^{\gamma}}\, T^{-\frac{5/2-\gamma}{2-\gamma}}\, \exp\left(\frac{-\tilde{r}^{(2-\gamma)}}{T}\right), \tag{3.9}$$

where T is the dimensionless time

$$T \equiv \frac{t - t_0}{t_s} + 1. \tag{3.10}$$

Here, $t_{\rm s}$ is the viscous timescale of the gas at radial distance R_1, which characterises the timespan required for the gas to evolve radially. It is defined as

$$t_{\rm s} \equiv \frac{1}{3(2-\gamma)^2} \frac{R_1^2}{\nu_1}. \tag{3.11}$$

Once we have the analytical expression of $\Sigma_{\rm g}$, we can derive the expression of the gas flux $\dot{\mathcal{M}}_{\rm g}$. By definition, the gas flux is (Armitage, 2010)

$$\dot{\mathcal{M}}_{\rm g} \equiv -2\pi r v_{\rm r,g} \Sigma_{\rm g} \tag{3.12}$$

where $v_{\rm r,g}$ is the radial velocity of the gas. The negative sign is due to the definition of a positive flux as being directed towards the star. From the continuity equation of a flux,

$$r\frac{\partial\,\Sigma_{\rm g}}{\partial\,t} + \frac{\partial\,(r\;v_{\rm r,g}\;\Sigma_{\rm g})}{\partial\,r} = r\frac{\partial\,\Sigma_{\rm g}}{\partial\,t} - \frac{1}{2\pi}\frac{\partial\,\dot{\mathcal{M}}_{\rm g}}{\partial\,r} = 0 \tag{3.13}$$

Hence, by replacing eq. 3.9 in the continuity equation and solving it, we get the expression for the gas mass flux (Hartmann et al., 1998),

$$\dot{\mathcal{M}}_{\rm g}(r,t) = \dot{\mathcal{M}}_{\rm g,0}\, T^{-\frac{5/2-\gamma}{2-\gamma}} \exp\left(-\frac{\tilde{r}^{(2-\gamma)}}{T}\right) \times \left[1 - 2(2-\gamma)\frac{\tilde{r}^{(2-\gamma)}}{T}\right]. \tag{3.14}$$

The expression changes sign at $R_{\rm t} = R_1 \left[\frac{T}{2(2-\gamma)}\right]^{\frac{1}{(2-\gamma)}}$. For $r < R_{\rm t}$ the gas accretes towards the star, and for $r > R_{\rm t}$ it expands outwards. Replacing eq. 3.9 and 3.14 in eq. 3.12, we derive the radial velocity of the gas,

$$v_{\rm r,g} = -\frac{3}{2}\frac{\nu}{r} \times \left[1 - 2(2-\gamma)\frac{\tilde{r}^{(2-\gamma)}}{T}\right]. \tag{3.15}$$

To identify multiple unknown values of parameters that emerged in this section, we will utilise relevant literature as a reference to obtain their fiducial values. For simplicity, we will focus only on Sun-like stars $M_* \sim M_\odot$ and assume that their mass remains constant. Beyond a few AU, the main heat source of the disk is the irradiation from the central star (Ida et al., 2016). According to the empirical fitting in Garaud & Lin (2007), $\zeta \approx \frac{3}{7}$, and consequently, $\gamma \approx \frac{15}{14}$. As a fiducial value for the sound speed $c_{\rm s,1} \sim 650\,{\rm m\,s^{-1}}$ in eq. 3.4 for a Sun-like star (Johansen et al., 2019) and $\Omega_{1\,\rm AU} \sim 2\pi\,{\rm yr^{-1}}$. In Hartmann et al. (1998), they estimated from fitting observational data for Sun-like stars that the gas accretion rate at early stages (e.g. $t_0 \sim 0.2\,{\rm Myr}$) is $\dot{\mathcal{M}}_{\rm g,0} \sim 10^{-7}\ {\rm M_\odot\,yr^{-1}}$ and that drops to $\sim 10^{-8}\ {\rm M_\odot\,yr^{-1}}$ over a few Myr. They also estimated that $\alpha \sim 0.01$. For the midplane turbulence, however, we choose $\alpha_{\rm t} \sim 10^{-4}$ as a fiducial value, as a low turbulence has been inferred from dust observations in the outer regions (Pinte et al., 2022). The total disk mass from eq. 3.9,

$$\begin{aligned}
M_{\rm g}(t) &= \int_0^\infty 2\pi r \Sigma_{\rm g}(r,t)\, dr = \frac{2}{3}\frac{\dot{\mathcal{M}}_{g,0}}{\nu_1}\frac{R_1^2}{(2-\gamma)} T^{-\frac{1}{2(2-\gamma)}} \\
&= \frac{2}{3}\frac{\dot{\mathcal{M}}_{g,0}}{\alpha c_{\rm s,1}^2\, \Omega_{1\,\rm AU}^{-1} \left(\frac{R_1}{1\,\rm AU}\right)^\gamma}\frac{R_1^2}{(2-\gamma)} T^{-\frac{1}{2(2-\gamma)}} \\
&\approx 0.16 \cdot {\rm M_\odot} \left(\frac{\alpha}{0.01}\right)^{-1} \left(\frac{\dot{\mathcal{M}}_{\rm g,0}}{10^{-7}\ {\rm M_\odot\,yr^{-1}}}\right) \left(\frac{c_{\rm s,1}}{650\ {\rm m\,s^{-1}}}\right)^{-2} \left(\frac{M_*}{1\ {\rm M_\odot}}\right)^{\frac{1}{2}} \times \\
&\times 100^{\frac{15}{14}-\gamma} \cdot \left(\frac{R_1}{100\,\rm AU}\right)^{2-\gamma} T^{-\frac{1}{2(2-\gamma)}}
\end{aligned} \tag{3.16}$$

For a typical initial disk mass of $M_{\rm disk} \sim 0.1\,{\rm M_\odot}$ and $M_{\rm disk} \sim 0.2\,{\rm M_\odot}$, from fiducial values we get initial disk sizes of $R_1 \sim 60\,{\rm AU}$ and $R_1 \sim 120\,{\rm AU}$ respectively. As a fiducial value we choose the typical disk size $R_1 \sim 100\,{\rm AU}$ (Williams & Cieza, 2011). These fiducial values correspond to a stable disk. When the disk is not stable, the self-gravity of the disk becomes relevant, and it can undergo local collapses. The Toomre's parameter $Q \approx \frac{c_{\rm s}\,\Omega}{\pi\, G\, \Sigma_{\rm g}}$ is used as the criteria to calculate the stability of the disk; the disk is stable if $Q \gtrsim 2$ across the whole disk (Armitage, 2010). All the fiducial values are listed in appendix A.

In fig. 3.1, we plot the gas surface density and the gas flux described by eq. 3.9 and 3.14. In this figure, we see that, when the initial disk size is set to $R_1 = 100\,{\rm AU}$, the outward

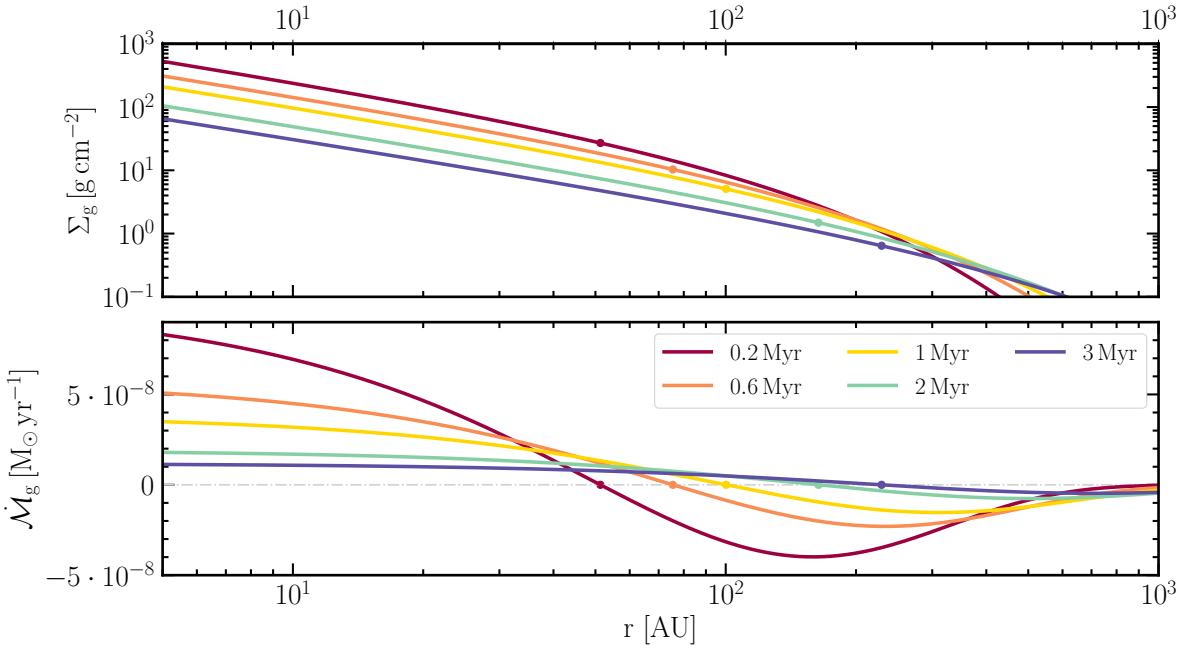

Figure 3.1: Gas density and gas flux over time according to eq. 3.9 and eq. 3.14, respectively. The dots represent the radial distance where $\dot{\mathcal{M}}_g$ vanishes. We use the fiducial values from table 1.

flux initially emerges at a radius greater than 50 AU, and then gradually moves outwards, reaching 100 AU before ~ 2 Myr. Thus, considering the momentum redistribution of the gas is relevant for protoplanets forming at large distances.

3.2 Pebble flux

The pebble flux describes the rate of pebble mass passing through an annulus at a distance r from the star. Numerical models that estimate the pebble flux (e.g. Brauer et al., 2008; Birnstiel et al., 2010) are computationally expensive and hinder the testing of various planet-forming scenarios, which is the aim of our work. Therefore, in this section, we develop a new analytical description. We introduce the general model of the dynamics of solid particles in section 3.2.1, followed by the derivation of the novel analytical model in section 3.2.2 and its computational test in section 3.2.3.

3.2.1 Dynamics of solid particles

Similarly to eq. 3.12, the pebble flux is defined as

$$\dot{\mathcal{M}}_p \equiv -2\pi r v_{r,p} \Sigma_p, \tag{3.17}$$

where $v_{\rm r,p}$ is the radial velocity of pebbles (Weidenschilling, 1977),

$$v_{\rm r,p} = \frac{v_{\rm r,g}}{1+{\rm St}^2} - \frac{2\Delta v\,{\rm St}}{1+{\rm St}^2}. \tag{3.18}$$

Here, St is the Stokes number (see section 2.2), $v_{\rm r,g}$ is the radial velocity of the gas (see eq. 3.15) and Δv quantifies the sub-Keplerian velocity reduction of the gas ($v_{\phi,\rm g} \approx v_{\rm K} - \Delta v$),

$$\Delta v = -\frac{1}{2}\left(\frac{H}{r}\right)\frac{\partial \ln P}{\partial \ln r} c_{\rm s} = \frac{1}{2}\left(\frac{H}{r}\right)\chi c_{\rm s}. \tag{3.19}$$

We denote the negative logarithmic pressure gradient in the midplane as χ. Assuming an ideal gas ($P \propto \frac{\Sigma_{\rm g}}{H} T_{\rm d}$) and using eq. 2.2, 3.3 and 3.9,

$$\chi \equiv -\frac{\partial \ln P}{\partial \ln r} = \gamma + \frac{\zeta}{2} + \frac{3}{2} + (2-\gamma)\frac{\tilde{r}^{\,(2-\gamma)}}{T} = \chi_0 + (2-\gamma)\frac{\tilde{r}^{\,(2-\gamma)}}{T} \tag{3.20}$$

where γ and ζ are the power-law indices of the viscosity and temperature respectively, $\tilde{r} = r/R_1$, and T is the dimensionless time (see eq. 3.10). The first term in eq. 3.18 describes the advection mode of transport that occurs when the gas flux drags solid particles, and the second term corresponds to the radial drift towards higher pressure. In fig. 3.2, we plot the radial velocity of solids depending on St. When ${\rm St} \sim \alpha \sim 0.01$ solids decouple from the gas[1], drifting faster than the gas towards the star. After a maximum when ${\rm St} \sim 1$, the radial velocity decreases again, as massive bodies have greater inertia. Since the drift and fragmentation barriers limit the pebble growth via coagulation (see section 2.2), generally, pebbles do not reach ${\rm St} \sim 1$.

As in the previous section, we discuss the fiducial values from the literature for parameters related to the pebble flux. First, it is thought that the initial dust-to-gas ratio is roughly the same as the one in the ISM (Feng & Krumholz, 2014). A typical standard value is $Z_0 \sim 0.01$. Assuming that solids do not decouple from the gas until t_0 (because their size is initially small), the initial pebble-to-gas ratio is equal to the initial dust-to-gas ratio, i.e. $Z(t_0) = Z_0 \sim 0.01$. Z evolves with time once pebbles start to decouple from the gas. As mentioned in section 2.2, ${\rm St} = \min({\rm St}_{\rm drift}, {\rm St}_{\rm frag})$. Regarding ${\rm St}_{\rm frag}$ (see eq. 2.7), laboratory experiments done in Güttler et al. (2010) reported a value of $v_{\rm f} \sim 1\,{\rm m\,s^{-1}}$ for the fragmentation velocity of grain silicates [2]. For fiducial values, the outer regions $r \sim R_1$ are drift-limited (see fig. 3.3). Hence, we choose ${\rm St} \approx 0.03$. To calculate the size of solid particles (see eq. 2.4), we choose $\rho_{\rm dust} \sim 1\,{\rm g\,cm^{-3}}$ as a nominal value (Ida et al., 2016). According to observations in Ricci et al. (2010), they found evidence of solid particles as large as at least 1 mm in the outer regions of several young disks. The particle size according to eq. 2.4 is $a_{\rm s} \sim 2\,{\rm mm}$ at R_1. Therefore, the fiducial values are in line with observations. A particle at $R_1 \sim 100\,{\rm AU}$ grows up to 2 mm in $\sim 0.2\,{\rm Myr}$ (from eq. 2.6) and then starts drifting inwards. We will consider that in the outer regions the pebble flux starts depleting when $t_0 \sim 0.2\,{\rm Myr}$.

[1] In $v_{\rm r,p}/v_{\rm r,g}$, the radial drift term will depend on ${\rm St}/\alpha$.

[2] There is an ongoing debate about the value of $v_{\rm f}$, as the fragmentation threshold may depend on the particle composition and consequently the location in the disk (Drążkowska et al., 2022).

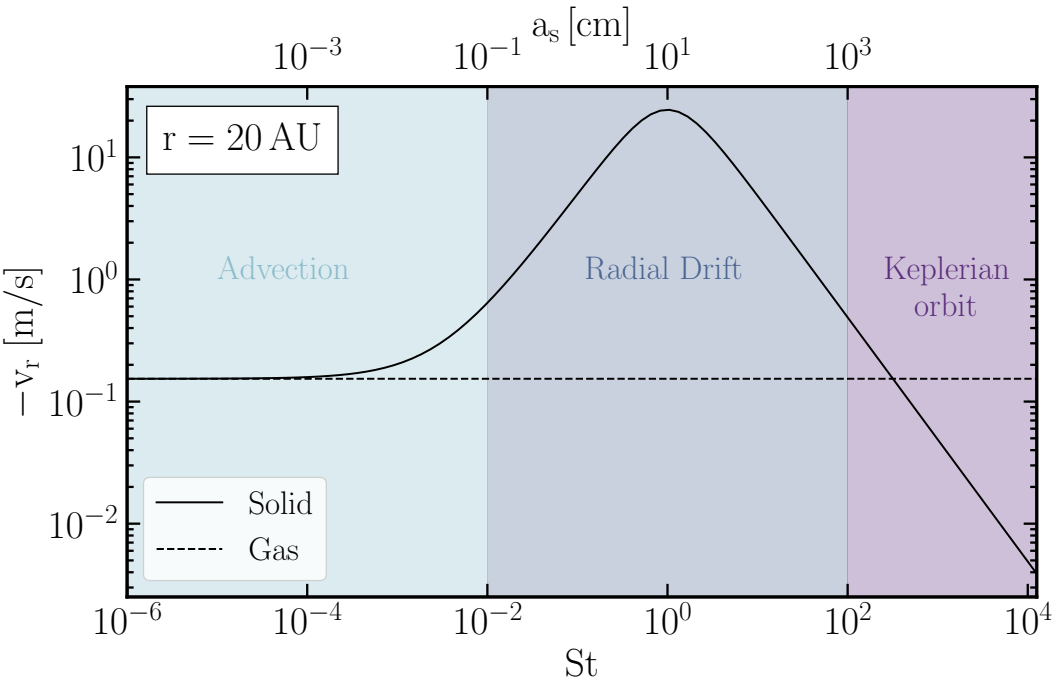

Figure 3.2: The inwards radial velocity of solids depending on their St or size a_s at 20 AU (see eq. 2.4 and eq. 3.18). The dashed line indicates the inwards radial velocity of the gas (see eq. 3.15). The colour ranges indicate the approximate regions describing what dominates the dynamics of solids. Small particles are well-coupled to the gas; particles with St between $\sim$ 0.01 and 100 undergo inwards radial drift; and for larger solids, the radial component of the velocity approaches 0, resulting in a purely Keplerian orbit. For the plot, we use fiducial values from appendix A.

Different models for the pebble flux $\dot{\mathcal{M}}_p$ can be derived depending on the assumptions. For example, in Johansen et al. (2019), they assumed that the ratio between the pebble and gas flux is constant. This approach is valid for small particles that are well-coupled to the gas. Nevertheless, with this model we are limited to analyse scenarios where pebbles grow only up to an small St, and the growth of protoplanets via small pebble accretion is too slow in the outer regions. Therefore, we will implement a model that considers that the pebble flux might deplete faster than the gas flux due to larger St.

3.2.2 Derivation of the analytical description

Defining the pebble-to-gas ratio or *metallicity* as

$$Z \equiv \frac{\Sigma_p}{\Sigma_g}, \tag{3.21}$$

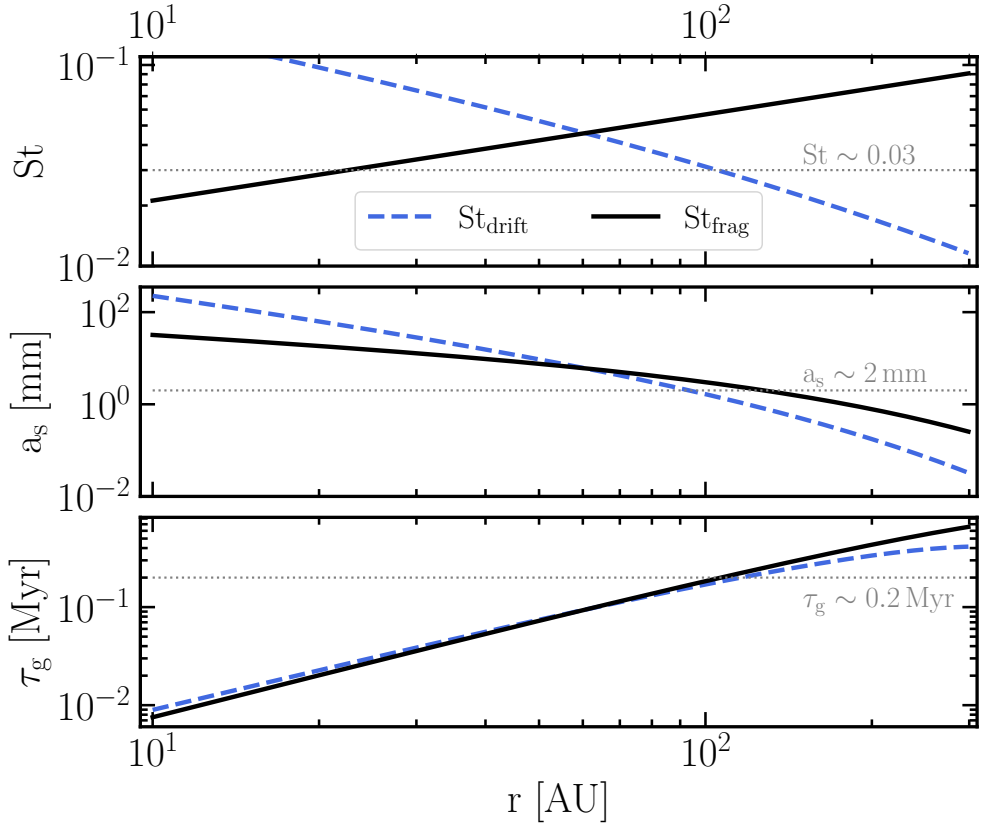

Figure 3.3: The fragmentation (black solid line) and drift limited (blue dashed line) Stokes numbers (see eq. 2.7 and 2.8 respectively), their corresponding particle size (see eq. 2.4) and the approximate timescale to grow up to that size (see eq. 2.6). The inner regions are limited by the fragmentation barrier and the outer ones by the drift barrier. When $r \sim R_1 \sim 100\,\mathrm{AU}$, $\mathrm{St} \sim 0.03$, $a_s \sim 2\,\mathrm{mm}$ and $\tau_g \sim 0.2\,\mathrm{Myr}$ for fiducial values (see appendix A).

the pebble flux can be written in terms of the metallicity by dividing eq. 3.12 and 3.17,

$$\dot{\mathcal{M}}_\mathrm{p} = Z \frac{v_\mathrm{r,p}}{v_\mathrm{r,g}} \dot{\mathcal{M}}_\mathrm{g}. \tag{3.22}$$

For simplification, we define $h(r,t) = \frac{v_\mathrm{r,p}}{v_\mathrm{r,g}} \dot{\mathcal{M}}_\mathrm{g}$ so that $\dot{\mathcal{M}}_\mathrm{p} = Z \cdot h(r,t)$. From eq. 3.14, 3.15 and 3.18,

$$\frac{v_\mathrm{r,p}}{v_\mathrm{r,g}} = \frac{1}{1+\mathrm{St}^2}\left(1 - \frac{2\Delta v \mathrm{St}}{v_\mathrm{r,g}}\right) = \frac{1}{1+\mathrm{St}^2}\left[1 + \frac{2}{3}\frac{\chi \mathrm{St}}{\alpha}\frac{1}{(1-2(2-\gamma)\frac{\tilde{r}^{(2-\gamma)}}{T})}\right], \tag{3.23}$$

$$h(r,t) = \frac{v_\mathrm{r,p}}{v_\mathrm{r,g}} \dot{\mathcal{M}}_\mathrm{g} = \frac{1}{1+\mathrm{St}^2}\left[1 - 2(2-\gamma)\frac{\tilde{r}^{(2-\gamma)}}{T} + \frac{2}{3}\frac{\chi \mathrm{St}}{\alpha}\right] \dot{\mathcal{M}}_{\mathrm{g},0} T^{-\frac{5/2-\gamma}{2-\gamma}} \exp\left(-\frac{\tilde{r}^{(2-\gamma)}}{T}\right), \tag{3.24}$$

where $\tilde{r} = r/R_1$ and T (see eq. 3.10) are the dimensionless spatial and time variables. χ depends on r and t (see eq. 3.20), and St can also depend on r and t. Defining

$$b(r,t) = \frac{2}{3}\frac{\chi(r,t)\mathrm{St(r,t)}}{\alpha}, \tag{3.25}$$

we can rewrite h,

$$h(r,t) = \frac{v_{\mathrm{r,p}}}{v_{\mathrm{r,g}}}\dot{\mathcal{M}}_{\mathrm{g}} = \frac{1}{1+\mathrm{St}^2}\left[1 - 2(2-\gamma)\frac{\tilde{r}^{\,(2-\gamma)}}{T} + b(r,t)\right]\dot{\mathcal{M}}_{\mathrm{g},0}T^{-\frac{5/2-\gamma}{2-\gamma}}\exp\left(-\frac{\tilde{r}^{\,(2-\gamma)}}{T}\right). \tag{3.26}$$

Since $h(r,t)$ is known, we want to derive $Z(r,t)$ so that we can get the analytical form of $\dot{\mathcal{M}}_{\mathrm{p}}$ in eq. 3.22. Neglecting the diffusivity of solid particles within the gas, the pebble flux fulfils its own continuity equation,

$$r\frac{\partial\,\Sigma_{\mathrm{p}}}{\partial\,t} - \frac{1}{2\pi}\frac{\partial\,\dot{\mathcal{M}}_{\mathrm{p}}}{\partial\,r} = 0. \tag{3.27}$$

We can rewrite this equation in terms of Z by replacing $\Sigma_{\mathrm{p}} = Z\Sigma_{\mathrm{g}}$ and $\dot{\mathcal{M}}_{\mathrm{p}} = Zh$ (see eq. 3.21 and 3.22). We make the change of variables from r and t to the dimensionless parameters $\tilde{r} = r/R_1$ and T (see eq. 3.10 and 3.11) respectively to simplify the equation. Applying the chain rule,

$$\frac{\partial}{\partial t} \equiv \frac{1}{t_{\mathrm{s}}}\frac{\partial}{\partial T} \equiv 3(2-\gamma)^2\frac{\nu_1}{R_1^2}\frac{\partial}{\partial T}, \qquad \frac{\partial}{\partial r} \equiv \frac{1}{R_1}\frac{\partial}{\partial\tilde{r}}. \tag{3.28}$$

The continuity equation, therefore, is

$$\begin{aligned} 3(2-\gamma)^2\frac{\nu_1}{R_1}\tilde{r}\frac{\partial(Z\cdot\Sigma_{\mathrm{g}})}{\partial T} - \frac{1}{2\pi}\frac{1}{R_1}\frac{\partial(Z\cdot h)}{\partial\tilde{r}} &= 0 \\ 3(2-\gamma)^2\nu_1\tilde{r}\left(Z\frac{\partial\Sigma_{\mathrm{g}}}{\partial T} + \Sigma_{\mathrm{g}}\frac{\partial Z}{\partial T}\right) - \frac{1}{2\pi}\left(Z\frac{\partial h}{\partial\tilde{r}} + h\frac{\partial Z}{\partial\tilde{r}}\right) &= 0. \end{aligned} \tag{3.29}$$

To solve the partial differential equation we substitute Σ_{g} and h (see eq. 3.9 and 3.26) and compute their (dimensionless) time and spatial derivatives respectively. The time derivative of Σ_{g} is

$$\frac{\partial\Sigma_{\mathrm{g}}}{\partial T} = \frac{\dot{\mathcal{M}}_{\mathrm{g},0}}{3\pi\nu_1}\tilde{r}^{-\gamma}T^{-\frac{5/2-\gamma}{2-\gamma}}\exp\left(-\frac{\tilde{r}^{\,(2-\gamma)}}{T}\right)\frac{1}{T}\left(-\frac{5/2-\gamma}{2-\gamma} + \frac{\tilde{r}^{\,(2-\gamma)}}{T}\right). \tag{3.30}$$

Computing $\frac{\partial h}{\partial\tilde{r}}$ is not trivial, and therefore, we make an approximation. The larger pebbles that we might find within a flux have St ~ 0.1. In that case $\frac{1}{\mathrm{St}^2+1} = 0.99$, and for lower St the value is even closer to one. Therefore, for simplicity $\frac{1}{\mathrm{St}^2+1} \sim 1$. Consequently, the spatial derivative is simplified as

$$\frac{\partial h}{\partial\tilde{r}} = \dot{\mathcal{M}}_{\mathrm{g},0}T^{-\frac{5/2-\gamma}{2-\gamma}}\exp\left(-\frac{\tilde{r}^{\,(2-\gamma)}}{T}\right)\left[\frac{\partial b}{\partial\tilde{r}} - (2-\gamma)\frac{\tilde{r}^{\,(1-\gamma)}}{T}\left(1 + 2(2-\gamma) - 2(2-\gamma)\frac{\tilde{r}^{\,(2-\gamma)}}{T} + b\right)\right]. \tag{3.31}$$

The general equation, therefore,

$$Z\frac{\tilde{r}^{\,(1-\gamma)}}{T}\left[\frac{(2-\gamma)}{2}b - \frac{T}{2\tilde{r}^{\,(1-\gamma)}}\frac{\partial b}{\partial\tilde{r}}\right] = -(2-\gamma)^2\tilde{r}^{\,(1-\gamma)}\frac{\partial Z}{\partial T} + \frac{1}{2}\left[1 + b - 2(2-\gamma)\frac{\tilde{r}^{\,(2-\gamma)}}{T}\right]\frac{\partial Z}{\partial\tilde{r}}. \tag{3.32}$$

This equation can be solved numerically given any initial conditions $Z(\tilde{r},1)=Z_0(\tilde{r})$ and expression for $\mathrm{St}(\tilde{r},T)$. However, solving eq. 3.32 analytically involves further limitations. Hence, for simplicity, we assume that St is constant and that $Z(\tilde{r},1)=Z_0$. In appendix B.1, we show why we could not solve the equation with $\mathrm{St}(\tilde{r})$. Applying the assumptions and substituting $\chi(\tilde{r},T)$ from eq. 3.20, we get that

$$b(\tilde{r},T)=\frac{2}{3}\frac{\mathrm{St}}{\alpha}\left(\chi_0+(2-\gamma)\frac{\tilde{r}^{\,(2-\gamma)}}{T}\right)=b_0\left(1+\frac{(2-\gamma)}{\chi_0}\frac{\tilde{r}^{\,(2-\gamma)}}{T}\right), \tag{3.33}$$

where $b_0=\frac{2}{3}\frac{\mathrm{St}\chi_0}{\alpha}$. The spatial derivative of $b(\tilde{r},T)$ is

$$\frac{\partial b}{\partial\tilde{r}}=\frac{2}{3}\frac{\mathrm{St}}{\alpha}(2-\gamma)^2\frac{\tilde{r}^{\,(1-\gamma)}}{T}=b_0\frac{(2-\gamma)^2}{\chi_0}\frac{\tilde{r}^{\,(1-\gamma)}}{T}. \tag{3.34}$$

Replacing $\frac{\partial b}{\partial\tilde{r}}$ in the general continuity equation 3.32, we get that

$$\begin{aligned} &Z\frac{\tilde{r}^{\,(1-\gamma)}}{T}\cdot\frac{(2-\gamma)}{2}b_0\left[1-\frac{2-\gamma}{\chi_0}\left(1-\frac{\tilde{r}^{\,(2-\gamma)}}{T}\right)\right]= \\ &=-(2-\gamma)^2\tilde{r}^{\,(1-\gamma)}\frac{\partial Z}{\partial T}+\frac{1}{2}\left[1+b_0+\left(\frac{b_0}{\chi_0}-2\right)(2-\gamma)\frac{\tilde{r}^{\,(2-\gamma)}}{T}\right]\frac{\partial Z}{\partial\tilde{r}}. \end{aligned} \tag{3.35}$$

This equation is a first-order linear Partial Differential Equation (PDE), which we will solve employing the Method of Characteristics for Non-Constant Coefficients (Riley et al., 1999). For simplicity, we will find the Z solution when $\gamma=1$, and generalise the expression afterwards. Therefore, the equation we want to solve is

$$\frac{1}{2}\left[1+b_0+\left(\frac{b_0}{\chi_0}-2\right)\frac{\tilde{r}}{T}\right]\frac{\partial Z}{\partial\tilde{r}}-\frac{\partial Z}{\partial T}-\frac{Z}{T}\frac{b_0}{2}\left[1-\frac{1}{\chi_0}+\frac{1}{\chi_0}\frac{\tilde{r}}{T}\right]=0. \tag{3.36}$$

We seek a solution of the form $Z(\tilde{r},T)=f(p)\cdot g(\tilde{r},T)$, where p is a function of $\tilde{r}$ and T and $g(\tilde{r},T)$ is any function that fulfills eq. 3.36. We rewrite the equation with

$$\frac{\partial Z}{\partial T}=\frac{\partial g}{\partial T}f(p)+g\frac{df}{dp}\frac{\partial p}{\partial T},\qquad \frac{\partial Z}{\partial\tilde{r}}=\frac{\partial g}{\partial\tilde{r}}f(p)+g\frac{df}{dp}\frac{\partial p}{\partial\tilde{r}}, \tag{3.37}$$

$$A(\tilde{r},T)=\frac{1}{2}\left[1+b_0+\left(\frac{b_0}{\chi_0}-2\right)\frac{\tilde{r}}{T}\right],\quad B(\tilde{r},T)=-1,\quad C(\tilde{r},T)=\frac{1}{T}\frac{b_0}{2}\left[1-\frac{1}{\chi_0}+\frac{1}{\chi_0}\frac{\tilde{r}}{T}\right], \tag{3.38}$$

which when substituting in the PDE we get

$$\begin{aligned} \left[A(\tilde{r},T)\frac{\partial g}{\partial\tilde{r}}+B(\tilde{r},T)\frac{\partial g}{\partial T}-C(\tilde{r},T)h\right]f(p)+\left[A(\tilde{r},T)\frac{\partial p}{\partial\tilde{r}}+B(\tilde{r},T)\frac{\partial p}{\partial T}\right]g\frac{df}{dp}=0, \\ \left[A(\tilde{r},T)\frac{\partial p}{\partial\tilde{r}}+B(\tilde{r},T)\frac{\partial p}{\partial T}\right]g\frac{df}{dp}=0, \\ A(\tilde{r},T)\frac{\partial p}{\partial\tilde{r}}+B(\tilde{r},T)\frac{\partial p}{\partial T}=0. \end{aligned} \tag{3.39}$$

In the first line, the first term vanishes as it is just the original PDE with Z replaced by g. Given that

$$dp = \frac{\partial p}{\partial \tilde{r}} d\tilde{r} + \frac{\partial p}{\partial T} dT, \tag{3.40}$$

this equation and eq. 3.39 become the same if we require that

$$\frac{d\tilde{r}}{A(\tilde{r}, T)} = \frac{dT}{B(\tilde{r}, T)}. \tag{3.41}$$

This is the characteristic equation, and the integration constant will be p. Hence, the first equation we need to solve is

$$\frac{d\tilde{r}}{\frac{1}{2}\left[1 + b_0 + \left(\frac{b_0}{\chi_0} - 2\right)\frac{\tilde{r}}{T}\right]} = -dT. \tag{3.42}$$

This equation is an homogeneous first-order Ordinary Differential Equation (ODE), and therefore, we can rewrite it in the form of $\frac{d\tilde{r}}{dT} = F(\frac{\tilde{r}}{T})$. An homogeneous ODE can be solved by

$$\frac{dT}{T} = \frac{du}{F(u) - u}, \tag{3.43}$$

where $u = \frac{\tilde{r}}{T}$ and $F(u) = \frac{d\tilde{r}}{dT}$. Integrating the equation, we get that

$$\tilde{r}(T) = -\left(1 + \frac{1}{b_0}\right)\chi_0 T + pT^{-\frac{b_0}{2\chi_0}+1}, \tag{3.44}$$

where p is the constant of integration. Rearranging the equation,

$$p = \left[\left(1 + \frac{1}{b_0}\right)\chi_0 + \frac{\tilde{r}}{T}\right] T^{\frac{b_0}{2\chi_0}}. \tag{3.45}$$

Thus, the general solution for the PDE is

$$Z(\tilde{r}, T) = g(\tilde{r}, T) f\left(\left[\left(1 + \frac{1}{b_0}\right)\chi_0 + \frac{\tilde{r}}{T}\right] T^{\frac{b_0}{2\chi_0}}\right). \tag{3.46}$$

To get the form of $Z(\tilde{r}, T)$ that fulfills the initial condition $Z(\tilde{r}, 1) = Z_0$, we will look for an adequate form of $g(\tilde{r}, T)$. We propose that it has the following structure

$$g(\tilde{r}, T) = cT^a \exp\left(b + \frac{\tilde{r}}{T}\right), \tag{3.47}$$

where a, b and c are unknown constants that can be calculated by replacing $g(\tilde{r}, T)$ in the PDE and applying the initial conditions. The partial derivatives of g,

$$\frac{\partial g}{\partial \tilde{r}} = cT^a \exp\left(b + \frac{\tilde{r}}{T}\right)\frac{1}{T} = \frac{g}{T}, \tag{3.48}$$

$$\frac{\partial g}{\partial T} = cT^a \exp\left(b + \frac{\tilde{r}}{T}\right)\left[\frac{a}{T} - \frac{\tilde{r}}{T^2}\right] = \frac{g}{T}\left[a - \frac{\tilde{r}}{T}\right]. \tag{3.49}$$

Replacing this in the PDE, we get that $a = \frac{1}{2} + \frac{b_0}{2\chi_0}$. b and c can be computed using the initial condition $Z(\tilde{r}, 1) = Z_0$. When $T = 1$,

$$g(\tilde{r}, 1) = c\,\exp\left(b + \tilde{r}\right), \quad f(p) = f\left(\left(1 + \frac{1}{b_0}\right)\chi_0 + \tilde{r}\right). \tag{3.50}$$

In order to get $Z(\tilde{r}, 1) = c\,\exp\left(b + \tilde{r}\right)\, f\left(\left(1 + \frac{1}{b_0}\right)\chi_0 + \tilde{r}\right) = Z_0$, the function f must take the form $f = \exp(-p)$, and therefore,

$$c = Z_0, \qquad b = \left(1 + \frac{1}{b_0}\right)\chi_0. \tag{3.51}$$

Setting everything together, we get the solution

$$Z(\tilde{r}, T) = Z_0 T^{\frac{1}{2} + \frac{b_0}{2\chi_0}} \exp\left\{ - \left[\chi_0 \left(1 + \frac{1}{b_0}\right) + \frac{\tilde{r}}{T}\right] \times \left[T^{b0/(2\chi_0)} - 1\right] \right\}. \tag{3.52}$$

From this equation we can get the general expression for any γ looking for a similar solution that fulfils eq. 3.35:

$$\boxed{Z(\tilde{r}, T) = Z_0 T^{\frac{1}{2(2-\gamma)} + \frac{b_0}{2\chi_0}} \exp\left\{ - \left[\frac{\chi_0}{(2-\gamma)} \left(1 + \frac{1}{b_0}\right) + \frac{\tilde{r}^{(2-\gamma)}}{T}\right] \times \left[T^{b_0/(2\chi_0)} - 1\right] \right\}} \tag{3.53}$$

A simplified expression of this solution can be derived by assuming that $\chi \approx \chi_0$, which is valid in the inner disk. From this assumption (and keeping St constant), $\frac{\partial b}{\partial r} = 0$, and therefore, the general equation 3.35 is further simplified. Since $b_0 = \frac{2}{3}\frac{\mathrm{St}}{\alpha}\chi_0$,

$$Z \frac{\tilde{r}^{\,(1-\gamma)}}{T} \frac{(2-\gamma)}{2} b_0 = -(2-\gamma)^2 \tilde{r}^{\,(1-\gamma)} \frac{\partial Z}{\partial T} + \frac{1}{2}\left[1 + b_0 - 2(2-\gamma)\frac{\tilde{r}^{\,(2-\gamma)}}{T}\right] \frac{\partial Z}{\partial \tilde{r}} \tag{3.54}$$

We realise there is a straightforward solution of this equation since if $\frac{\partial Z}{\partial \tilde{r}} = 0$, it turns out that the PDE converts into a ODE,

$$Z \frac{\tilde{r}^{\,(1-\gamma)}}{T} \frac{(2-\gamma)}{2} b_0 = -(2-\gamma)^2 \tilde{r}^{\,(1-\gamma)} \frac{\partial Z}{\partial T}, \tag{3.55}$$

$$\frac{Z}{T}\frac{1}{2} b_0 = -(2-\gamma)\frac{d\,Z}{d\,T}. \tag{3.56}$$

Therefore, $Z(\tilde{r}, T) = Z(T)$, and this is valid for our initial conditions as they do not depend on $\tilde{r}$. Integrating the ODE,

$$\boxed{Z(T) = Z_0 T^{-\frac{b_0}{2(2-\gamma)}} = Z_0 T^{-\frac{1}{2(2-\gamma)}\frac{2}{3}\frac{\chi_0 \mathrm{St}}{\alpha}}} \tag{3.57}$$

which is less intricate than eq. 3.53. We tried to derive $Z(r, t)$ alternatively (see appendix B.2) by some other assumptions, and we get the same expression as in eq. 3.57. Knowing

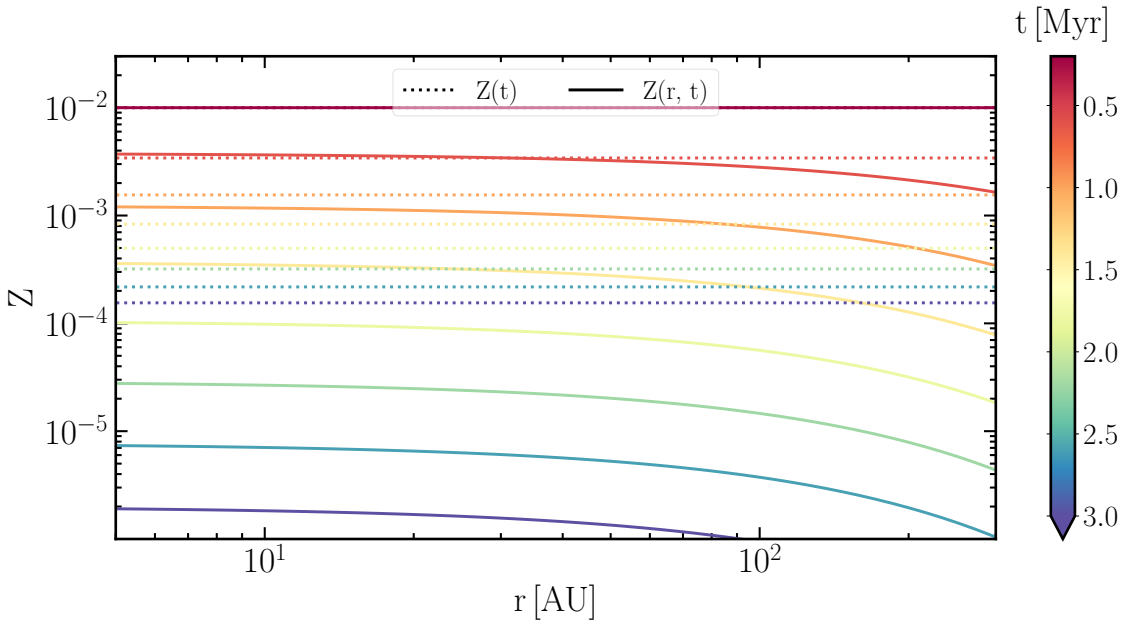

Figure 3.4: Analytical models of the evolution of the metallicity across the disk. We plot the two solutions; $Z(r,t)$ from eq. 3.53 with solid lines, and $Z(t)$ from eq. 3.57 with dotted lines. $Z(r,t) \approx Z(t)$ in the inner regions until the pebbles from the outer regions reach the inner ones. We use the fiducial values from appendix A.

the metallicity, we compute the pebble flux by eq. 3.22.

In fig. 3.4, we compare the evolving metallicity across the disk from eq. 3.53 and 3.57. For $Z(r,t)$ we see that, in the outer regions, the pebble flux depletion occurs faster than in the inner regions. Hence, $Z(t) \nsim Z(r,t)$ in the outer regions ($r \sim R_1$). In addition, in the inner regions $Z(t) > Z(r,t)$ after a while because, in the case of $Z(r,t)$, fewer pebbles are coming from the outer regions. The timescale until $Z(r,t) \approx Z(t)$ for inner regions will depend on St, as it will determine the radial drift of particles (see fig. 3.2), and therefore, the timescale at which outer particles reach the inner regions. We will adopt $Z(r,t)$ for our calculations, as it involves less approximations. However, in section 5, we will discuss the possibility that $Z(t)$ might be a marginally superior alternative.

3.2.3 Computational method vs. analytical description

To validate that the analytical expression $Z(r,t)$ from eq. 3.53 properly describes the dynamics of pebbles within the flux, we conducted a simulation of the evolution of the gas and drifting pebbles in a disk. The simulation involved tracking the trajectories of 40 000 particles - 20 000 representing the gas, while the remaining 20 000 represent the pebbles.

Firstly, a set of 20 000 positions was selected randomly on a logarithmic grid, each position

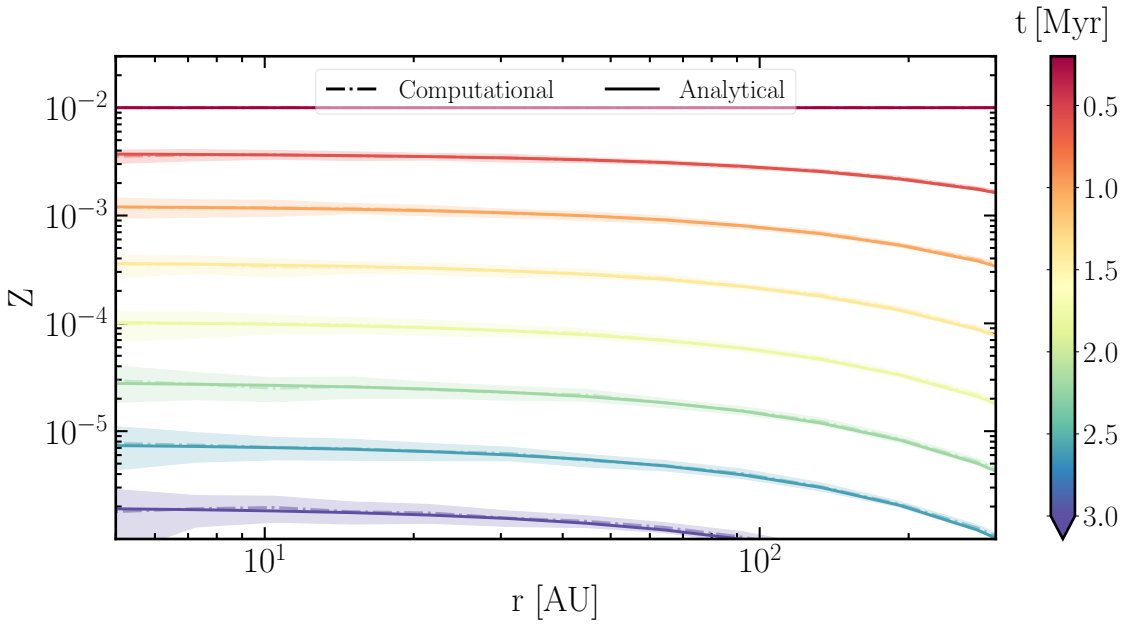

Figure 3.5: Comparison between the metallicity calculated computationally and analytically. The dash-dotted lines and the filled regions represent the mean value and standard deviation of the computational results. The solid lines represent the analytical expression (see eq. 3.53). We use the fiducial values from appendix A.

being occupied by a gas particle and a pebble particle. To determine the mass represented by each particle, we identified its nearest neighbouring particles and computed the midpoint $r_{\rm mid}$ between the particle and its neighbour. The mass embedded between the particle's position and the midpoint was then calculated by

$$m_{\rm i,g} = |\int_{r_{\rm mid}}^{r_{\rm i}} 2\pi r \Sigma_{\rm g}(r, t_0)\, dr|, \tag{3.58}$$

which was assigned as the mass of the gas particle, and

$$m_{\rm i,p} = |\int_{r_{\rm mid}}^{r_{\rm i}} 2\pi r Z_0 \Sigma_{\rm g}(r, t_0)\, dr|, \tag{3.59}$$

for the pebble one. Consequently, we are enforcing the assumption that $Z(r, t_0) = Z_0$. Moreover, we assign the same Stokes number St to all pebble particles since we assumed a constant St to obtain $Z(r, t)$. Once particles are initialised, we employed the explicit Euler method to compute their evolution. The position of the i^{th} particle at the n^{th} time-step is given by

$$r_{\rm i,g}^{(n)} = r_{\rm i,g}^{(n-1)} + v_{\rm i,r,g}^{(n-1)} h, \tag{3.60}$$

$$r_{\rm i,p}^{(n)} = r_{\rm i,p}^{(n-1)} + v_{\rm i,r,p}^{(n-1)} h, \tag{3.61}$$

where $h = t^{(n)} - t^{(n-1)}$ is the constant time-step (we chose $h = 5 \cdot 10^{-3}$ Myr), and to compute $v_{\rm i,r,g}^{(n-1)}$ and $v_{\rm i,r,p}^{(n-1)}$ we used eq. 3.15 and 3.18 respectively.

After calculating the evolution of each particle at the n^{th} time-step, we divided the disk in $\sim$ 20 bins and summed the gas and pebble mass of the particles contained in each bin. Then, we calculated the pebble-to-gas density ratio in the j^{th} bin at the n^{th} time step by

$$Z_{\mathrm{j}}^{(n)} = \frac{\sum_{\mathrm{i}\in\mathrm{j\ at\ t^{(n)}}} m_{\mathrm{p,i}}}{\sum_{\mathrm{i}\in\mathrm{j\ at\ t^{(n)}}} m_{\mathrm{g,i}}} \tag{3.62}$$

By following this method, we calculated the metallicity evolution across the disk. To improve accuracy, we repeated the procedure 50 times. Fig. 3.5 displays the mean metallicity of 50 simulations and the standard deviation. Given the similarity between the analytical model and the mean result from the simulations and the small uncertainty, we conclude that under the assumptions of initial Z_0 being constant across the disk and St over time and across the disk, the analytical expression $Z(r,t)$ from eq. 3.53 provides an accurate description of the pebble dynamics.

3.3 Evolution of the protoplanet

Since the protoplanet grows via pebble and gas accretion while it migrates, in this section, we explain the specific model we use for describing this evolution. We display the pebble and gas growth rate $\dot{M}$ and migration rate $\dot{r}$ equations, which we will solve using simple numerical methods such as the Explicit Runge-Kutta method of order 2, already implemented in *scipy.integrate.solve_ivp* Python package.

For solving the numerical equation, we need the initial mass, location and formation time of the embryo; M_0, r_0 and $t_{0,\mathrm{p}}$. The initial time of the formation of the embryo can differ from that of the disk t_0. We presume that the embryo can be initialiased at any $t_{0,\mathrm{p}} \geq t_0$ and at any r_0. As a fiducial value, we set the typical initial mass value of $M_0 \sim 0.01\,\mathrm{M}_\oplus$ (Johansen et al., 2019).

3.3.1 Growth rate via pebble accretion

To formulate the growth rate via pebble accretion, two questions need to be addressed. Firstly, is the planetary mass sufficient to accrete from the complete layer of pebbles? Secondly, what physics governs the relative velocity between the protoplanet and pebbles? The answer to the first question will determine whether we can consider the accretion to be 2D or 3D. The second answer will determine whether the relative velocity is dominated by the gas (Bondi Regime) or the gravitational pull from the protoplanet (Hill regime). In this subsection, we will elaborate on the various regimes and their corresponding analytical growth rates.

Regarding the first aspect, in the 2D regime, the protoplanet is large enough to accrete from the complete layer of pebbles. Analytically, this means that the pebble-accretion radius R_{acc} is larger than the pebble scale height H_{p} (see eq. 2.5). The characteristics favouring the 2D accretion scenario are a large planet mass (so that accretion has a larger scope) and the settling of pebbles. In contrast, in the 3D regime, the embryo only has access to a fraction of

the pebble layer. Therefore, the efficiency in the 3D regime is lower than in the 2D regime. From Johansen & Lambrechts (2017), the expressions for the growth rate of the protoplanet in each regime are

$$\dot{M}_{\rm 2D} = 2R_{\rm acc}\Sigma_{\rm p}\delta v, \tag{3.63}$$

$$\dot{M}_{\rm 3D} = \pi R_{\rm acc}^2\rho_{\rm p}\delta v, \tag{3.64}$$

where $\Sigma_{\rm p}$ is the surface density of pebbles (see eq. 3.21), $\rho_{\rm p}$ is the pebble density in the midplane ($\rho_{\rm p} \approx \frac{1}{\sqrt{2\pi}}\frac{\Sigma_{\rm p}}{H_{\rm p}}$), and δv is the approach velocity between the pebble and the protoplanet, defined as

$$\delta v \equiv \Omega R_{\rm acc} + \Delta v, \tag{3.65}$$

where Δv is the sub-Keplerian velocity reduction of the gas (see eq. 3.19). For the transition between 3D and 2D to be continuous, $\dot{M}_{\rm 2D} = \dot{M}_{\rm 3D}$ at certain stage. From this equality we get that the transition occurs when

$$\frac{R_{\rm acc}}{H_{\rm p}} = \sqrt{\frac{8}{\pi}}. \tag{3.66}$$

To derive the analytical expression of the accretion radius $R_{\rm acc}$, we address the second question; depending on the mass of the protoplanet and the Stokes number, the relative velocity between the protoplanet and pebbles is determined either by sub-Keplerian gas flow ($\delta v \approx \Delta v$, Bondi regime, see eq. 3.19) or by the Keplerian shear ($\delta v \approx \Omega R_{\rm acc}$, Hill regime) (Lambrechts & Johansen, 2012). The Bondi and Hill radii of a protoplanet are defined as,

$$R_{\rm H} \equiv r\left(\frac{M}{3M_*}\right)^{1/3}, \tag{3.67}$$

$$R_{\rm B} \equiv \frac{GM}{\Delta v^2}, \tag{3.68}$$

where r and M are the position and mass of the protoplanet. If the relative velocity is dominated by the gas flow (Bondi regime), the encounter time is

$$t_{\rm enc,\,B} \equiv \frac{R_{\rm B}}{\Delta v}. \tag{3.69}$$

On the contrary, if the relative velocity is dominated by the gravity of the protoplanet,

$$t_{\rm enc,\,H} \equiv \frac{R_{\rm H}}{v_{\rm H}} = \frac{R_{\rm H}}{R_{\rm H}\Omega} = \Omega^{-1}. \tag{3.70}$$

For accretion, the pebble needs to change direction significantly in the encounter on a timescale that is shorter than the stopping time of pebbles $t_{\rm stop}$ (see eq. 2.3). Therefore, $t_{\rm stop}/t_{\rm enc} \lesssim 1$ for accretion. In Johansen & Lambrechts (2017), they derive a more accurate expression for the effective accretion radius in each regime (Johansen & Lambrechts, 2017),

$$R_{\rm acc} = \left(10\frac{t_{\rm stop}}{t_{\rm enc,H}}\right)^{1/3} R_{\rm H} = \left(\frac{\rm St}{0.1}\right)^{1/3} R_{\rm H} \qquad \text{Hill Regime} \tag{3.71}$$

$$R_{\rm acc} = \left(4\frac{t_{\rm stop}}{t_{\rm enc,B}}\right)^{1/2} R_{\rm B} = \left(\frac{4\ {\rm St}\ \Delta {\rm v}}{\Omega\ R_{\rm B}}\right)^{1/2} R_{\rm B} \qquad \text{Bondi Regime} \tag{3.72}$$

These expressions of $R_{\rm acc}$ are valid for pebble-sizes we will use (${\rm St} \lesssim 0.1$), but for larger values, the expressions need some readjustment (Johansen & Lambrechts, 2017).

By equating the two accretion radii, we can determine the transitional mass between the two regimes. This approach ensures a smooth and continuous growth rate during the transition from one regime to another,

$$M_{\rm t} = \frac{25}{144}\frac{\Delta v^3}{G\Omega}\frac{1}{\rm St}. \tag{3.73}$$

The accretion will occur in the Hill regime if $M \geq M_{\rm t}$ and in the Bondi regime if if $M < M_{\rm t}$.

In the literature, many pebble accretion models are based on the 2D Hill regime (see review by Drążkowska et al., 2022). Nevertheless, the transition between Bondi and Hill regimes shifts to larger protoplanet masses in the outer disk. In fig. 3.6, we plot the transition mass between 2D and 3D accretion and Bondi and Hill regime, and we see that the prevailing regime strongly depends on the location and mass of the protoplanet. Considering only the 2D Hill regime would lead to overestimated growth rates.

As mentioned in section 2.3.1, the protoplanet stops accreting pebbles when it reaches the pebble isolation mass ($M_{\rm iso}$). In Bitsch et al. (2018), they run 3D hydrodynamical simulations to measure $M_{\rm iso}$ and derive a simple scaling law,

$$M_{\rm iso}(r) = 25 M_\oplus \left(\frac{H/r}{0.05}\right)^3 \times \left[0.34\left(\frac{\log 10^{-3}}{\log \alpha_{\rm t}}\right)^4 + 0.66\right] \times \left[1 - \frac{-\chi_0 + 2.5}{6}\right], \tag{3.74}$$

where α_t is the midplane turbulence and χ_0 was calculated in eq. 3.20. $M_{\rm iso}$ scales with H/r (which increases with distance) since the non-linear perturbations that open the gap start approximately when the Hill Radius ($R_H \propto r$, see eq. 3.67) reaches the scale height H (Lambrechts et al., 2014). $M_{\rm iso}$ also increases with increasing $\alpha_{\rm t}$ because turbulent motions can give pebbles random kicks, hampering the trapping of pebbles at the outer edge of the gap. Furthermore, $M_{\rm iso}$ increases with increasing χ_0, as increasing the pressure gradient hinders the formation of an inverted pressure gradient zone. In our simulations, the mass growth due to pebble accretion will stop when $M \approx M_{\rm iso}$. Once the protoplanet reaches $M_{\rm iso}$, we consider the model for the gas accretion onto the protoplanet.

One of the issues we will find is that $M_{\rm iso}$ is very large in the outer regions; e.g. to reach $M_{\rm iso}$ at 50 AU the protoplanet needs to form a core of $\sim 50\,{\rm M}_\oplus$. In general, reaching $M_{\rm iso}$ is necessary to allow the protoplanet's envelope to cool down and accrete gas. Nevertheless, if the pebble flux depletes, the envelope can cool down without reaching $M_{\rm iso}$. Still, the protoplanet needs to be massive enough to accrete gas efficiently (e.g. $2 - 10\,{\rm M}_\oplus$), but we propose that when the pebble flux depletes, it undergoes gas accretion.

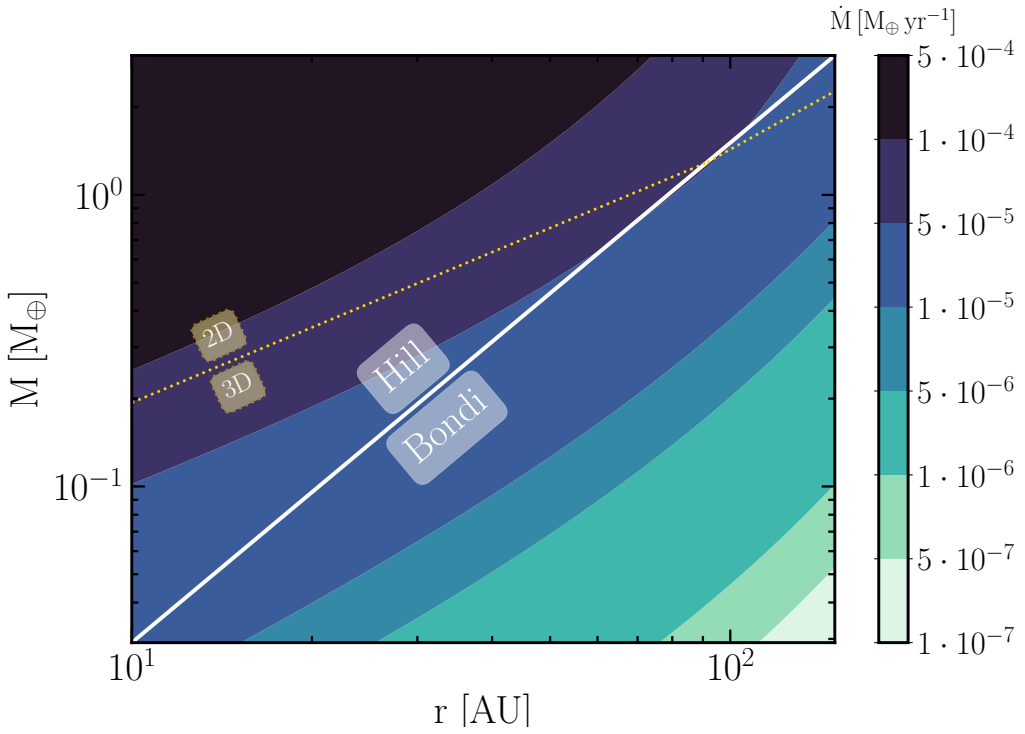

Figure 3.6: The growth rate $\dot{M}$ of a protoplanet via pebble accretion depending on its location and mass (see eq. 3.63 and 3.64). The solid white line indicates the transition between Hill and Bondi regimes (see eq. 3.73), and the dotted yellow line the transition between 2D and 3D (see eq. 3.66). The yellow line will be placed lower or higher on the y-axis if the midplane turbulence α_t decreases or increases respectively. The accretion rate increases as the protoplanet becomes larger and it gets closer to the star. Although it is not depicted in the plot, the accretion rate drops also over time, as the pebble surface density decreases. For fiducial values, see appendix 1.

As a first approach, we use a simple description to implement this; if the time required for doubling the mass of a protoplanet via pebble accretion is larger than a certain threshold $\tau_{\rm th}$, pebble accretion stops and the protoplanet starts accreting gas. The doubling-mass time is

$$\tau \approx \frac{M}{\dot{M}}, \tag{3.75}$$

where M is the mass of the protoplanet and $\dot{M}$ its growth rate via pebble accretion. When the pebble flux depletes, $\dot{M}$ decreases, and consequently, τ will approach $\tau_{\rm th}$. Even small protoplanets close to the embryo mass can fulfil $\tau > \tau_{\rm th}$. However, when M is very small, the gas accretion is not efficient, and the protoplanet will not grow.

$\tau_{\rm th}$ is unknown, and it might vary with the atmospheric pollution, as it might take longer to cool down if the envelope is highly polluted. In Lambrechts et al. (2014), they calculated the minimal accretion rates required to sustain a stable gas envelope, and from their calculations, we infer that $\tau_{\rm th}$ might lay down between 10 Myr and 100 Myr. We will take $\tau_{\rm th} = 100$ Myr

as a fiducial value.

3.3.2 Growth rate via gas accretion

We assume that the gas accretion starts with the contraction of the gaseous envelope at a rate suggested by Ikoma et al. (2000),

$$\dot{M}_{\rm KH} = 10^{-5}\ {\rm M}_\oplus\ {\rm yr}^{-1} \left(\frac{M}{10\ {\rm M}_\oplus}\right)^4 \left(\frac{\kappa}{0.1\ {\rm m}^2\ {\rm kg}^{-1}}\right)^{-1}, \tag{3.76}$$

where κ is the opacity of the envelope, and as already mentioned in section 2.3.2, the growth rate decreases with increasing the opacity. As a fiducial value we take $\kappa = 0.005\ {\rm m}^2\ {\rm kg}^{-1}$ (Johansen et al., 2019). Since the contraction accelerates at higher mass, the planet might eventually become so massive that growth will be restricted by the supply of gas flowing into its Hill sphere. Once this occurs, the growth rate of the protoplanet will be equal to the rate of gas supply, as described by Tanigawa & Tanaka (2016) and Ida et al. (2018),

$$\dot{M}_{\rm disk} = \frac{0.29}{3\pi}\left(\frac{H}{r}\right)^{-4}\left(\frac{M}{M_\star}\right)^{4/3}\frac{\dot{M}_{\rm g}}{\alpha}\frac{\Sigma_{\rm gap}}{\Sigma_{\rm g}}, \tag{3.77}$$

where $\Sigma_{\rm gap}$ is the surface density in the gap[3]. The ratio between the unperturbed and gap density is

$$\frac{\Sigma_{\rm gap}}{\Sigma_{\rm g}} = \frac{1}{1+0.04K}, \tag{3.78}$$

where

$$K = \left(\frac{M}{M_\star}\right)^2\left(\frac{H}{r}\right)^{-5}\alpha_{\rm t}^{-1}. \tag{3.79}$$

The growth rate cannot be larger than the global accretion rate of the gas flux within the disk $\dot{\mathcal{M}}_{\rm g}$ (see eq. 3.14). Indeed, in Lubow & D'Angelo (2006) they estimated that the maximum accretion rate onto the protoplanet is approximately 80% of the gas flux, and therefore,

$$\dot{M} = \min\left[\dot{M}_{\rm KH}, \dot{M}_{\rm disk}, 0.8\ \dot{\mathcal{M}}_{\rm g}\right]. \tag{3.80}$$

3.3.3 The protoplanet's migration

Generally, individual protoplanets undergo inwards radial migration while they grow. Planets that are not massive enough to open a gap in the gas fall into the type-I migration regime. To describe type-I migration, we use the standard scaling law as in Tanaka et al. (2002) for the migration speed of the protoplanet,

$$\dot{r} = -k_{\rm mig}\frac{M}{M_\star}\frac{\Sigma_{\rm g} r^2}{M_\star}\left(\frac{H}{r}\right)^{-2} v_{\rm K}, \tag{3.81}$$

[3]As the protoplanet opens a gap the amount of gas that enters the gap will be lower.

where v_K is the Keplerian velocity (see eq. 2.1) and k_mig the constant prefactor that was fitted using 3D numerical simulations in D'Angelo & Lubow (2010)

$$k_\mathrm{mig} = -2\,(1.36 + 0.62\gamma + 0.43\zeta). \tag{3.82}$$

γ and ζ are the already discussed power-values of the midplane temperature and viscosity respectively (see eq. 3.2 and 3.3).

When a planet grows up to a certain mass, according to Kanagawa et al. (2018), the disk–planet interaction becomes strong enough so that the planet opens a density gap along its orbit and migrates with the gap in the disk. Considering this effect, we will use the modified migration equation from Johansen et al. (2019),

$$\dot{r} = \frac{\dot{r}_\mathrm{I}}{1 + \left[M/\left(2.3 M_\mathrm{iso}\right)\right]^2}, \tag{3.83}$$

where $\dot{r}_\mathrm{I}$ is the classical type-I migration rate from eq. 3.81, and M_iso is the isolation mass from eq. 3.74. Combining the aforementioned pebble and gas accretion rate, the migration rate and the initial conditions, we are prepared to carry out simulations.

Chapter 4

Results & Discussion

Given the growth and migration rates, we numerically calculated the growth tracks (i.e. growth versus migration) of the protoplanets over time. First, we compare our simulations with previous studies to verify that our code works. We also compare growth tracks using different pebble flux models to demonstrate the need for our new model. Afterwards, we analyse different planet-forming scenarios by varying some parameters. Finally, we summarise our findings and the implications of our work.

4.1 Code testing and model comparison

We tested our code by comparing the outcome with the analytic growth tracks derived in Johansen et al. (2019) (see their eq. 20). Using a simplified model, the authors obtained the growth track $r(M)$ of a protoplanet that evolves over an unlimited timespan. First, we calculated growth tracks using their model to compare our outcome with the analytical expression. Afterwards, we incrementally assembled our model.

We enumerate the building blocks we utilised in the assembly, along with the expected outcome at each stage:

(a) Model adopted in Johansen et al. (2019). The protoplanet grows in the 2D Hill regime within a steady disk (see eq. 3.7). They simplified the expression of the approach velocity between the protoplanet and the pebbles (see eq. 3.65) such as $\delta v \approx R_{\mathrm{acc}}\Omega$. Moreover, they assumed that the pebble-to-gas ratio $Z = Z_0$ is constant in space and time. When adopting this model, we expect to obtain the same result as their analytical expression.

(b) Accretion in the 3D regime. It is expected that the growth slows down, especially for small St, due to the higher pebble scale height (see eq. 2.5).

(c) Disk evolution and exponential cut-off of the gas surface density. At growth timescales of a few $\sim 0.1\,\mathrm{Myr}$, we do not expect the disk evolution to have much impact, as the viscous timescale for fiducial values is $\sim 1\,\mathrm{Myr}$ (see eq. 3.11). The outer regions, however, will be strongly affected by the exponential cut-off of the density and by the outwards gas flux.

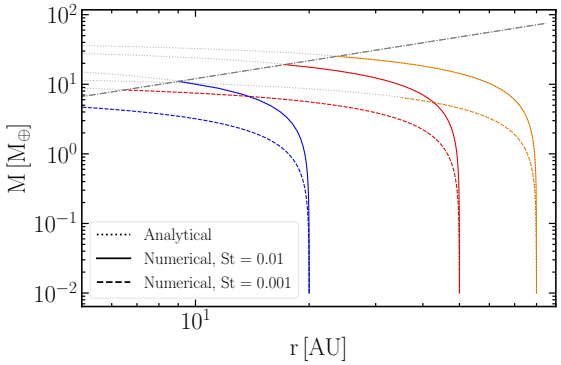

(a) Accretion in 2D Hill, the disk is steady and Z_0 is constant. We get the same growth track as the analytical one.

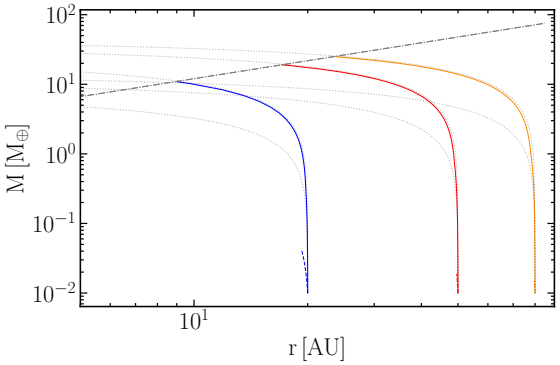

(b) Including accretion in 3D regime. The growth slows down especially for small St.

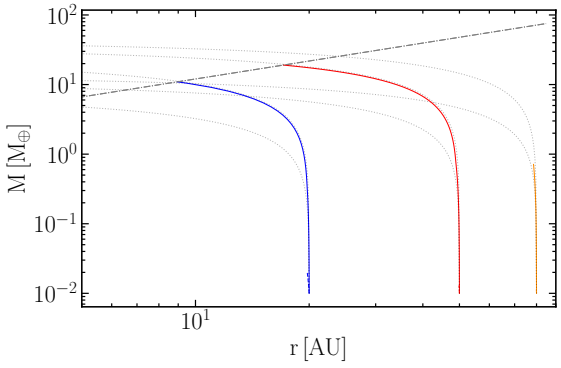

(c) Including disk evolution and exponential cut-off of the gas surface density. The growth slows down mainly in the outer region.

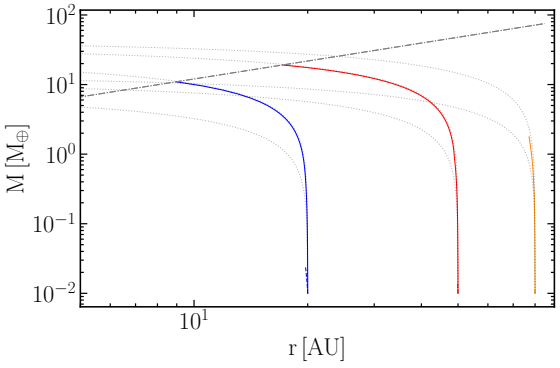

(d) Including accretion in Bondi regime. In this case, the growth increases due to the implementation of the complete form of δv from eq. 3.65.

Figure 4.1: Comparison between the analytical expression from Johansen et al. (2019) eq. 20 and the numerical calculation of the growth tracks. We incrementally assembled our model from (a) to (d). However, Z_0 is still constant. We employed St = 0.001 and St = 0.01. The embryos are initialised at 20, 50 and 80 AU, starting at $t_{0,\mathrm{p}} = 0.2$ Myr. We stopped the simulations at $t = 1$ Myr or before if they reach M_{iso} (grey dot-dashed line, see eq. 3.74). The analytical growth track is indicated with the grey dotted line, and the numerical ones with blue, red and orange lines.

(d) Accretion in Bondi regime. We considered the Bondi R_{acc} accretion radius below the transition mass (see eq. 3.73) and the complete expression for δv from eq. 3.65. By adding the Bondi R_{acc}, we anticipate a lower growth rate for low masses. However, the complete form of δv will increase the growth rates (see eq. 3.63 and 3.64). Therefore, when including the Bondi regime, the increase or decrease in the growth rate will depend on the balance between these counteracting effects.

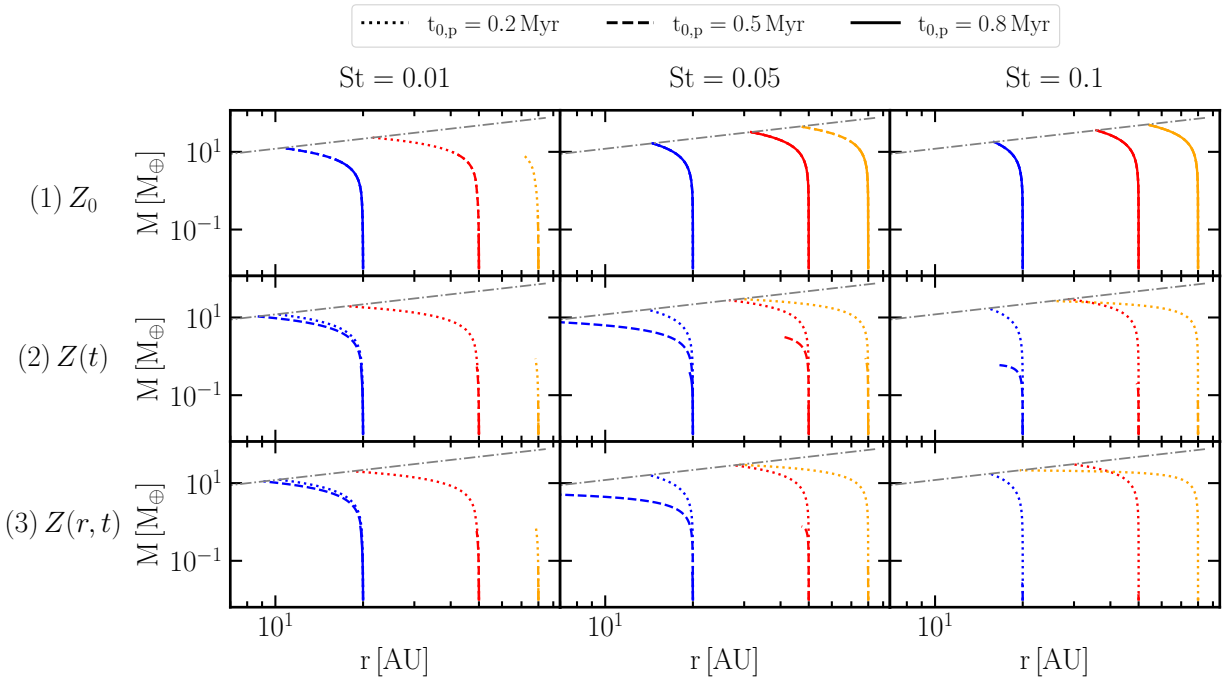

Figure 4.2: Row-by-row, we used a different pebble flux model; (1) Z_0, (2) $Z(t)$, and (3) $Z(r,t)$. The embryos are initialised at 20, 50 and 80 AU (indicated with blue, red and orange respectively), starting at $t_{0,p} = 0.2, 0.5$, and 0.8 Myr (indicated with dotted, dashed and solid lines respectively). We stopped the simulations at $t = 1$ Myr or when they reach M_{iso} (grey dot-dashed line, see eq. 3.74). Column-by-column, we used a different St. Model (1) and (2) overestimate the growth, especially for large St. However, model (2) yields outcomes that are more similar to those of model (3).

In fig. 4.1, we show the comparison between the analytical and numerical growth tracks. The variations from one model to another one are consistent with what we expected. Furthermore, fig. 4.1d shows that reaching M_{iso} beyond 20 AU is difficult, as migration overcomes the slow growth. A solution to that is faster growth with a stronger pebble flux. When St is large, pebbles drift faster, and consequently, the pebble flux is stronger but short-lasting. In section 3.2.2, we described a model for the pebble flux that implements the pebble flux depletion. We will now demonstrate how relevant it is to consider this depletion when we increase St of the pebble flux.

In fig. 4.2, we compare growth tracks when varying the model for the pebble flux: model (1) is the one with constant $Z = Z_0$; model (2) is the simplified expression we derived for $Z(t)$ (see eq. 3.57); and model (3) is the full solution $Z(r,t)$ (see eq. 3.53). We initialised the position and mass of the seeds as in fig. 4.1, but also varying the formation time $t_{0,p} = 0.2, 0.5$ and 0.8 Myr and St = 0.01, 0.05 and 0.1. In the results, we see that increasing St increases growth. When St = 0.01, the three models show similar growth tracks when $t_{0,p} = 0.2$ and 0.5 Myr. However, when $t_{0,p} = 0.8$ Myr, as the pebble flux depletes, growth is lower in model (2) and (3). When St = 0.05 and 0.1, given that the pebble flux depletes faster, model (1) greatly overestimates the final masses. Another interesting aspect is that when St = 0.1

in model (3), the embryo initialised at $r_0 = 80\,\mathrm{AU}$ reaches $M_{\rm iso}$ at distances closer to the star that the one initialised at $r_0 = 50\,\mathrm{AU}$. This happens not only because the growth is slower in the outer regions, but also because the depletion occurs earlier in the outermost regions. Overall, the new pebble flux model that considers depletion is crucial in modelling the formation of distant cores. From this point forward, we will adhere to model (3).

4.2 Which scenarios are most favourable for forming wide-orbit planets?

In this section, we show the results of many simulations. First, we vary the characteristics of the initial embryo, such as the position r_0, formation time $t_{0,\rm p}$ and mass M_0. We calculate the formation of their cores, followed by their gas accretion process. Next, we repeat the simulations but varying disk parameters such as the Stokes number, the metallicity, and the midplane turbulence. Afterwards, we implement the new gas accretion path. Finally, we discuss which scenarios lead to the formation of distant cores that can open gaps and which might yield wide-orbit planets at the end of the disk lifetime ($t_{\rm f} \sim 3\,\mathrm{Myr}$) [1].

4.2.1 Fiducial simulation

We simulated the evolutionary trajectories of 1000 protoplanets with an initial mass of $M_0 = 0.01\,\mathrm{M}_\oplus$, with random variations in their initial position r_0 within the range of 30 AU to 100 AU and formation time $t_{0,\rm p}$ between 0.2 Myr and 1.5 Myr. We initialised the disk of $R_1 = 100\,\mathrm{AU}$ at $t_0 = 0.2\,\mathrm{Myr}$, with a pebble flux characterised by a Stokes number $\mathrm{St} = 0.03$ and an initial metallicity $Z_0 = 0.01$, which gives an initial pebble reservoir of $M_{\rm peb,0} \sim 650\,\mathrm{M}_\oplus$ for fiducial values. We terminated the simulation when $t_{\rm f} = 3\,\mathrm{Myr}$. Subsequently, we repeated the simulations using the same initial position and formation time of the embryos but decreasing and increasing an order of magnitude their initial mass ($M_0 = 0.001$ and $0.1\,\mathrm{M}_\oplus$). In this section, we did not include the new path for gas accretion from eq. 3.75.

In fig. 4.3, we show the results of the core formation for fiducial values. The most distant cores form at $\sim 25{-}30\,\mathrm{AU}$ within the range $t \sim 0.35{-}0.7\,\mathrm{Myr}$. Since these protoplanets reach $M_{\rm iso}$, they open a gap at early stages near their location. The embryos of these protoplanets are initialised at the earliest stages ($t_{0,\rm p} \sim 0.2{-}0.3\,\mathrm{Myr}$), but it is hard to discern any clear pattern in the embryos' initial positions. Hence, in fig. 4.4, we plot the total solid mass of the protoplanets depending on their initial conditions. We divided the protoplanets into five different groups: (1) metal-rich cores $M_{\rm s} \geq 25\,\mathrm{M}_\oplus$; (2) standard cores $25\,\mathrm{M}_\oplus > M_{\rm s} \geq 10\,\mathrm{M}_\oplus$; (3) mini-Neptunes $10\,\mathrm{M}_\oplus > M_{\rm s} \geq 2\,\mathrm{M}_\oplus$; (4) ice planets $2\,\mathrm{M}_\oplus > M_{\rm s} \geq 0.1\,\mathrm{M}_\oplus$; and (5) minor bodies $0.1\,\mathrm{M}_\oplus > M_{\rm s}$. In the plot, we see that the core mass (and therefore the core formation distance) strongly depends on $t_{0,\rm p}$. Embryos

[1] For clarity: the initial time of the disk t_0 corresponds to the onset of the fiducial values and the drift of the pebbles; the embryo's formation time, $t_{0,\rm p}$, can occur at equivalent or later times than t_0; the core formation time denotes the point at which the protoplanet attains $M_{\rm iso}$ and opens a gap; the disk lifetime refers to the end of the simulation, when the planet is presumed to have ceased its evolution.

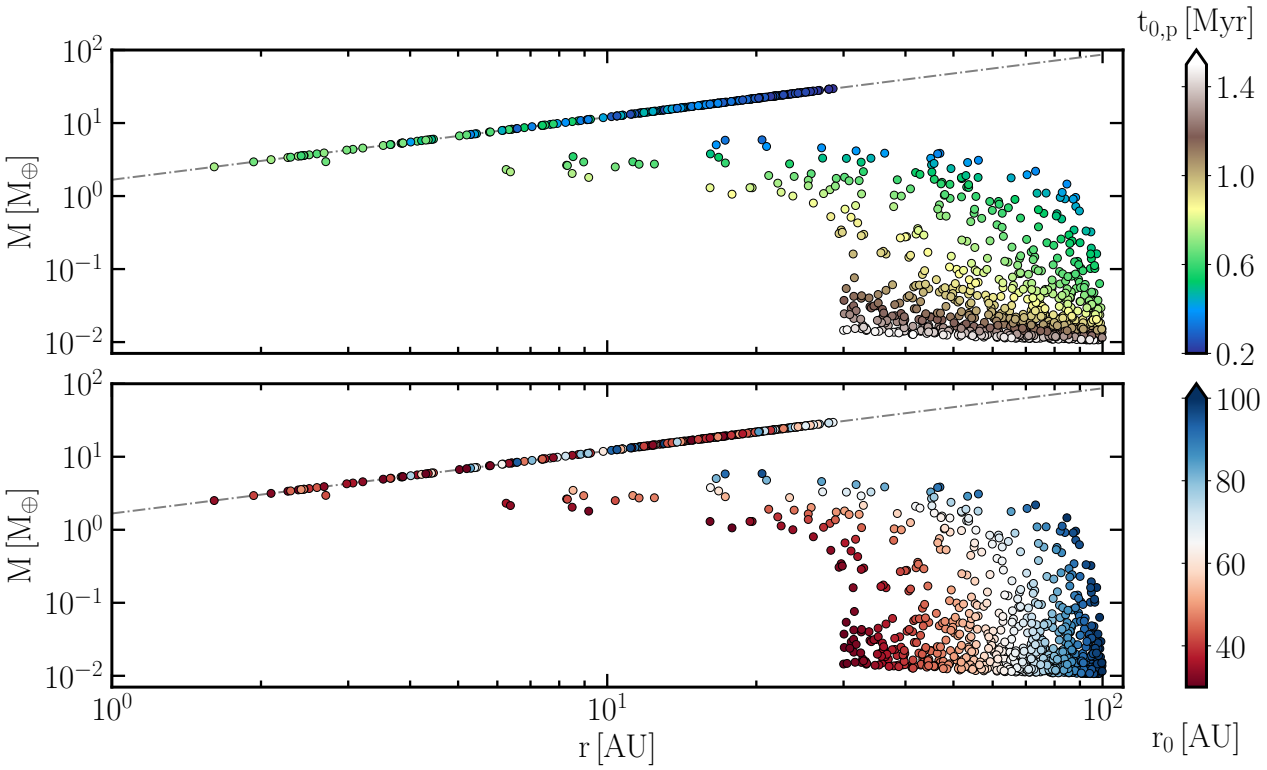

Figure 4.3: Evolution of 1000 protoplanets with an initial mass of $M_0 = 0.01\,M_\oplus$. Simulations stop after $t = 3$ Myr or if a protoplanet reaches $M_{\rm iso}$ (grey dot-dashed line, see eq. 3.74). The color-map in the top panel indicates the formation time of the embryos, and the one at the bottom indicates their initial position. The core of giant planets can form at ~ 30 AU the furthest. The embryos of those cores must form early and be initialised in the outer regions (see fig. 4.4 for a detailed description).

initialised at around ~ 30 AU have to form before $t_{0,\rm p} \sim 0.8$ Myr to reach $M_{\rm iso}$, and the embryos initialised at $\gtrsim 90$ AU, before $t_{0,\rm p} \sim 0.3$ Myr. Furthermore, the core mass decreases with increasing initial distance, except the region $50-80$ AU, where cores are metal-rich if the embryos are formed in the early stages ($t_{0,\rm p} \lesssim 0.3$ Myr). That occurs due to the same reason as in figure 4.2, in the 3rd row and 3rd column; the embryo initialised at 50 AU forms a more massive core than the embryos initialised at 20 AU and 80 AU.

In fig. 4.5, we show the same results as in fig. 4.3 but including gas accretion. First, we see a large dichotomy between gas giants and planets that do not reach $M_{\rm iso}$. The furthest gas giants are at ~ 6 AU and are as massive as $\sim 10\,M_{\rm Jup}$. Early-formed embryos that become gas giants end up orbiting at further distances and are more massive. Simultaneously, embryos initially located further from the star end up having a lower total mass. Those trends are more evident when plotting the total mass and final position of the gas giants depending on their initial conditions (see fig. 4.6). In figure 4.6b, we see that the final distance of embryos formed at early stages increases with increasing the initial distance. However, if the embryos form at later stages, outer embryos end up orbiting closer to the star due to the depletion of the pebble flux.

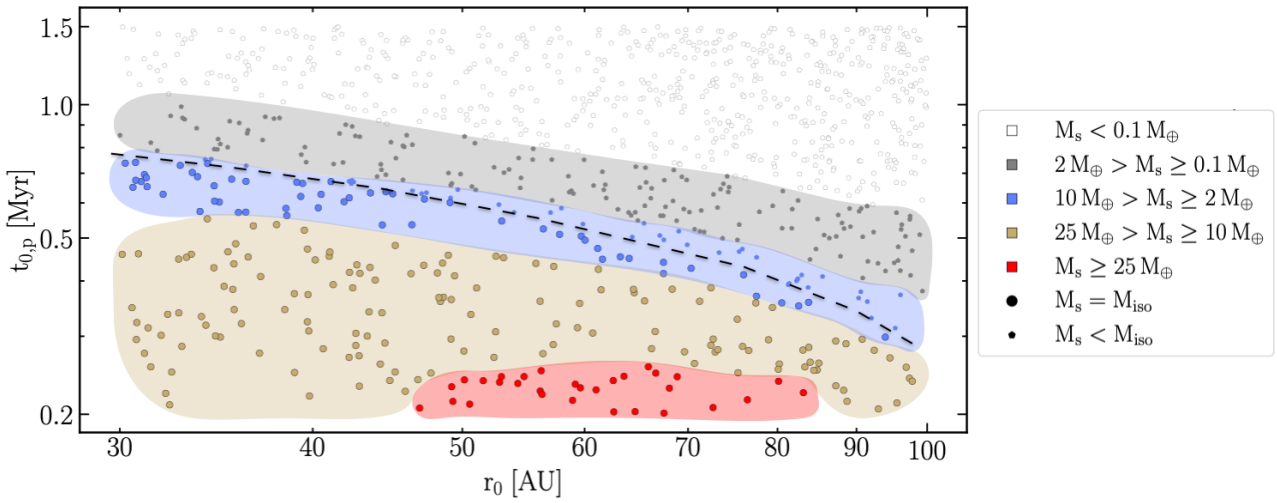

Figure 4.4: Total solid mass of protoplanets from fig. 4.3 depending on the initial position and formation time of the embryos. The coloured regions indicate the solid mass specified in the legend. Protoplanets that reach M_{iso} are denoted by circular symbols, while those that fail to reach M_{iso} are represented by small pentagonal symbols. The black line separates both populations. The most massive cores (and therefore the furthest ones) originate from early embryos ($t_{0,p} \lesssim 0.3\,$Myr) located within the range $\sim 50 - 80\,$AU.

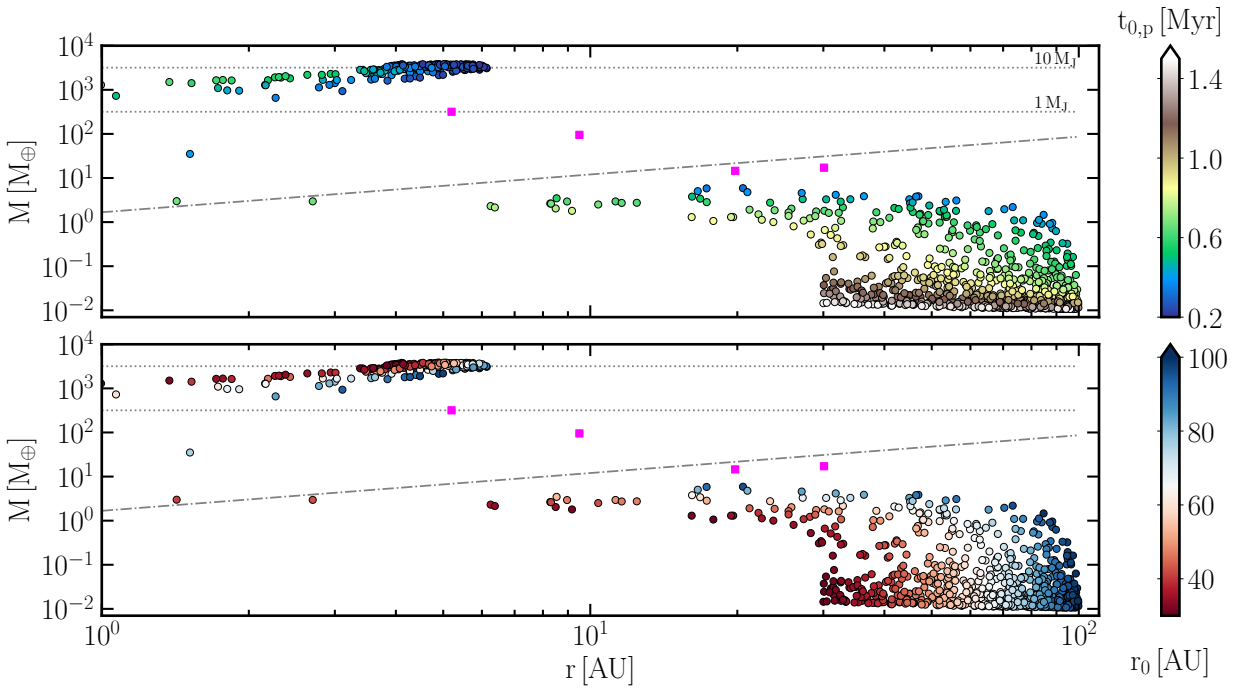

Figure 4.5: Same as fig. 4.3 but including gas accretion when the cores reach M_{iso}. As a reference, magenta squares show the position and mass of the giant planets in the Solar System, and the grey dotted lines indicate 1 and 10 times the mass of Jupiter. The furthest gas giants are at $\sim$ 6 AU and are as massive as $\sim$ 10 M_{Jup}. The embryos of those giant planets must form early and be initialised in the outer regions (see fig. 4.6 for a detailed description).

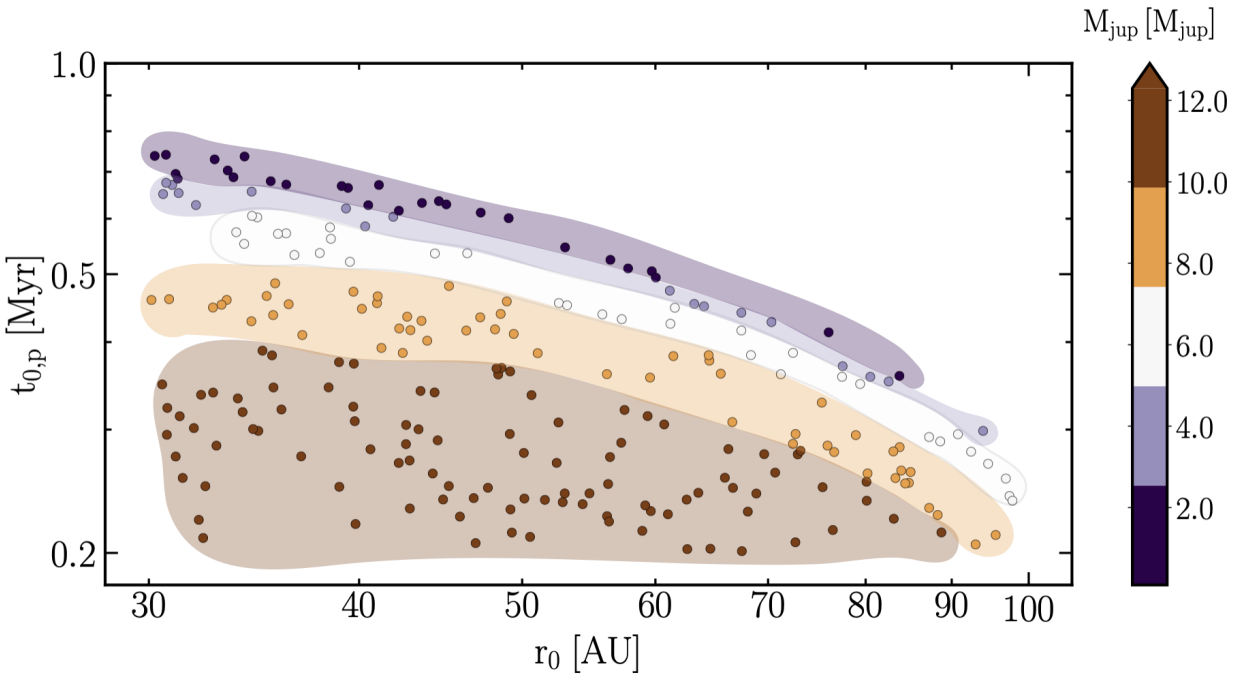

(a) The final mass of the gas giant is larger when the embryo forms closer to the star or/and when it forms earlier.

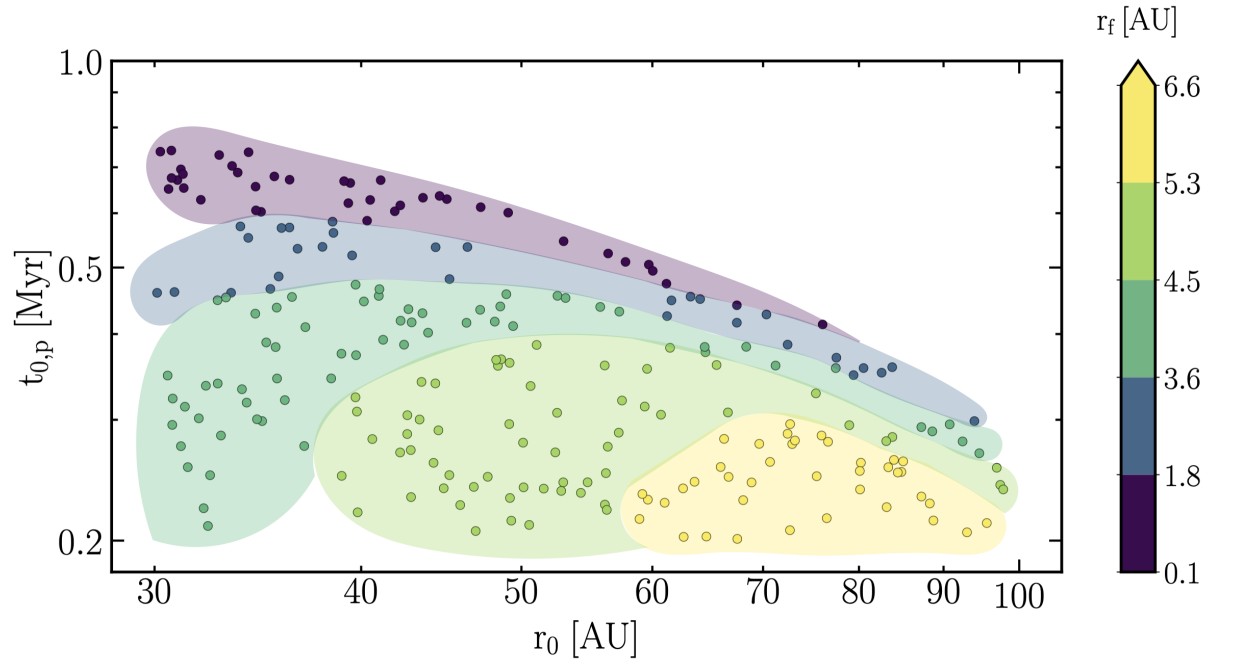

(b) For a given initial location, the later the embryo forms, the closer the final gas giant is. On the other hand, if the embryo forms early, the final gas giant is further away when the embryo forms further away. However, if the embryo forms late, the final gas giant is closer to the star when the embryo forms further away.

Figure 4.6: Final mass and position of the gas giants depending on the initial position and formation time of the embryos.

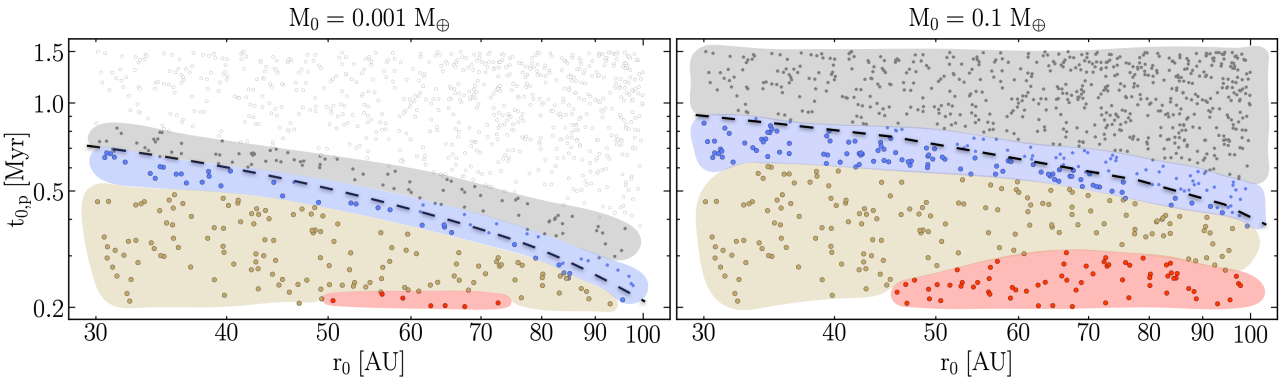

Figure 4.7: Same as fig. 4.4, but for $M_0 = 0.001\,\mathrm{M}_\oplus$ and $M_0 = 0.1\,\mathrm{M}_\oplus$. More massive embryos can form approximately $\sim 0.2\,\mathrm{Myr}$ later than small embryos to reach M_{iso}. An increase of ten times the initial mass produces an effect comparable to forming the embryo $\sim 0.1\,\mathrm{Myr}$ earlier.

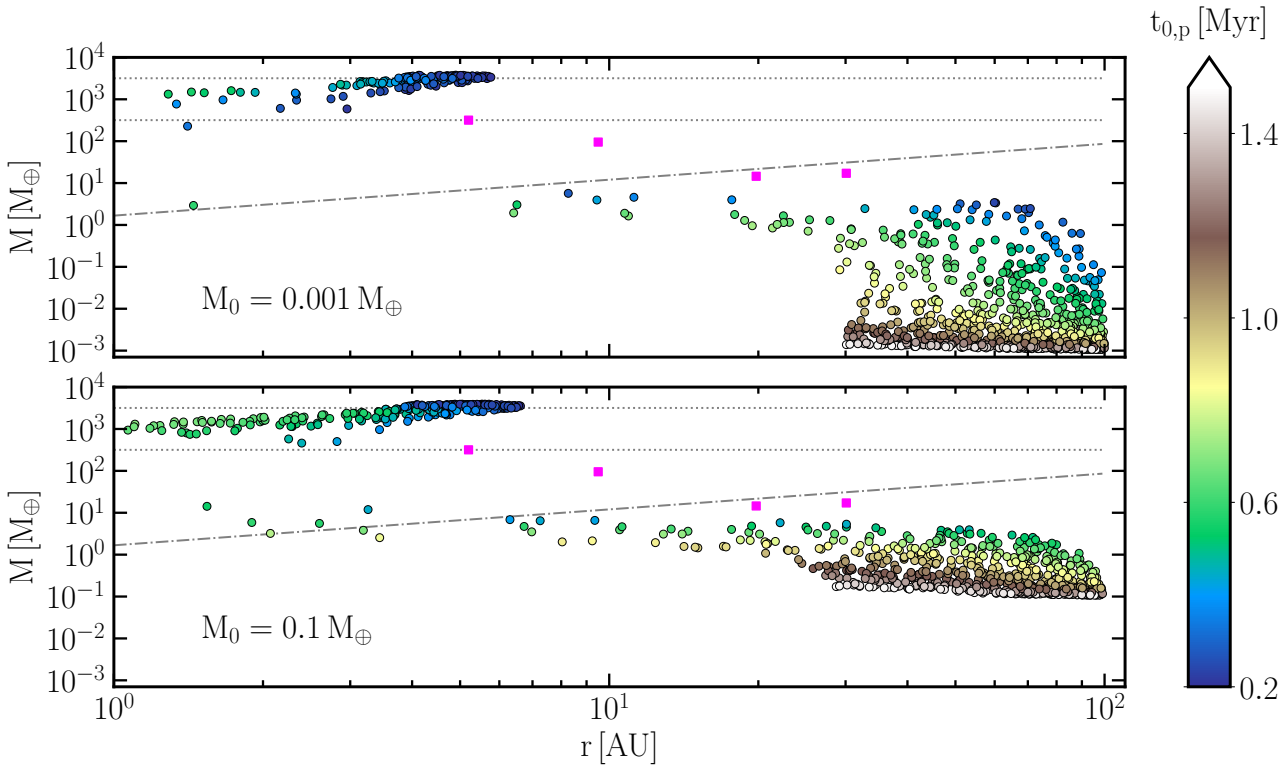

Figure 4.8: Same as fig. 4.5 but varying M_0. We can still form gas giants when $M_0 = 0.001\,\mathrm{M}_\oplus$. For high initial mass $M_0 = 0.1\,\mathrm{M}_\oplus$, the possibility for embryos to form gas giants expands longer in time, but there is no significant change in the furthest distance they reach; the furthest achievable final position is around $6 - 7\,\mathrm{AU}$, and they cross the pebble isolation mass at slightly further locations.

When increasing/decreasing the mass of the embryos an order of magnitude, the formation time required to reach M_{iso} spans/stretches $\sim 0.1\,\mathrm{Myr}$ at all locations (see fig. 4.7). Otherwise,

there is no significant change in the maximum distance of the cores and gas giants (see fig. 4.8).

4.2.2 Varying the Stokes number, initial metallicity and turbulence

Next, we ran simulations with the same set of initial conditions (r_0, $t_{0,\mathrm{p}}$) and $M_0 = 0.01\,\mathrm{M}_\oplus$, but varying the Stokes numbers St, the initial metallicity Z_0 and midplane turbulence α_t. For simplicity, we only changed the values of the parameters individually. We did not readjust the fiducial values as the conclusions would not change.

For St, we tried the values St = 0.01 and St = 0.06. St = 0.01 could be the real value if $\mathrm{St}_\mathrm{drift}$ from eq. 2.8 is overestimated or if $v_\mathrm{f} \sim 0.4\,\mathrm{m\,s^{-1}}$, which in that case means that the Stokes number is limited by fragmentation. On the other hand, St = 0.06 could be the real value if $\mathrm{St}_\mathrm{drift}$ from eq. 2.8 is underestimated, and $\mathrm{St}_\mathrm{frag} = 0.06$ with the fiducial $v_\mathrm{f} \sim 1\,\mathrm{m\,s^{-1}}$. In fig. 4.9, we show the results of varying St when $Z_0 = 0.01$. For small St = 0.01, the outcome strongly depends on the initial position. Embryos closer to the star at $r_0 \sim 30\,\mathrm{AU}$ mainly become gas giants, while protoplanets beyond $\sim 80\,\mathrm{AU}$ never reach M_iso. Growth is slower than for higher St, but as the flux depletes at later stages, the protoplanets can still reach M_iso at later times. When cores form late, the remaining amount of gas within the disk is lower, and therefore, the torque exerted by the gas causing migration is weaker. Thus, embryos initially between 50 and 70 AU and formed at early stages ($t_{0,\mathrm{p}} \lesssim 0.3\,\mathrm{Myr}$) reach M_iso later ($t \sim 1\,\mathrm{Myr}$) and at closer distances ($\lesssim 20\,\mathrm{AU}$, see also fig. 4.15 and fig. C.2), but far enough so that it leads to the formation of planets almost as far as 10 AU. Late-formed cores that never reach M_iso grow more than in the case of larger St due to the longer-lasting pebble flux. When increasing St, we see that the short-lasting pebble flux creates a large dichotomy between protoplanets that reach M_iso and the ones that do not.

For Z_0, we doubled the fiducial value ($Z_0 = 0.02$, $M_\mathrm{peb,0} \sim 1300\,\mathrm{M}_\oplus$), which can occur if, e.g. the star and the disk form in a higher-metallicity environment. In fig. 4.10, we see that a higher Z_0 leads to the formation of more distant gas giants. That occurs because the stronger pebble flux allows faster growth, and consequently, cores can form at larger distances. In fig. 4.11, we show the growth tracks of the furthest cores we can form. When St = 0.01, the cores can form at $\sim 35\,\mathrm{AU}$ at the furthest, and those cores form from embryos starting at around $\sim 90\,\mathrm{AU}$ at the earliest stages $t_{0,\mathrm{p}} \sim t_0$. In the case of St = 0.03, the cores form as far as 50 AU. Those cores form from embryos at $r_0 \gtrsim 80\,\mathrm{AU}$, and they reach M_iso at $t \gtrsim 0.4\,\mathrm{Myr}$. That means that when the disk is $t \sim 0.4\,\mathrm{Myr}$, it is possible to open a gap at 50 AU, and that this gap would co-migrate alongside the protoplanet. However, hydrodynamical simulations are necessary to study the details of the evolution of the gap (Kanagawa et al., 2020). When St = 0.06, the scenario is similar to St ~ 0.03, but the furthest cores form at $t \sim 0.3\,\mathrm{Myr}$. We already mentioned that faster growth is not always beneficial, as two protoplanets that reach M_iso at the same location but at different times, the late one will migrate less. Nonetheless, since the cores form way further, the increase of $Z_0 \sim 0.02$ is positive in forming wide-orbit gas giants at the end of the disk lifetime.

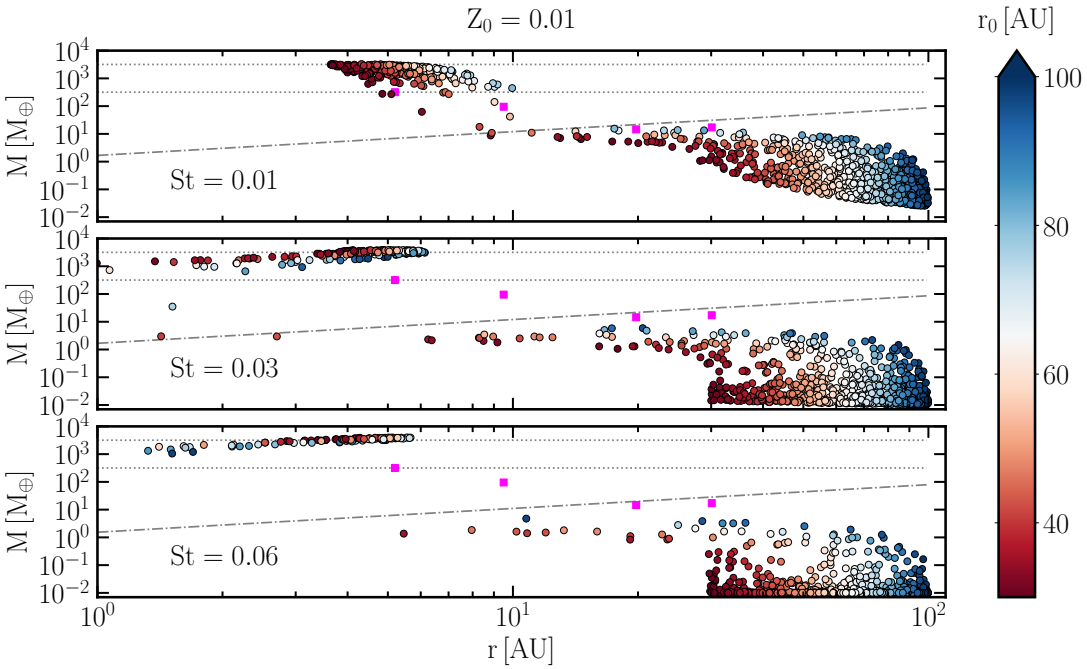

Figure 4.9: Same as fig. 4.5 but varying St. For small St = 0.01, early formed embryos initially between 60 and 80 AU lead to the formation of planets almost as far as 10 AU. For larger St = 0.03 and 0.06, there is a large dichotomy between protoplanets that reach $M_{\rm iso}$ and the ones that do not. In fig. C.1 we show the same plot but for $t_{0,\rm p}$ in the color-bar.

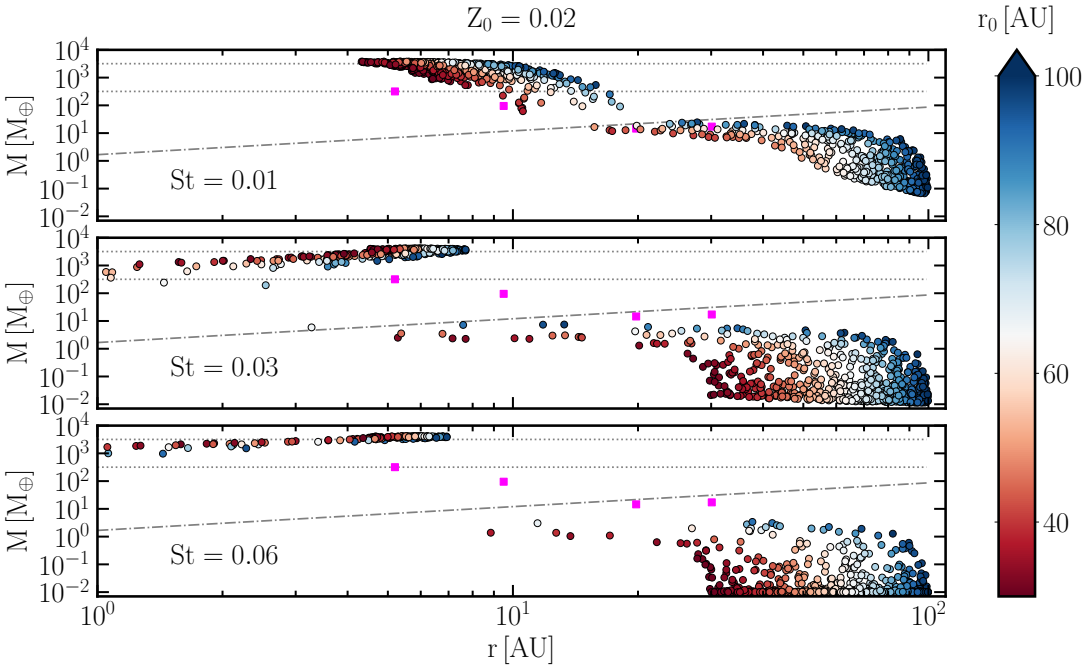

Figure 4.10: Same as fig. 4.9 but increasing Z_0. For any St, a higher Z_0 leads to the formation of more distant planets.

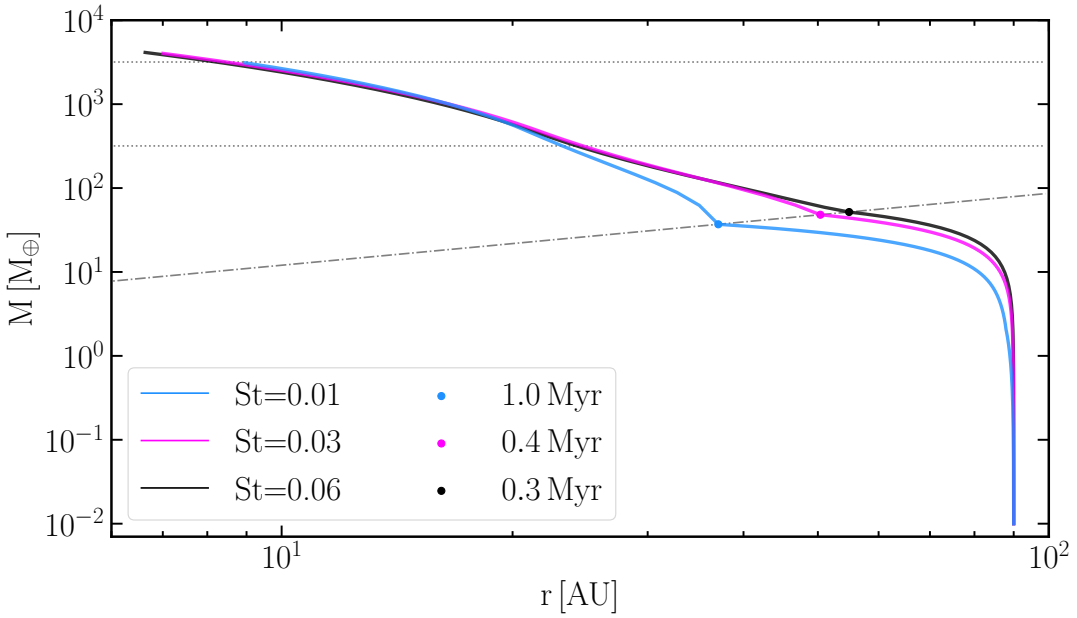

Figure 4.11: For $Z_0 \sim 0.02$ and varying St, the growth tracks of the furthest cores we can form. The embryos are initialised at $t_{0,\mathrm{p}} = t_0 = 0.2\,\mathrm{Myr}$ and located at $r_0 = 90\,\mathrm{AU}$. For $\mathrm{St} = 0.03$ and 0.06, the cores form at $\sim 50\,\mathrm{AU}$ when 0.4 and 0.3 Myr respectively. As they reach M_{iso} when the gas disk is massive, they undergo strong migration during gas accretion. When $\mathrm{St} = 0.01$ the core forms at $\sim 35\,\mathrm{AU}$ when $\sim 1\,\mathrm{Myr}$. As it reaches M_{iso} later, migration is weaker.

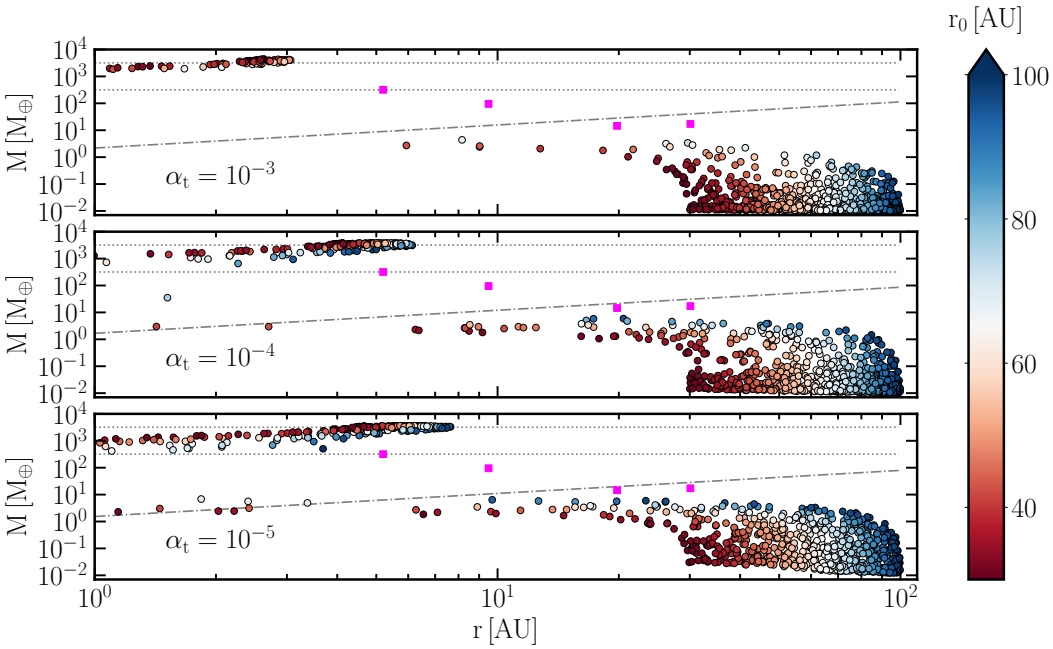

Figure 4.12: Same as fig. 4.9 but varying the midplane turbulence α_t. For lower turbulence, the furthest gas giants increase their distance by a few AU.

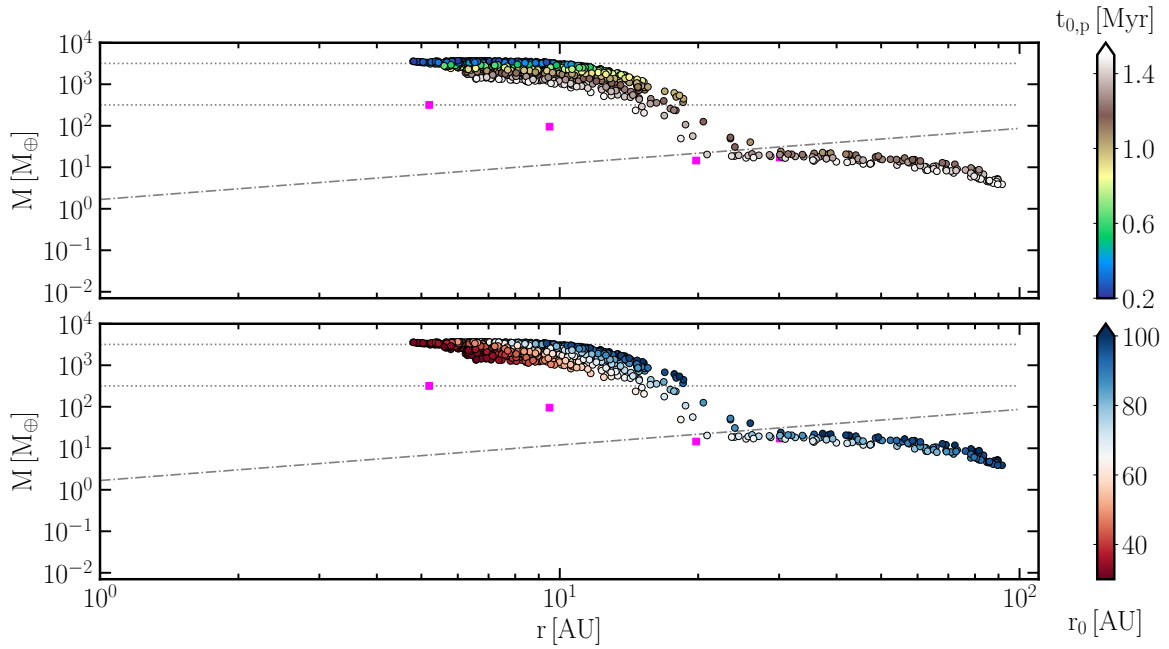

Figure 4.13: The evolution of protoplanets with the best scenario for forming wide-orbit planets at the end of the disk lifetime: St = 0.01, $Z_0 = 0.02$ and $\alpha_t \sim 10^{-5}$. These conditions can lead to gas giants as far as ~ 20 AU. We did not include the new path for gas accretion yet.

For α_t, we tried the scenario of high turbulence $\alpha_t \sim 10^{-3}$ and low turbulence $\alpha_t \sim 10^{-5}$. In fig. 4.12, we see that high turbulence hinders the formation of gas giants mainly in the outer regions, while low turbulence leads to the formation of wider orbit gas giants. As low midplane turbulence allows pebbles to settle down onto the midplane, the initial growth in the 3D regime becomes faster. Furthermore, high turbulence hinders the particle's growth and $St \sim St_{frag} \sim 0.005$ for fiducial values (see eq. 2.7). However, there is very little growth in such a scenario (see fig. C.3).

Overall, we saw that the best characteristics for the fast core formation are $Z_0 = 0.02$ and $\alpha_t \sim 10^{-5}$. We also saw that when St = 0.01, gas giants can form further at the end of the disk lifetime. Within that scenario, we can form gas giants between 10 and 20 AU (see fig. 4.13). Their embryos formed at around $t_{0,p} \sim 0.5-1.5$ Myr in the outermost regions within the disk $\sim 60-100$ AU (see fig. C.4 and C.5 for detailed description). The furthest cores that we can form within this scenario are at ~ 45 AU when ~ 0.7 Myr, and then, it would migrate towards ~ 10 AU by the end of the disk lifetime. In this scenario, we see that the protoplanets that do not reach M_{iso} are as massive as $\sim 10\,M_\oplus$ and orbit as far as 70 AU.

So far, we were able to reproduce the formation of gaps at far distances ($\lesssim 50$ AU) and the formation of relatively wide-orbit gas giants ($\lesssim 20$ AU) at the end of the disk lifetime. Attempting to inquire whether or not pebble accretion could explain the existence (albeit scarce) of gas giants beyond 20 AU, in the next section, we implement the new path for starting gas accretion.

4.2.3 A new gas accretion path for forming wide-orbit gas giants

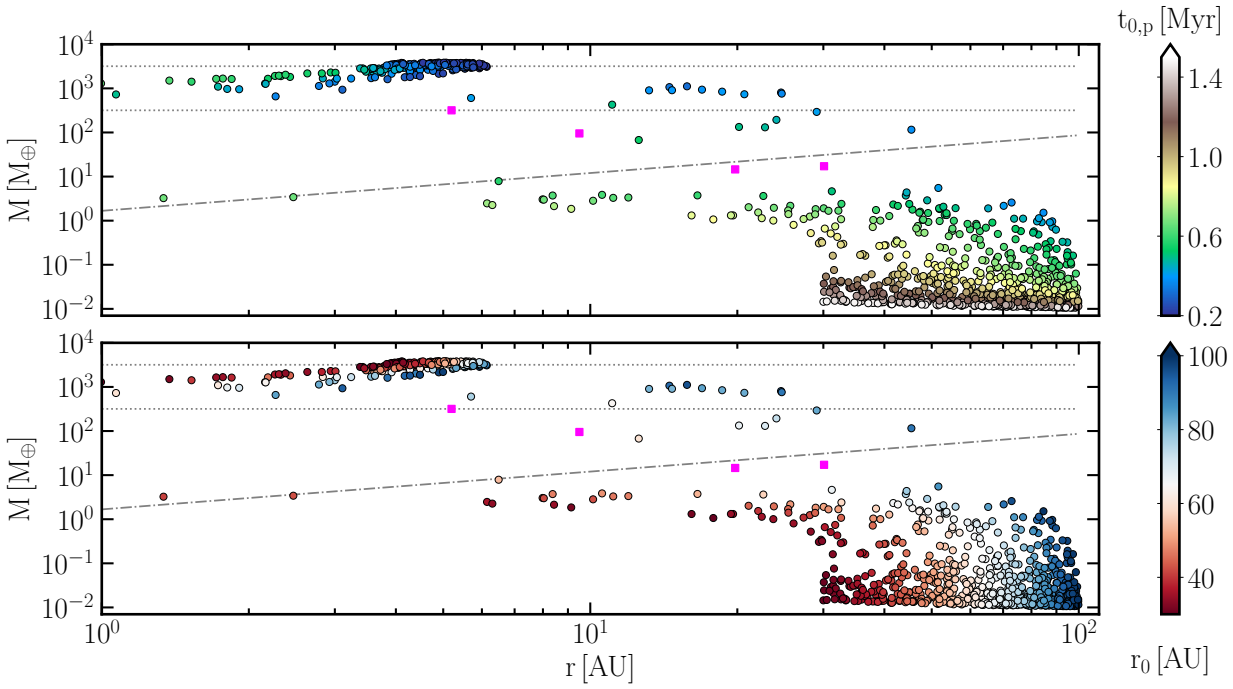

Figure 4.14: Evolution of 1000 protoplanets but including gas accretion before reaching $M_{\rm iso}$ when $\tau > 100\,{\rm Myr}$ (see eq. 3.75). It is possible to form gas giants beyond 10 AU for fiducial values.

In fig. 4.14, we repeated the simulations for fiducial values but including gas accretion before reaching $M_{\rm iso}$ if $\tau > 100\,{\rm Myr}$. Previously, the furthest giant planets we could form were at $\sim 6\,{\rm AU}$ for fiducial values (see fig. 4.5). With this new approach, we form a few giant planets between 10 and 30 AU. Furthermore, trying different scenarios, we saw that it is possible to form gas giants as far as 50 AU (see fig. C.6). These giant planets have cores between 2 and $8\,{\rm M}_\oplus$, and start growing from embryos formed between 0.4 and 0.7 Myr located between 60 AU and 100 AU. In fig. C.6, we included the calculations but varying the $\tau_{\rm th} = 10, 40, 70, 100\,{\rm Myr}$ due to atmospheric pollution variability (Lambrechts et al., 2014). For higher $\tau_{\rm th}$, protoplanets will take longer to cool down, and therefore, they will accrete gas later. Therefore, final masses will be lower for higher $\tau_{\rm th}$. In the same figure, we show different scenarios ($M_0 = 0.1\,{\rm M}_\oplus$, $Z_0 = 0.02$ and $\alpha_{\rm t} \sim 10^{-5}$), and in all of them we could reproduce wide-orbit gas giants. When St ~ 0.01, given that the pebble flux is long-lasting, this new mechanism does not apply.

Table 4.1: Summary of different sets of simulations. For each of them, we ran 1000 simulations with the same initial condition set $(r_0, t_{0,\mathrm{p}})$. The parameters we changed from the fiducial value are emphasised in bold type. For abbreviations, we used the prefix h (high) or xs/s/l (extra small/small/low) + the parameter we varied.

Set	**(A)**	**(B)**	**(C)**	**(D)**	**(E)**	**(F)**	**(G)**	**(H)**	**(I)**	**(J)**	**(K)**	**(L)**
$M_0\,[\mathrm{M}_\oplus]$	0.01	**0.001**	**0.1**	0.01	0.01	0.01	0.01	0.01	0.01	0.01	0.01	0.01
Z_0	0.01	0.01	0.01	0.01	0.01	**0.02**	**0.02**	**0.02**	0.01	0.01	0.01	**0.02**
St	0.03	0.03	0.03	**0.01**	**0.06**	**0.01**	0.03	**0.06**	**0.005**	0.03	0.03	**0.01**
α_t	10^{-4}	10^{-4}	10^{-4}	10^{-4}	10^{-4}	10^{-4}	10^{-4}	10^{-4}	$\mathbf{10^{-3}}$	$\mathbf{10^{-3}}$	$\mathbf{10^{-5}}$	$\mathbf{10^{-5}}$
Abv.	fid	sM$_0$	hM$_0$	sSt	hSt	sSt.hZ	hZ	hSt.hZ	xsSt.hα_t	hα_t	lα_t	sSt.hZ.lα_t

4.2.4 Comparison between different scenarios

In table 4.1, we summarise different scenarios we tried. In fig. 4.15, we show the obtained solid masses as well as the number of protoplanets that reach M_{iso}. In fig. 4.16, we show the final positions of the gas giants.

In fig. 4.15, we see that we can only form very metal-rich cores ($> 35\,\mathrm{M}_\oplus$) if $Z_0 = 0.02$. With fiducial values, we can form cores as massive as $25 - 35\,\mathrm{M}_\oplus$. A decrease in the turbulence ($\alpha_{\mathrm{t}} \sim 10^{-5}$) is beneficial for forming more massive cores, as the initial growth in the 3D regime is faster (see eq. 3.64) and M_{iso} increases with decreasing α_{t} (see eq. 3.74). In the scenario of only varying St $= 0.01$ is not possible to form metal-rich cores, but this is improved when including $Z_0 = 0.02$. In fig. 4.16, we see that the configuration of St $= 0.01$ and $Z_0 = 0.02$ is the only one in reproducing wide-orbit planets further away than 10 AU among planets that reach M_{iso}, and it is improved when the turbulence is $\alpha_{\mathrm{t}} \sim 10^{-5}$. However, when St $\gtrsim 0.03$, we could also reproduce a few wide-orbit gas giants that never reach M_{iso}.

4.3 Summary and Implications

In this work, we intended to decipher which scenarios lead to the rapid formation of distant planetary cores via pebble accretion, thereby enabling them to carve gaps as in observed disks. Additionally, we analysed the formation of distant giant planets at the end of the disk lifetime. Given that pebbles drift inwards, we derived a novel analytical model to describe the pebble flux that supplies material for the growth of embryos. In fig. 4.2, we showed that the new pebble flux model is necessary, especially in the outer regions. Starting from an embryo of $\sim 0.01\,\mathrm{M}_\oplus$, we implemented that the protoplanet can grow via pebble accretion within the 3D or 2D regime, as well as in the Bondi or Hill regime. As shown in fig. 3.6 and 4.1d, the initial embryo grows within the 3D Bondi regime in the outer regions. We also considered that the protoplanet migrates as it grows and that it opens a gap that

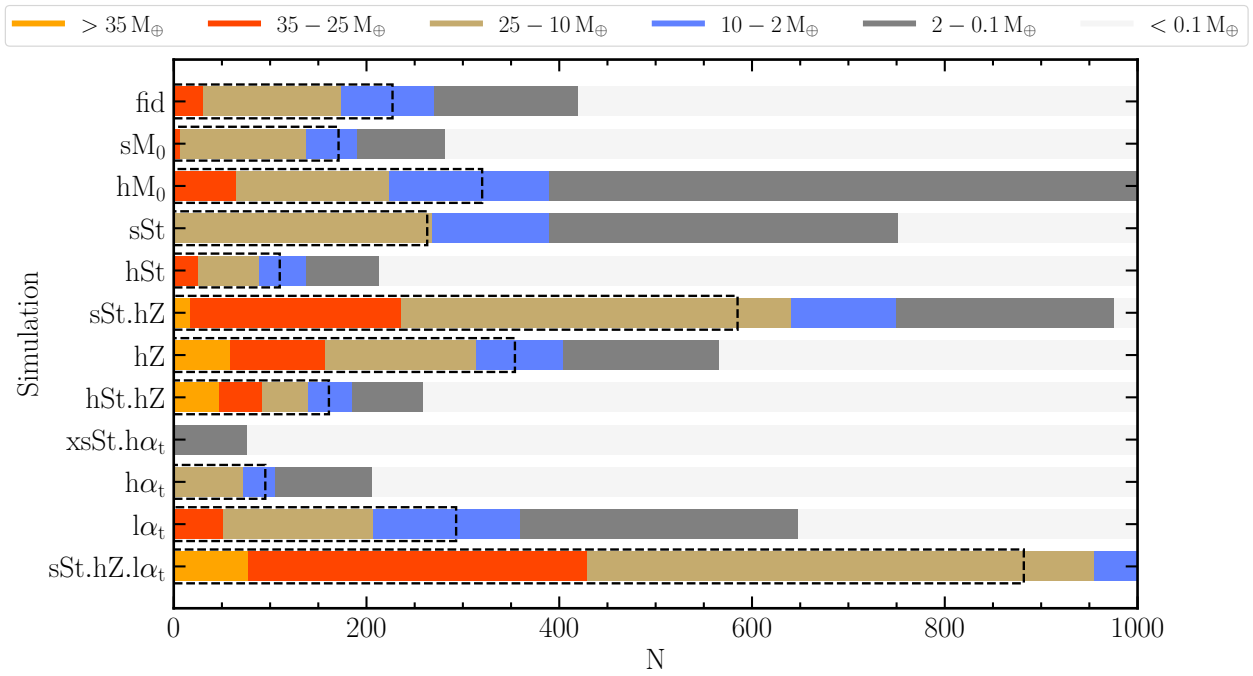

Figure 4.15: The amount of protoplanets in different total solid mass ranges for various scenarios (see table 4.1). The dashed lines indicate the number of protoplanets that reach $M_{\rm iso}$.

hinders pebble accretion and slows down migration. Once the core formed by reaching the pebble isolation mass $M_{\rm iso}$, we included a prescription of the gas accretion. Moreover, we proposed that the protoplanet can accrete gas before reaching $M_{\rm iso}$ when the pebble flux depletes significantly.

We found that the Stokes number of the pebble flux determines the core formation and, consequently, the final position of giant planets. A relatively strong pebble flux (St $\gtrsim 0.01$) is necessary for growth in the outer regions. Moreover, a short-lasting (St $\gtrsim 0.03$) flux can form metal-rich cores very quickly ($t \sim 0.35 - 0.7\,$Myr) at around 30 AU and open a gap. After accreting gas, these giant planets end up orbiting at 6 AU at the furthest. On the contrary, a long-lasting (St ~ 0.01) flux can form gas giants with lower core masses opening a gap at $\sim 20\,$AU when $\sim 1\,$Myr. However, the final giant planets will orbit as far as 10 AU. When including gas accretion when the pebble flux depletes, the short-lasting pebble flux can form gas giants between $\sim 10 - 30\,$AU with low core masses. These bodies will get massive enough to open a gap after they start accreting gas at $t > 2\,$Myr. Therefore, with a short-lasting flux protoplanets could open a gap at around 30 AU in both the early and late stages.

An increase in the metallicity of $Z_0 \sim 0.02$ significantly contributes to the formation of metal-richer cores. In fig. 4.11, we showed that cores can quickly form as far as $\sim 50\,$AU for St $\gtrsim 0.03$, and $\sim 35\,$AU for St $\gtrsim 0.01$. Moreover, in the case of the long-lasting pebble flux, giant planets can form as far as 20 AU at the end of the disk lifetime (see fig. 4.10).

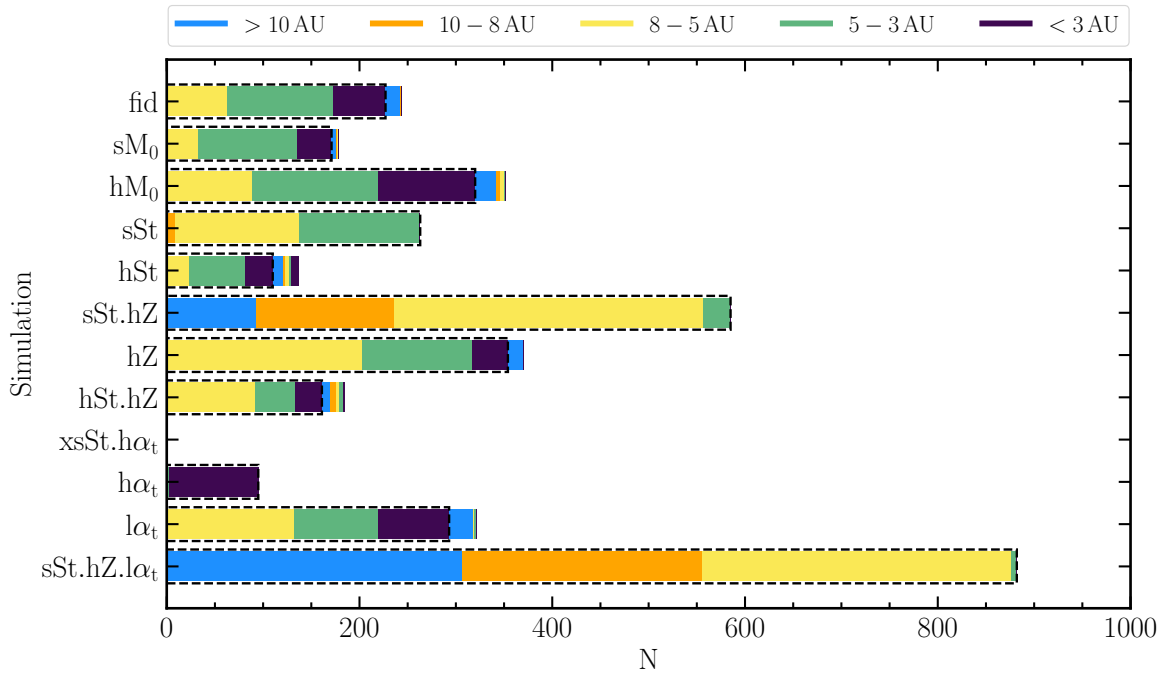

Figure 4.16: The amount of gas giants within different final position ranges for various scenarios (see table 4.1). The dashed lines indicate the number of protoplanets that reach $M_{\rm iso}$. The planets outside the dashed region undergo gas accretion without reaching $M_{\rm iso}$.

Furthermore, we found that high turbulence hinders the formation of wide-orbit planets, and low turbulence allows the outermost embryos to grow faster. Hence, a relatively high metallicity of $Z_0 \sim 0.02$ and low turbulence of $\alpha_{\rm t} \sim 10^{-5}$ are beneficial in forming wide-orbit gas giants with metal-rich cores.

Aside from the characteristics of the disk, the initial location and formation time of the embryo are crucial for the outcome. Embryos initially located at $> 60\,$AU and formed earlier than $\sim 1\,$Myr are necessary to form wide-orbit giant planets (the ranges could be narrower or wider depending on the scenario, see section 4.2.2). An increase (decrease) of ten times the initial mass of the embryo produces an effect comparable to forming the embryo $\sim 0.1\,$Myr earlier (later) (see fig. 4.7). The embryo has to form at early stages to reach $M_{\rm iso}$ in the outer regions. However, according to Liu et al. (2020), the embryos are more massive further from the star; an embryo at $\sim 100\,$AU can be one order of magnitude larger than an embryo at $\sim 10\,$AU. If the embryos are more massive in the outer regions, the position dependency in reaching $M_{\rm iso}$ could be mitigated. Otherwise, we did not find a strong correlation between the formation of more massive embryos and an increase in the furthest distances that gas giants can achieve. The authors in Jiang & Ormel (2023) analysed the formation of wide-orbit planets using ring substructures, and their findings led to a similar conclusion.

In section 4.2.3, we proposed a mechanism that could potentially elucidate the formation of gas giants at significantly greater distances. We found that the model results in two

types of gas giants; the ones that reach $M_{\rm iso}$ and therefore have a metal-rich core, and the ones that orbit at further distances and have a smaller core (between 2 and 8 $M_\oplus$). Moreover, these distant planets are overall less massive than the ones that reach $M_{\rm iso}$ (but final mass moderately depends on $\tau_{\rm th}$, see fig. C.6). We suggest that in observations we could differ if a protoplanet at $\sim$ 15 AU is formed by a long-lasting flux of St $\sim$ 0.01 or by a stronger short-lasting flux of St $\sim$ 0.03 by analysing its metallicity, as the latter would have a less massive core. Nonetheless, detecting the metallicity of a protoplanet could be challenging. Another possibility that we suggest is that in the short-lasting pebble scenario, the protoplanet would open a gap when the outer regions are mostly depleted of pebbles, while in the long-lasting pebble scenario, the solid amount would be higher. When observing a protoplanet within a gap, we propose that it might be possible to infer the scenario in which it was formed by detecting the solid amount in its outer regions.

One of the reasons why it has been questioned whether the substructures are formed by planets is because the substructures are observed in outer regions, whereas in evolved planetary systems, wide-orbit gas giants are hardly ever found (e.g. Vigan et al., 2017). Nevertheless, in every scenario we analysed, once the cores formed in the outer regions, they migrated tens of AUs until the disk dissipated. That could explain why we see several substructures in the outer regions that do not match the exoplanet catalogue. In addition, according to our model, wide-orbit planets are also rare (see fig. 4.14), as the protoplanet must attain sufficient growth through pebble accretion to be able to accrete gas while avoiding excessive migration and aligning with the decrease in pebble flux. This rare occurrence is consistent with the low frequency of wide-orbit giant planets from direct imaging surveys (Bowler & Nielsen, 2018).

Given that most of the simulated cores accrete solid material from the outer regions, that might imply that our giant planets may have started to form in the outer regions (previously suggested in Bitsch et al., 2019). This conclusion is in line with Jupiter's super-solar nitrogen abundance, as the majority of the nitrogen is frozen out in the outer regions exterior to the N_2 snowline beyond 30 AU (Öberg & Wordsworth, 2019). In addition, the metal content of Jupiter is between 25 $M_\oplus$ and 45 $M_\oplus$ (Wahl et al., 2017). It has been challenging to explain the formation of such massive cores only by pebble accretion mechanism; e.g., in Johansen et al. (2019), they alluded to late planetesimal accretion proposed by Shiraishi & Ida (2008). However, we could reproduce Jupiter's core analogues solely by pebble accretion within certain scenarios (see fig. 4.15). As we did not consider the interaction between planets, we cannot draw any accurate conclusions about the formation of the Solar System. Nevertheless, it is noteworthy that in figures 4.9 and 4.10 when St = 0.01, we were able to reproduce all the giant planets of the Solar System with unexpected accuracy. While we do not have enough data to posit that the Solar System must have formed within such a scenario, we can conclude that the formation of planets with the mass and location of the giant planets in the Solar System are reproducible individually in the same scenario.

Chapter 5

Main Limitations and Prospects

In this work, we analysed whether distant planets can form via pebble accretion. Our models have certain limitations, and some of them may impact our results.

First, the derived pebble flux model does not include dust evolution; we estimated the growth of the outermost solids and calculated when they start drifting. We also assumed a constant St for the flux across the disk. Nevertheless, dust coagulation might result in a distribution of particles with different St and Z across the disk. In fig. 5.1, we conducted a preliminary comparative analysis between our analytical pebble flux models (from eq. 3.53 and 3.57) and the numerical one calculated in Appelgren et al. (2023), where they included a simple model of dust evolution with both fragmentation and drifting barriers. In this comparison, the analytical models look promising. Nevertheless, the flux from the assumption that St and χ are constant (left panel) is closer to the numerical flux than the one that assumes only St constant (center panel). That might be because in the outer regions, the radial drift limits the growth of particles, and $\mathrm{St}_{\mathrm{drift}} \cdot \chi \propto \mathrm{r}^{-\frac{4}{7}}$ (see eq. B.1), which is a weak r-dependency in the outermost regions. As in the PDE St and χ are multiplying (see eq. 3.25 and 3.32), the assumption of considering both constants might be a better approximation. We made our simulations by assuming that only St is constant, and we do not expect that switching the analytical pebble flux model would have a major effect (see fig. 4.2). Nevertheless, the impact of our approximations needs to be studied in the future by comparing it with detailed dust evolution models (e.g. Birnstiel et al., 2010).

In our simulations, our starting point is an embryo of $\sim 0.01\,\mathrm{M}_{\oplus}$ initialised in a smooth disk at any position and time within the disk. So far, we did not discuss the origin of the embryos since our goal was to study the growth once pebble accretion takes place. For triggering SI, a local enrichment in the metallicity of $Z \sim 0.015$ and a large Stokes number of $\mathrm{St} \sim 0.1$ are required (Johansen et al., 2009; Bai & Stone, 2010). The water ice line (where the inward drifting pebbles evaporate) is demonstrated to be a preferred location for fulfilling these criteria (e.g. Schoonenberg et al., 2018). If the ice lines of more volatile species (e.g. N_2, CO) are also favourable locations for forming planetesimals, this could explain the origin of distant embryos (Qi et al., 2013). Next, we modelled the evolution of the protoplanet utilising scaling laws derived from previous works (e.g. for migration and pebble isolation mass Tanaka et al., 2002; Kanagawa et al., 2018; Bitsch

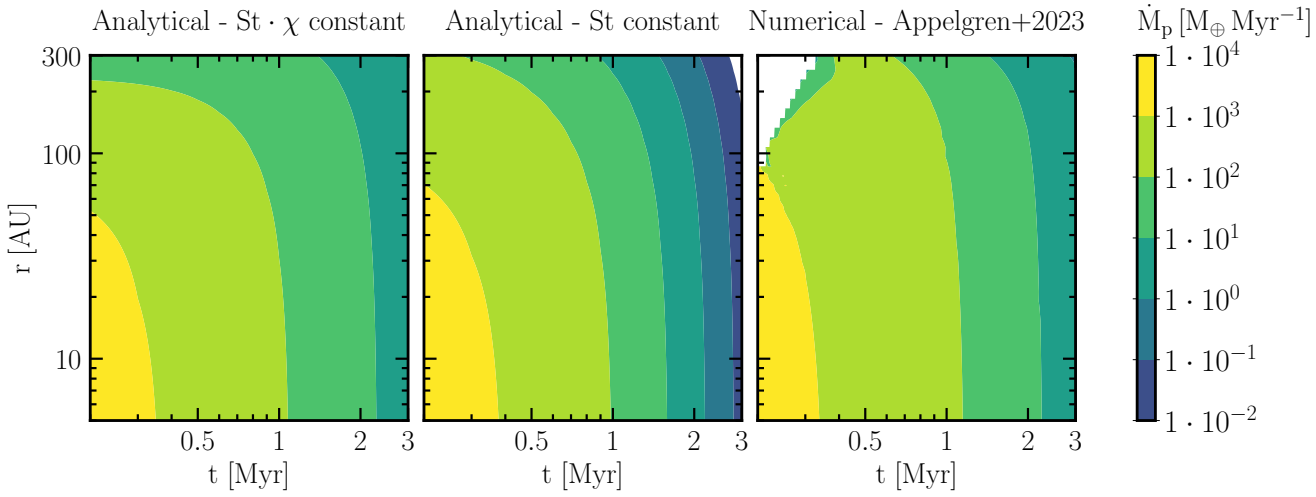

Figure 5.1: Comparison of the analytical pebble fluxes (eq. 3.53 and 3.57) and numerical calculations from Appelgren et al. (2023). Both analytical models display adequate output, but the one that assumes constant St and χ exhibits closer proximity to numerical calculations. We thank Johan Appelgren for sharing the data needed to produce the figure.

et al., 2018). The use of these simplified scaling laws might undermine our accuracy. Regarding the formation of the core, we did not include planetesimal accretion, which might increase the growth rate of the core. Moreover, in Birnstiel et al. (2012), they demonstrated that dust coagulation leads to a two-size population; large pebbles and small dust. We neglected the contribution of the smallest population. Nonetheless, in Lyra et al. (2023), they claimed that the contribution of small solids to the growth rate (especially in the Bondi regime) is significant. Because of this, our growth rate might be underestimated.

Our goal was to model the growth via pebble accretion. Nevertheless, we included a simplified gas accretion model for some insights into the formation of gas giants. As we see in e.g. fig. 4.5, the gas giants attain masses often higher than most observed exoplanets. Our model does not explain how to stop gas accretion unless we reduce the disk lifetime. Hence, a more detailed model for gas accretion is necessary to study more realistic outcomes. Another limitation is that the gas accretion depends on the opacity κ, which its value, to date, is still unknown. Moreover, we proposed that when the pebble flux depletes significantly, the envelope could cool down, and the protoplanet could accrete gas if it is massive enough. This mechanism needs to be further studied in the future since we did not relate the cooling time with the opacity of the envelope.

We simulated the evolution of isolated protoplanets, yet many planets reside in multi-planetary systems. Simultaneously growing bodies would interact with each other, strongly influencing the outcome (Bitsch et al., 2019). However, the study of a multi-planetary system cannot (or should not) be carried out without first studying the formation of individual planets. Due to the scant research on planet formation in outer regions, we studied single-evolving protoplanets.

Finally, the results are very sensitive to variations in the parameters. We often used fiducial values based on previous literature, but in many cases, the values are still being debated, and future observations are needed for further constraint. In addition, to compare our results with forthcoming observations of young wide-orbit planets (see fig. 1.1), the generalisation of the model for all types of stars is necessary.

Bibliography

Appelgren J., Lambrechts M., van der Marel N., 2023, arXiv e-prints, p. arXiv:2303.07297

Armitage P. J., 2010, Astrophysics of Planet Formation. Cambridge University Press

Bae J., Isella A., Zhu Z., Martin R., Okuzumi S., Suriano S., 2022, arXiv e-prints, p. arXiv:2210.13314

Bai X.-N., Stone J. M., 2010, ApJ, 722, 1437

Birnstiel T., Dullemond C. P., Brauer F., 2009, Astronomy & Astrophysics, 503, L5

Birnstiel T., Dullemond C. P., Brauer F., 2010, Astronomy & Astrophysics, 513, A79

Birnstiel T., Klahr H., Ercolano B., 2012, Astronomy & Astrophysics, 539, A148

Bitsch B., Johansen A., Lambrechts M., Morbidelli A., 2015a, Astronomy & Astrophysics, 575, A28

Bitsch B., Lambrechts M., Johansen A., 2015b, Astronomy & Astrophysics, 582, A112

Bitsch B., Morbidelli A., Johansen A., Lega E., Lambrechts M., Crida A., 2018, Astronomy & Astrophysics, 612, A30

Bitsch B., Izidoro A., Johansen A., Raymond S. N., Morbidelli A., Lambrechts M., Jacobson S. A., 2019, Astronomy & Astrophysics, 623, A88

Blum J., Wurm G., 2008, Annual Review of Astronomy and Astrophysics, 46, 21

Boss A. P., 1997, Science, 276, 1836

Bowler B. P., Nielsen E. L., 2018, in Deeg H. J., Belmonte J. A., eds, , Handbook of Exoplanets. p. 155, doi:10.1007/978-3-319-55333-7_155

Brauer F., Dullemond C. P., Henning T., 2008, Astronomy & Astrophysics, 480, 859

Chambers J., 2021, ApJ, 914, 102

Coleman G. A. L., Nelson R. P., 2014, Monthly Notices of the Royal Astronomical Society, 445, 479

Currie T., et al., 2022, Nature Astronomy, 6, 751

D'Angelo G., Lubow S. H., 2010, ApJ, 724, 730

Drążkowska J., Stammler S. M., Birnstiel T., 2021, Astronomy & Astrophysics, 647, A15

Drążkowska J., et al., 2022, arXiv e-prints, p. arXiv:2203.09759

Dubrulle B., Morfill G., Sterzik M., 1995, Icarus, 114, 237

Dürmann C., Kley W., 2015, Astronomy & Astrophysics, 574, A52

Feng Y., Krumholz M. R., 2014, Nature, 513, 523

Garaud P., Lin D. N. C., 2007, ApJ, 654, 606

Goldreich P., Tremaine S., 1978, ApJ, 222, 850

Güttler C., Blum J., Zsom A., Ormel C. W., Dullemond C. P., 2010, Astronomy & Astrophysics, 513, A56

Haffert S. Y., Bohn A. J., de Boer J., Snellen I. A. G., Brinchmann J., Girard J. H., Keller C. U., Bacon R., 2019, Nature Astronomy, 3, 749

Haisch Karl E. J., Lada E. A., Lada C. J., 2001, The Astrophysical Journal Letters, 553, L153

Hartmann L., Calvet N., Gullbring E., D'Alessio P., 1998, ApJ, 495, 385

Hartmann L., Herczeg G., Calvet N., 2016, Annual Review of Astronomy and Astrophysics, 54, 135

Ida S., Lin D. N. C., 2004, ApJ, 604, 388

Ida S., Guillot T., Morbidelli A., 2016, Astronomy & Astrophysics, 591, A72

Ida S., Tanaka H., Johansen A., Kanagawa K. D., Tanigawa T., 2018, ApJ, 864, 77

Ikoma M., Nakazawa K., Emori H., 2000, ApJ, 537, 1013

Jiang H., Ormel C. W., 2023, Monthly Notices of the Royal Astronomical Society, 518, 3877

Johansen A., Bitsch B., 2019, Astronomy & Astrophysics, 631, A70

Johansen A., Lambrechts M., 2017, Annual Review of Earth and Planetary Sciences, 45, 359

Johansen A., Youdin A., Mac Low M.-M., 2009, The Astrophysical Journal Letters, 704, L75

Johansen A., Blum J., Tanaka H., Ormel C., Bizzarro M., Rickman H., 2014, in Beuther H., Klessen R. S., Dullemond C. P., Henning T., eds, Protostars and Planets VI. p. 547 (arXiv:1402.1344), doi:10.2458/azu_uapress_9780816531240-ch024

Johansen A., Ida S., Brasser R., 2019, Astronomy & Astrophysics, 622, A202

Kanagawa K. D., Tanaka H., Szuszkiewicz E., 2018, ApJ, 861, 140

Kanagawa K. D., Nomura H., Tsukagoshi T., Muto T., Kawabe R., 2020, ApJ, 892, 83

Keppler M., et al., 2018, Astronomy & Astrophysics, 617, A44

Kley W., Nelson R. P., 2012, Annual Review of Astronomy and Astrophysics, 50, 211

Lambrechts M., Johansen A., 2012, Astronomy & Astrophysics, 544, A32

Lambrechts M., Johansen A., 2014, Astronomy & Astrophysics, 572, A107

Lambrechts M., Johansen A., Morbidelli A., 2014, Astronomy & Astrophysics, 572, A35

Lambrechts M., Morbidelli A., Jacobson S. A., Johansen A., Bitsch B., Izidoro A., Raymond S. N., 2019, Astronomy & Astrophysics, 627, A83

Lin D. N. C., Papaloizou J., 1986, ApJ, 309, 846

Liu B., Lambrechts M., Johansen A., Pascucci I., Henning T., 2020, Astronomy & Astrophysics, 638, A88

Lorek S., Johansen A., 2022, Astronomy & Astrophysics, 666, A108

Lubow S. H., D'Angelo G., 2006, ApJ, 641, 526

Lynden-Bell D., Pringle J. E., 1974, Monthly Notices of the Royal Astronomical Society, 168, 603

Lyra W., Johansen A., Cañas M. H., Yang C.-C., 2023, arXiv e-prints, p. arXiv:2301.03825

Manara C. F., Robberto M., Da Rio N., Lodato G., Hillenbrand L. A., Stassun K. G., Soderblom D. R., 2012, ApJ, 755, 154

Miotello A., Kamp I., Birnstiel T., Cleeves L. I., Kataoka A., 2022, arXiv e-prints, p. arXiv:2203.09818

Misener W., Krijt S., Ciesla F. J., 2019, ApJ, 885, 118

Morbidelli A., 2020, Astronomy & Astrophysics, 638, A1

Öberg K. I., Wordsworth R., 2019, The Astronomical Journal, 158, 194

Ormel C. W., 2017, The Emerging Paradigm of Pebble Accretion. Springer International Publishing, Cham, pp 197–228, doi:10.1007/978-3-319-60609-5_7, https://doi.org/10.1007/978-3-319-60609-5_7

Ormel C. W., Cuzzi J. N., 2007, Astronomy & Astrophysics, 466, 413

Ormel C. W., Klahr H. H., 2010, Astronomy & Astrophysics, 520, A43

Pinte C., Teague R., Flaherty K., Hall C., Facchini S., Casassus S., 2022, arXiv e-prints, p. arXiv:2203.09528

Pollack J. B., Hubickyj O., Bodenheimer P., Lissauer J. J., Podolak M., Greenzweig Y., 1996, Icarus, 124, 62

Pringle J. E., 1981, Annual Review of Astronomy and Astrophysics, 19, 137

Qi C., et al., 2013, Science, 341, 630

Ricci L., Testi L., Natta A., Neri R., Cabrit S., Herczeg G. J., 2010, Astronomy & Astrophysics, 512, A15

Riley K. F., Hobson M. P., Bence S. J., 1999, Mathematical methods for physics and engineering

Safronov V. S., 1972, Evolution of the protoplanetary cloud and formation of the earth and planets.

Schäfer U., Yang C.-C., Johansen A., 2017, Astronomy & Astrophysics, 597, A69

Schoonenberg D., Ormel C. W., Krijt S., 2018, Astronomy & Astrophysics, 620, A134

Shakura N. I., Sunyaev R. A., 1973, Astronomy & Astrophysics, 24, 337

Sheehan P. D., Eisner J. A., 2018, ApJ, 857, 18

Shiraishi M., Ida S., 2008, ApJ, 684, 1416

Soderblom D. R., Hillenbrand L. A., Jeffries R. D., Mamajek E. E., Naylor T., 2014, in Beuther H., Klessen R. S., Dullemond C. P., Henning T., eds, Protostars and Planets VI. p. 219 (arXiv:1311.7024), doi:10.2458/azu_uapress_9780816531240-ch010

Tanaka H., Takeuchi T., Ward W. R., 2002, ApJ, 565, 1257

Tanigawa T., Tanaka H., 2016, ApJ, 823, 48

Testi L., et al., 2014, in Beuther H., Klessen R. S., Dullemond C. P., Henning T., eds, Protostars and Planets VI. p. 339 (arXiv:1402.1354), doi:10.2458/azu_uapress_9780816531240-ch015

Vigan A., et al., 2017, Astronomy & Astrophysics, 603, A3

Wahl S. M., et al., 2017, Geophysical Research Letters, 44, 4649

Weidenschilling S. J., 1977, Monthly Notices of the Royal Astronomical Society, 180, 57

Wetherill G. W., Stewart G. R., 1989, Icarus, 77, 330

Williams J. P., Cieza L. A., 2011, Annual Review of Astronomy and Astrophysics, 49, 67

Youdin A. N., Lithwick Y., 2007, Icarus, 192, 588

Appendices

A Fiducial values of parameters

Table 1: Definition of parameters used in this work, their fiducial values from literature and related equations.

Symbol	Definition	Fiducial Values	Equation
t_0	Initial time of the disk	0.2 Myr	—
t_f	Disk lifetime	3 Myr	—
M_*	Star mass	$1\,M_\odot$	—
M_{disk}	Initial disk mass	$0.16\,M_\odot$	eq. 3.16
$M_{peb,0}$	Initial pebble reservoir	$650\,M_\oplus$	—
Z	Global metallicity	Initially 0.01	eq. 3.53 and 3.57
Σ_g	Gas surface density	Initially $2000\,g\,cm^{-2}$ at 1 AU	eq. 3.9
Σ_p	Pebble surface density	Initially $20\,g\,cm^{-2}$ at 1 AU	eq. 3.21
R_1	Disk size	100 AU	—
$\dot{\mathcal{M}}_{g,0}$	Inner gas accretion rate	$10^{-7}\,M_\odot\,yr^{-1}$	eq. 3.14
c_s	Sound speed	$650\,m\,s^{-1}$ at 1 AU	eq. 3.4
ν	Viscosity	—	eq. 3.6
γ	Viscosity power-index	$\frac{15}{14}$	eq. 3.2
ζ	Temperature power-index	$\frac{3}{7}$	eq. 3.3
α	Accretion coefficient	0.01	—
α_t	Midplane turbulence	10^{-4}	—
Ω	Keplerian angular frequency	$2\pi\,yr^{-1}$ at 1 AU	eq. 2.1
H	Gas scale height	—	eq. 2.2
H_p	Pebble scale height	0.1 H	eq. 2.5
St	Stokes number	0.03	See eq. 2.3
v_f	Fragmentation velocity	$1\,m\,s^{-1}$	—
t_{stop}	Stopping time of pebbles	—	See eq. 2.3
ρ_{dust}	Internal density of pebbles	$1\,g\,cm^{-3}$	See eq. 2.4
a_s	Size of pebbles	Initially 2 mm at 100 AU	See eq. 2.4
κ	Opacity of the envelope	$0.005\ m^2\ kg^{-1}$	—
M_0	Initial mass of the embryo	$0.01 M_\oplus$	—
r_0	Initial position of the embryo	30−100 AU	—
$t_{0,p}$	Formation time of the embryo	$0.2 - 1.5$ Myr	—

B Analytical model for the pebble flux

In this appendix, we include the issues we found for the derivation of an analytical model when St is non-constant and another derivation for the metallicity, which turns out to be the same expression as in eq. 3.57.

B.1 An attempt to solve the pebble flux for non-constant St.

In this section, we explain why we could not solve the PDE for non-constant St. First, to date, there is no analytical expression of $\mathrm{St}(\mathrm{r},\mathrm{t})$ for describing the growth and transport simultaneously. We could, however, use the expression $\mathrm{St}(\mathrm{r}) \approx \mathrm{St}_{\mathrm{drift}}$ for outer regions and assume that particles reach $\mathrm{St}_{\mathrm{drift}}$ at approximately the same time in all locations. We can rewrite eq. 2.8 by substituting eq. 2.1 and 3.19,

$$\mathrm{St}_{\mathrm{drift}} \approx \frac{\sqrt{3\pi}}{80}\frac{v_{\mathrm{K}}}{\Delta v}Z_0 = 0.12\cdot\frac{100^{\frac{15}{14}-\gamma}}{\chi}\cdot\left(\frac{M_*}{M_\odot}\right)\cdot\left(\frac{c_{\mathrm{s1}}}{650\,\mathrm{m\,s^{-1}}}\right)^{-2}\cdot\left(\frac{Z_0}{0.01}\right)\cdot\left(\frac{r}{100\,\mathrm{AU}}\right)^{\frac{1}{2}-\gamma}. \quad \text{(B.1)}$$

Therefore, b from eq. 3.25,

$$b = \frac{2}{3}\frac{\chi}{\alpha}\mathrm{St}_{\mathrm{drift}} \approx 8\cdot 100^{\frac{15}{14}-\gamma}\cdot\left(\frac{\alpha}{0.01}\right)^{-1}\cdot\left(\frac{M_*}{M_\odot}\right)\cdot\left(\frac{c_{\mathrm{s1}}}{650\,\mathrm{m\,s^{-1}}}\right)^{-2}\cdot\left(\frac{Z_0}{0.01}\right)\cdot\left(\frac{r}{100\,\mathrm{AU}}\right)^{\frac{1}{2}-\gamma}. \quad \text{(B.2)}$$

For $\gamma = 1$, we can rewrite b and its dimensionless spatial derivative,

$$b = b_{\mathrm{s}}\tilde{r}^{-\frac{1}{2}}, \qquad \frac{\partial b}{\partial \tilde{r}} = -\frac{b_{\mathrm{s}}}{2}\tilde{r}^{-\frac{3}{2}}. \quad \text{(B.3)}$$

Replacing b in the PDE from eq. 3.32 with $\gamma = 1$,

$$\frac{Z}{T}\frac{b_{\mathrm{s}}}{2}\tilde{r}^{-\frac{1}{2}}\left[1+\frac{T}{2\tilde{r}}\right] = -\frac{\partial Z}{\partial T} + \frac{1}{2}\left(1 + b_{\mathrm{s}}\tilde{r}^{-\frac{1}{2}} - 2\frac{\tilde{r}}{T}\right)\frac{\partial Z}{\partial \tilde{r}}. \quad \text{(B.4)}$$

This equation is a first-order linear Partial Differential Equation (PDE), and we try to solve it by the Method of Characteristics for Non-Constant Coefficients (for a more detailed explanation of the derivation, see section 3.2.2 or Riley et al., 1999). The characteristic equation, in this case,

$$\frac{d\,\tilde{r}}{\frac{1}{2}\left(1 + b_{\mathrm{s}}\tilde{r}^{-\frac{1}{2}} - 2\frac{\tilde{r}}{T}\right)} = -d\,T. \quad \text{(B.5)}$$

This equation is a non-linear first-order Ordinary Differential Equation (ODE). We were not able to analytically solve this non-linear equation. We could linearise the equation around $\tilde{r} \sim 1$, but in that case, $\mathrm{St} \sim \mathrm{St}_0$. Hence, we decided to look for a solution for constant St directly. Nevertheless, in the drift-limited region, we see that the r-dependency of b is weak ($b \propto \mathrm{St}\cdot\chi \propto \mathrm{r}^{-\frac{4}{7}}$ for $\gamma = \frac{15}{14}$). Therefore, it might be a better approximation to assume $\mathrm{St}\cdot\chi$ constant rather than St constant. In the case of $\mathrm{St}\cdot\chi$ constant, and therefore b constant, we get the solution eq. 3.57.

B.2 Exploring an alternative method for determining the evolving metallicity

In this section, we describe an alternative way of deriving the pebble flux. First, we use simplified expressions for the gas surface density and gas flux, commonly used to describe the inner regions,

$$\Sigma_{\mathrm{g}}(r,t) = \frac{\dot{\mathcal{M}}_{g,0}}{3\pi\nu_1}\left(\frac{R_1}{r}\right)^{\gamma} T^{\eta}, \quad \text{(B.6)}$$

$$\dot{\mathcal{M}}_g(t) = \dot{\mathcal{M}}_{g,0} T^{\eta}, \tag{B.7}$$

where $\eta = -\frac{5/2-\gamma}{2-\gamma}$. Recalculating $\frac{\partial \ln P}{\partial \ln r}$ with the simplified $\Sigma_{\rm g}(r,t)$ (see eq. 3.20), we get that $\chi = \chi_0$. The ratio between the radial velocities (see eq. 3.15 and 3.18)

$$\frac{v_{\rm r,p}}{v_{\rm r,g}} = \frac{1 + \frac{2}{3}\frac{\rm St}{\alpha}\chi_0}{1 + {\rm St}^2}. \tag{B.8}$$

From eq. 3.16, we know that the total mass of the gas disk is

$$M_g(t) = \frac{2}{3}\frac{\dot{\mathcal{M}}_{g,0}}{\nu_1}\frac{R_1^2}{(2-\gamma)} T^{\eta+1} = 2(2-\gamma) t_{\rm s} \dot{\mathcal{M}}_g(t) \cdot T. \tag{B.9}$$

where $t_{\rm s}$ is the viscous timescale (see eq. 3.11). We derive the mass over time,

$$\frac{d\,M_{\rm g}}{d\,t} = \frac{2}{3}\frac{\dot{\mathcal{M}}_{g,0}}{\nu_1}\frac{R_1^2}{(2-\gamma)}\frac{(\eta+1)}{t_{\rm s}} T^{\eta} = -\dot{\mathcal{M}}_{g,0} T^{\eta} = -\dot{\mathcal{M}}_g(t). \tag{B.10}$$

Assuming that $Z(r,t) \approx Z(t)$, we can relate the mass of the gas and the mass of the pebbles,

$$M_{\rm p}(r,t) = \int 2\pi r \Sigma_{\rm p}(r,t) d\,r = \int 2\pi r Z(r,t) \Sigma_{\rm g}(r,t) d\,r \approx Z(t) M_{\rm g}(t). \tag{B.11}$$

Therefore, $M_{\rm p}(t) \approx Z(t) M_{\rm g}(t)$. Taking the derivative of this equation over time,

$$\frac{d\,M_{\rm p}(t)}{d\,t} = \frac{d\,Z}{d\,t} M_{\rm g}(t) + \frac{d\,M_{\rm g}}{d\,t} Z(t). \tag{B.12}$$

As $\frac{d\,M_{\rm g}}{d\,t} = -\dot{\mathcal{M}}_g(t)$ (see eq. B.10), we assume that $\frac{d\,M_{\rm p}}{d\,t} = -\dot{\mathcal{M}}_p(t)$ as well. Hence,

$$-\dot{\mathcal{M}}_p(t) = \frac{d\,Z}{d\,t} M_{\rm g}(t) - \dot{\mathcal{M}}_g(t) Z(t), \tag{B.13}$$

$$Z(t)\dot{\mathcal{M}}_g(t) \left(1 - \frac{v_{\rm r,p}}{v_{\rm r,g}}\right) = \frac{d\,Z}{d\,t} M_{\rm g}(t). \tag{B.14}$$

Replacing eq. B.9,

$$\left(1 - \frac{v_{\rm r,p}}{v_{\rm r,g}}\right) \frac{1}{2(2-\gamma)t_{\rm s}} \frac{1}{T} d\,t = \frac{d\,Z}{Z}, \tag{B.15}$$

$$\boxed{Z(t) = Z_0 T^{\frac{1}{2(2-\gamma)}\left(1 - \frac{v_{\rm r,p}}{v_{\rm r,g}}\right)}} \tag{B.16}$$

Assuming that $\frac{1}{{\rm St}^2+1} \sim 1$, from eq. B.8,

$$Z(t) = Z_0 T^{-\frac{1}{2(2-\gamma)}\frac{2}{3}\frac{\rm St}{\alpha}\chi_0}. \tag{B.17}$$

We get the same result as in eq. 3.57.

C Other results

In this appendix, we include results that can help the reader understand the details of the findings.

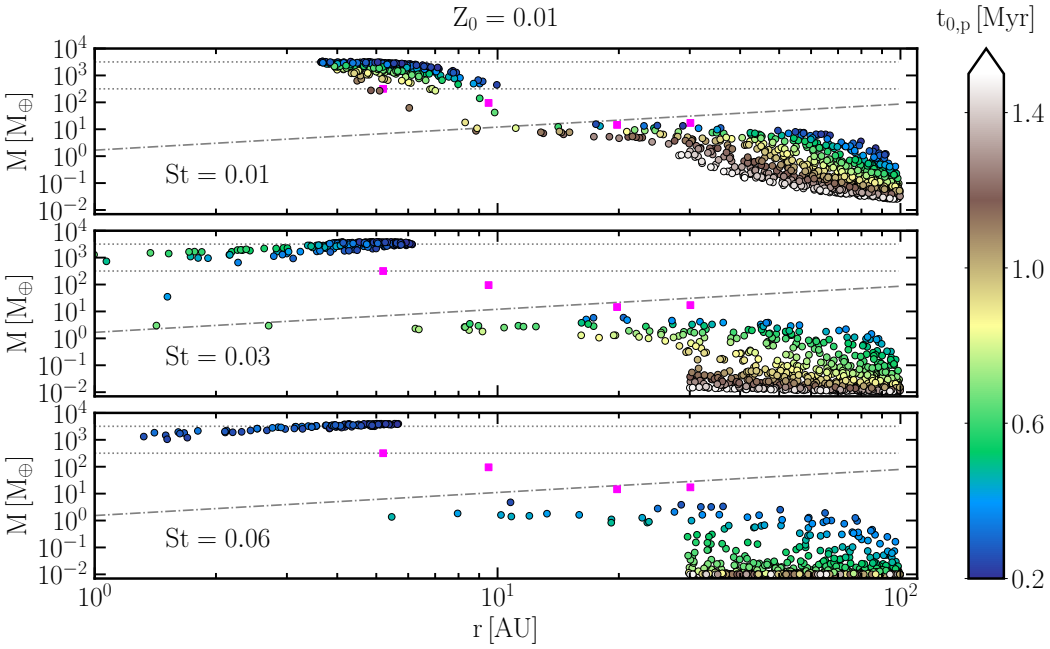

Figure C.1: Same as fig. 4.9 but showing $t_{0,p}$ in the color-bar. When St $\gtrsim$ 0.03, only early-formed embryos can become gas giants orbiting at ~ 6 AU at furthest. When St = 0.01, late-formed embryos can become gas giants. For the same initial location, later-formed ones will be less massive.

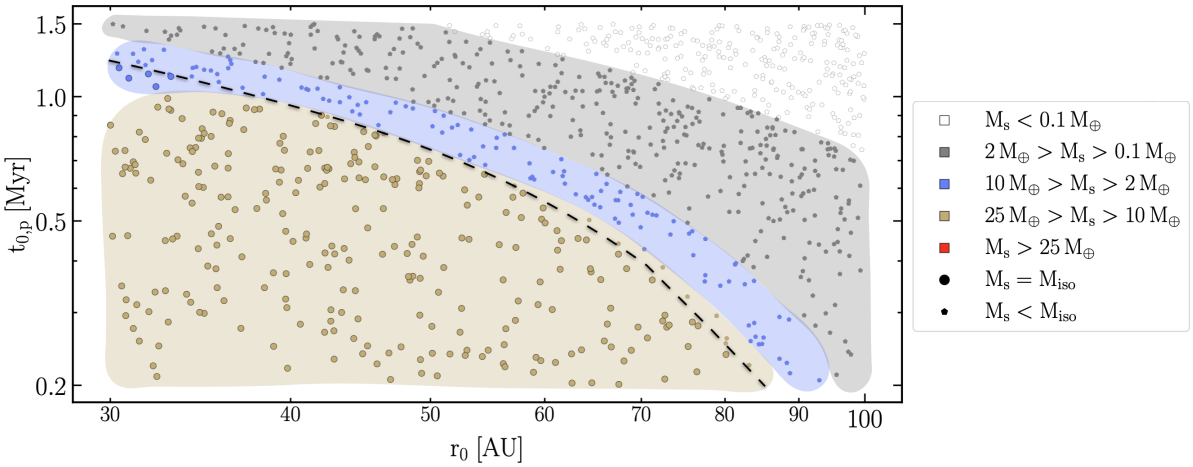

Figure C.2: When St = 0.01, the total solid mass of protoplanets depending on the initial position and formation time of the embryos. None of the protoplanets reach $M_s \geq 25\,M_\oplus$. However, more protoplanets reach M_{iso} than in the case of St = 0.03 (see fig. 4.4).

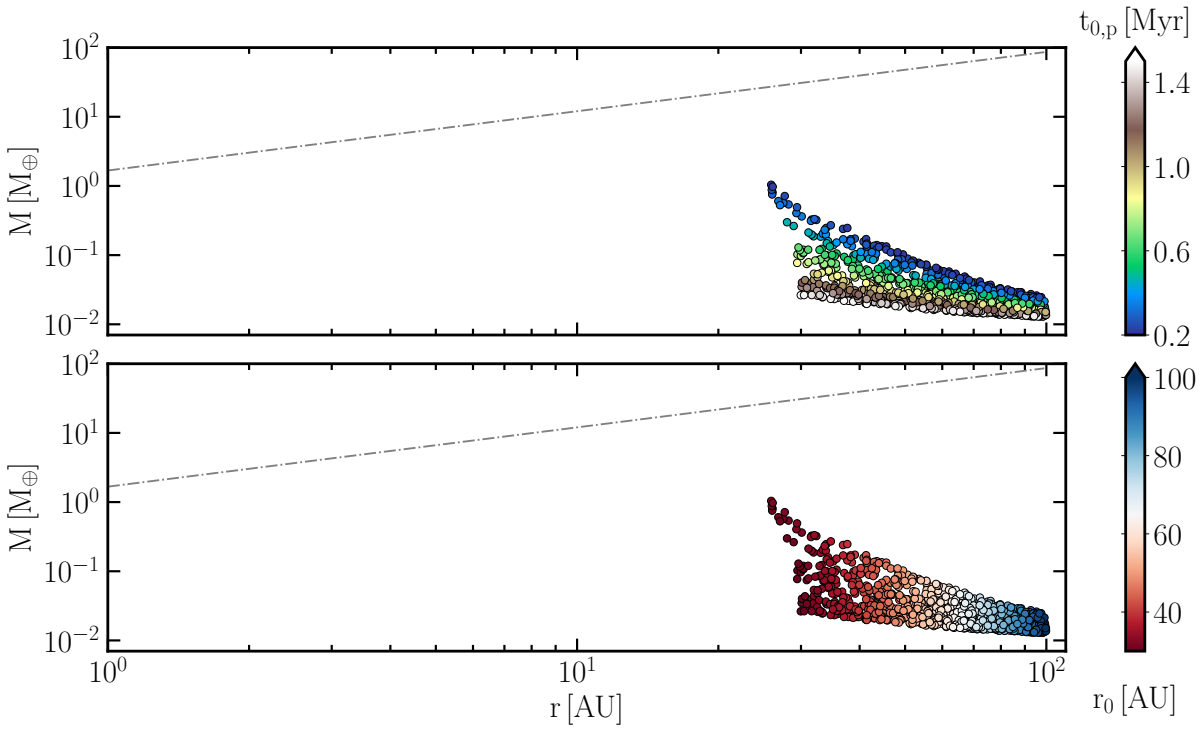

Figure C.3: Evolution of protoplanets when St = 0.005 and $\alpha_t \sim 10^{-3}$. There is very little growth, so wide-orbit gas giants cannot form within this scenario.

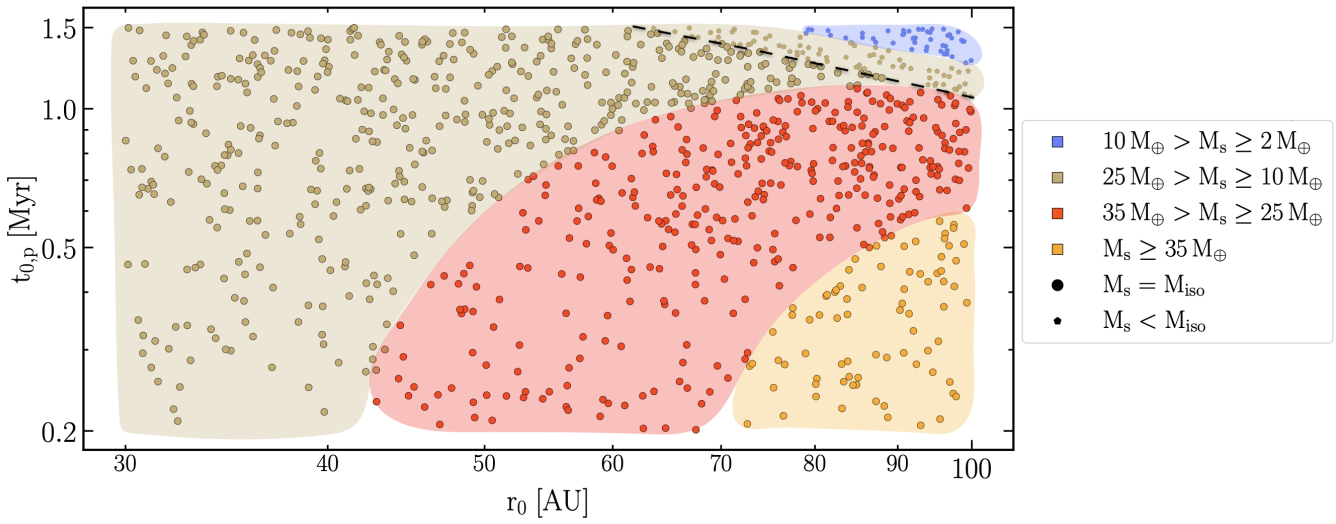

Figure C.4: When St = 0.01, Z_0 = 0.02 and $\alpha_t \sim 10^{-5}$, the total solid mass of the protoplanets depending on the initial position and formation time of the seeds. Most protoplanets reach M_{iso}. Early-formed and distant embryos form distant and massive cores.

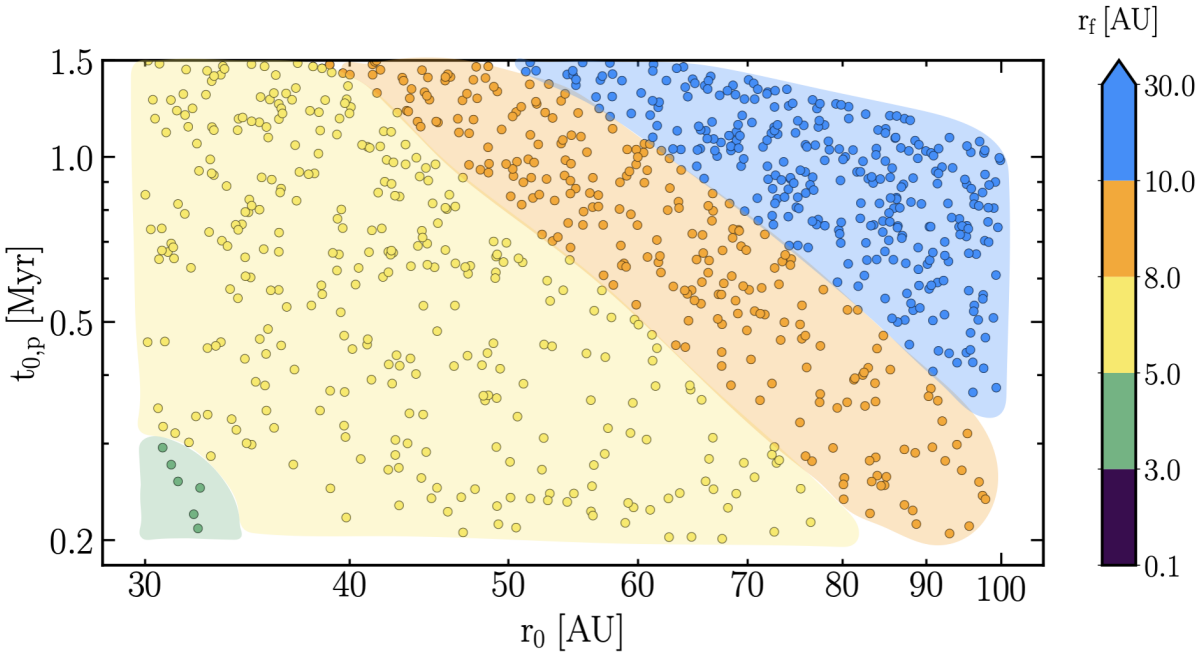

Figure C.5: When St = 0.01, $Z_0 = 0.02$ and $\alpha_t \sim 10^{-5}$, the final position of the gas giants depending on the initial position and formation time of the seeds. Embryos initiated far away become the furthest gas giants. Since the pebble flux is long-lasting, contrary to fig. 4.6b, for late-formed embryos, the final gas giants do not get closer to the star when the embryo forms further away.

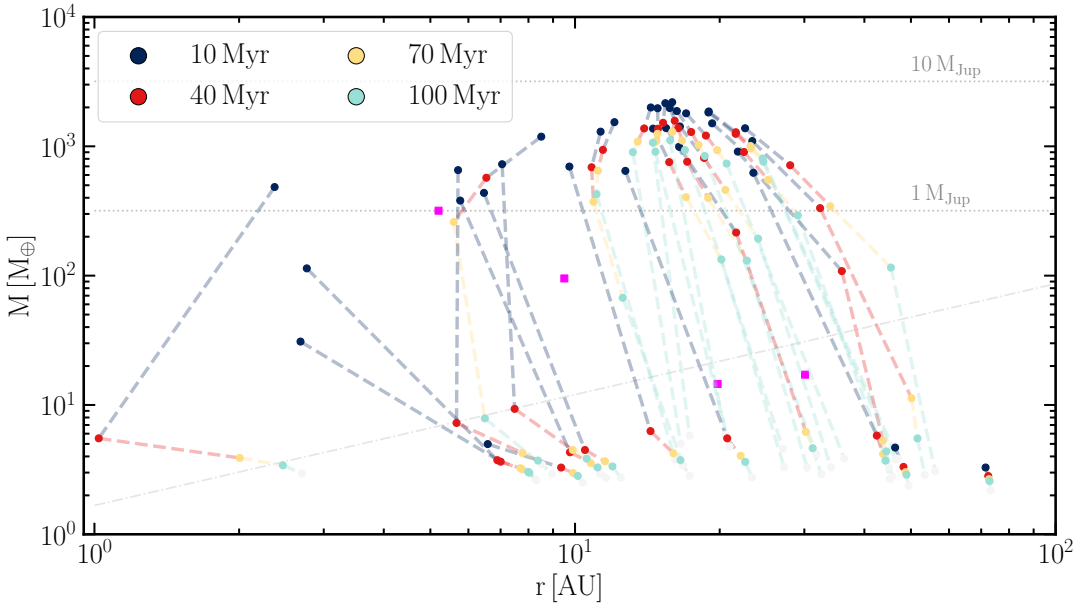

(a) Fiducial values.

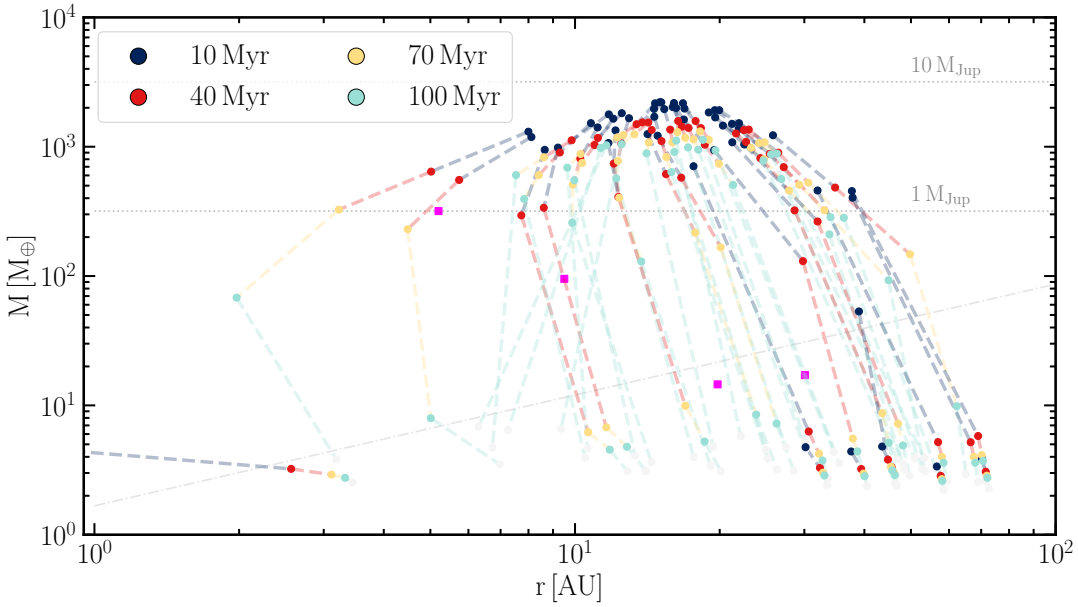

(b) $M_0 = 0.1\,\mathrm{M}_\oplus$.

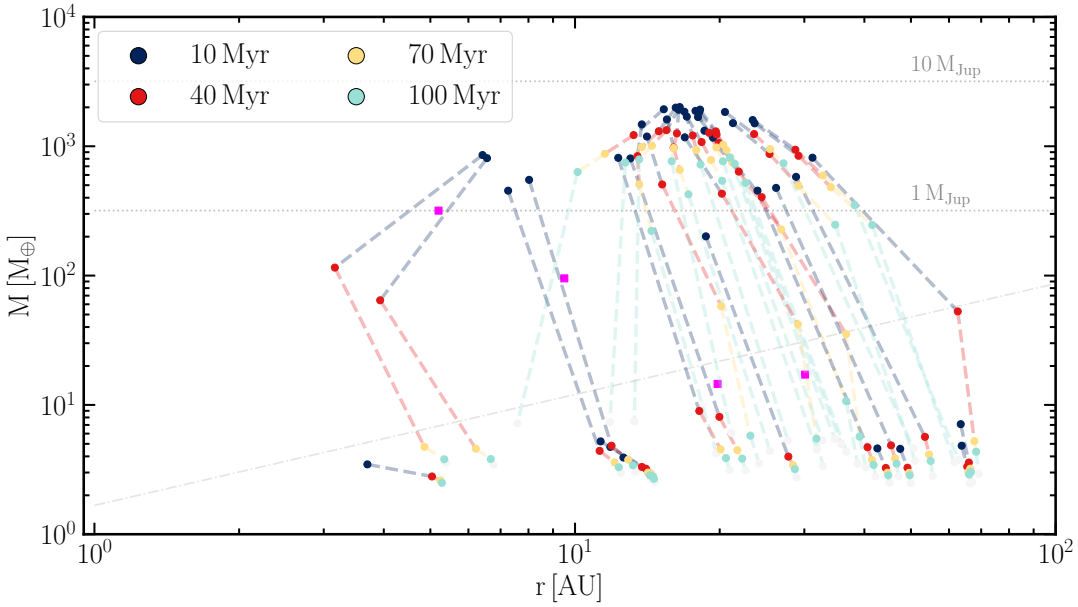

(c) $Z_0 = 0.02$.

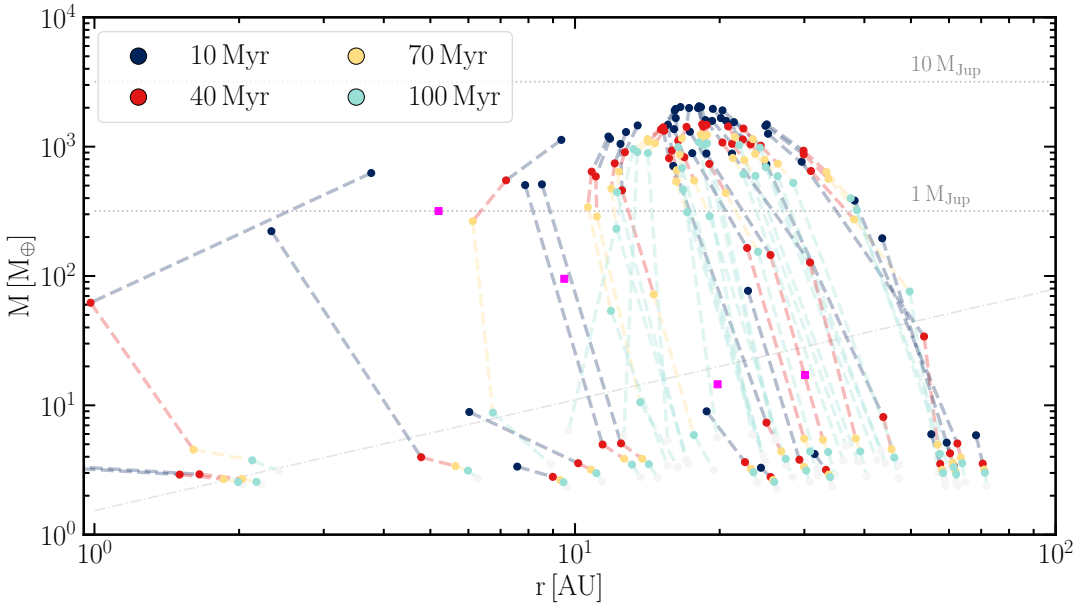

(d) $\alpha_t \sim 10^{-5}$.

Figure C.6: For different scenarios, the position and mass of giant planets formed without reaching M_{iso}, as explained in section 4.2.3. The lines connect the different outcomes of the same planet when varying τ_{th}. In all scenarios, most gas giants form between $10 - 30$ AU, and a few form at $40 - 50$ AU.